PAUL SCHERRER INSTITUT

Aeroradiometric Measurements in the Framework of the Swiss Exercise ARM18 and the International Exercise CONTEX 2018

Gernot Butterweck, Benno Bucher, Ladislaus Rybach, Cristina Poretti,
Stéphane Maillard, Mauro Schindler, Bénédicte Hofstetter-Boillat,
Sabine Mayer, Gerald Scharding

PSI Bericht Nr. 19-01
March 2019
ISSN 1019-0643

Aeroradiometric Measurements in the Framework of the Swiss Exercises ARM18 and the International Exercise CONTEX 2018

Gernot Butterweck[1], Benno Bucher[2], Ladislaus Rybach[3], Cristina Poretti[4], Stéphane Maillard[5], Mauro Schindler[5], Bénédicte Hofstetter-Boillat[1], Sabine Mayer[1], Gerald Scharding[4]

1 Division for Radiation Safety and Security, Paul Scherrer Institute (PSI), 5232 Villigen PSI, Switzerland
2 Swiss Federal Nuclear Safety Inspectorate (ENSI), Industriestrasse 19, 5200 Brugg, Switzerland
3 Institute of Geophysics, Swiss Federal Institute of Technology Zürich (ETHZ), 8092 Zürich, Switzerland
4 Swiss National Emergency Operations Center (NEOC), 8044 Zürich, Switzerland
5 Nuclear Biological Chemical - Explosive Ordnance Disposal (NBC-EOD) Centre of Competence, 3700 Spiez, Switzerland

Paul Scherrer Institut (PSI)
5232 Villigen PSI, Switzerland
Tel. +41 56 310 21 11
Fax +41 56 310 21 99
www.psi.ch

PSI Bericht Nr. 19-01
March 2019
ISSN 1019-0643

Abstract

The measurement flights of the exercise ARM18 were performed between May 28th and June 1st, 2018. The exercise was organized by the National Emergency Operations Centre (NEOC) under coordination from the Expert Group for Aeroradiometrics (FAR). Representatives of KompZen ABC-Kamir participated both in the exercise and performed separate measuring flights.
According to the alternating schedule of the annual ARM exercises, the environs of the nuclear power plants Beznau (KKB) and Leibstadt (KKL) and the nuclear facilities of the Paul Scherrer Institute (PSI) and the Zwischenlager Würenlingen AG (Zwilag) were surveyed. The measurements showed no artificial radionuclides outside of the plant premises. On request of German authorities, the measuring area was extended into German territory. In this area, a dose rate anomaly associated with ^{232}Th activity in a mineral processing plant could be identified.
The series of radiological background measurements over Swiss cities was complemented with measurements over Solothurn, Fribourg and Yverdon-les-Bains. The measurement in the vicinity of Yverdon-les-Bains was used to directly compare the evaluation software of the old ARM system (MGS32) to the proprietary software of the manufacturer of the RLL system (Mirion).
The international exercise CONTEX18 was performed in the International Atomic Energy Agency (IAEA) Response and Assistance Network (RANET) framework between June 19th and 21st in northern Denmark, coordinated by the Danish Emergency Management Agency (DEMA). It provided the opportunity to measure an altitude profile over the North Sea with low airborne radon progeny concentrations. A clear difference to measurements over Swiss inland lakes was observed. This difference was used for investigating a potential method to compensate for the influence of airborne radon progeny on the measurement of ^{238}U activity concentrations. The organisers of the exercise placed several sources of different radionuclides and activities in the exercise area, challenging the performance of airborne detection. A method using maxima of the man-made-gross-count(MMGC)-ratio to define points which should be inspected more closely was developed. The spectra of these points of interest were inspected in detail and led to the identification of ^{137}Cs, ^{192}Ir, ^{99m}Tc, ^{75}Se and ^{111}In sources.
Measurements around Mont Vully on behalf of the University of Basel could not clearly locate small scale anomalies of ^{238}U concentrations due to the field of view of the airborne measurements and depth of the peat layer containing elevated ^{238}U concentrations.
Measurements along a transversal showed expected results due to flight altitude and attenuation of photons by water bodies.

Contents

List of Figures

List of Tables

1 Introduction

Swiss airborne gamma spectrometry measurements started in 1986. Methodology and software for calibration, data acquisition and mapping were developed at the Institute of Geophysics of the Swiss Federal Institute of Technology Zurich (ETHZ). Between 1989 and 1993 the environs of Swiss nuclear installations were measured annually on behalf of the Swiss Federal Nuclear Safety Inspectorate (ENSI) during exercises performed annually as system check and drill for the operators. This schedule was changed to biannual inspections in 1994, together with an organizational inclusion of the airborne gamma-spectrometric system (ARM) into the Emergency Organization Radioactivity (EOR) of the Federal Office for Civil Protection (FOCP). The deployment of the airborne gamma-spectrometric system is organized by the National Emergency Operations Centre (NEOC). NEOC is also responsible for the recruitment and instruction of the measurement team and the operational readiness of the system. Aerial operations are coordinated and performed by the Swiss Air Force with Super Puma helicopters. The gamma-spectrometric equipment is stationed at the military airfields of Dübendorf and Payerne. The gamma-spectrometry system can be airborne within four hours. Responsibility for scientific support, development and maintenance of the aeroradiometric measurement equipment passed from ETHZ to the Radiation Metrology Section of the Paul Scherrer Institute (PSI) in 2003 in cooperation with ENSI. General scientific coordination and planning of the annual measuring flights is provided by the Expert Group for Aeroradiometrics (FAR). FAR was a working group of the Swiss Federal Commission for NBC-protection (ComNBC) and consists of experts from all Swiss institutions concerned with aeroradiometry. FAR was re-organized as an expert group of the NEOC in 2008. Additional information can be found at http://www.far.ensi.ch/.
In 2018 the ARM measuring system used by the NEOC in the past exercises was replaced with the RLL (Radiometrie Land-Luft) system owned by the Swiss air force. Of the four systems available, under normal circumstances two systems are operated by staff of the NBC-EOD Centre of Competence (KompZen ABC-Kamir) for measurements tasks with military character and two systems are assigned to NEOC for the deployment in case of civil emergencies with a radiological component. As identical measuring systems are used, the results of measuring flights performed by NBC-EOD Centre of Competence are included into the scientific report. As from 2018, the scientific report includes as before measuring flights of the NEOC (ARM18z) together with measuring flights performed by the NBC-EOD Centre of Competence (ARM18m).
This report focuses on methodological aspects and thus complements the short report of NEOC about the annual flight surveys (available from the NEOC website https://www.naz.ch).

1.1 Measuring System RLL

The measuring system RLL (Radiometrie Land-Luft) consists of a radiation detector with four NaI(Tl) scintillation crystals with a total volume 16.8 litres and associated photo-multipliers and multichannel analysers for low level measurements and one Geiger-Müller tube and associated electronics for high-level dose rate measurement. Detectors, Geiger-Müller tube and associated electronics are installed in an aluminium case with thermal insulation foam. The detection container is mounted in the cargo bay below the centre of the helicopter. The RLL system uses position, air pressure, air temperature and radar altitude provided by the helicopter via the internal ARINC bus. Figure 1 shows the complete system packaged for storage. The equipment control, data acquisition and storage are performed with a rugged computer working as a data server. Two further rugged redundant client computers are used as operator interface for real-time evaluation, data mapping and communication. All computers are installed in an equipment rack including a battery backed-up power supply. Both operators can operate the system with their associated client computer, display, keyboard and trackball. The additional third central display of the operator's console is mirrored in the cockpit on a screen located between both pilots and is used for information exchange with the pilots and general radiological situation awareness (figure 2). The measuring system RLL is mounted in an Aerospatiale AS 332 Super Puma helicopter (TH 06) of the Swiss Air Forces (figure 3). This helicopter has excellent navigation properties and allows emergency operation during bad weather conditions and night time.

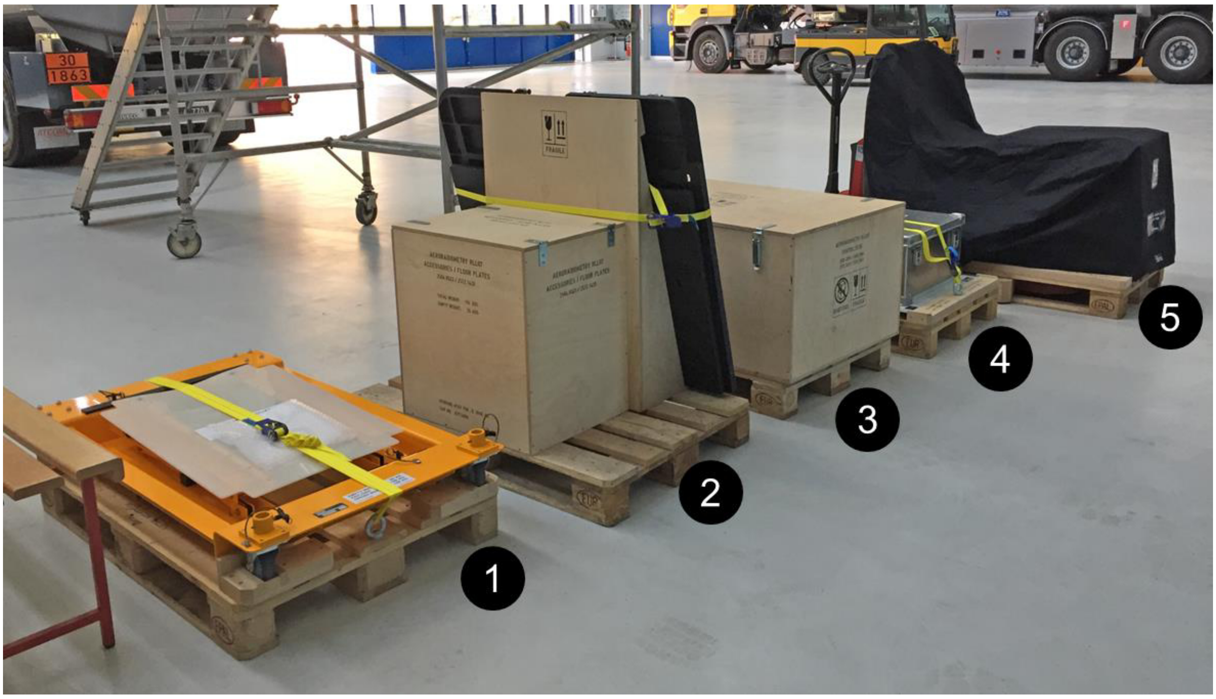

Figure 1: Components of the RLL system. 1. Lifting platform for the installation of the detection container. 2. Floor plates and accessories case. 3. Monitors and operator console. 4. Detection container. 5. Operator seats and equipment rack.

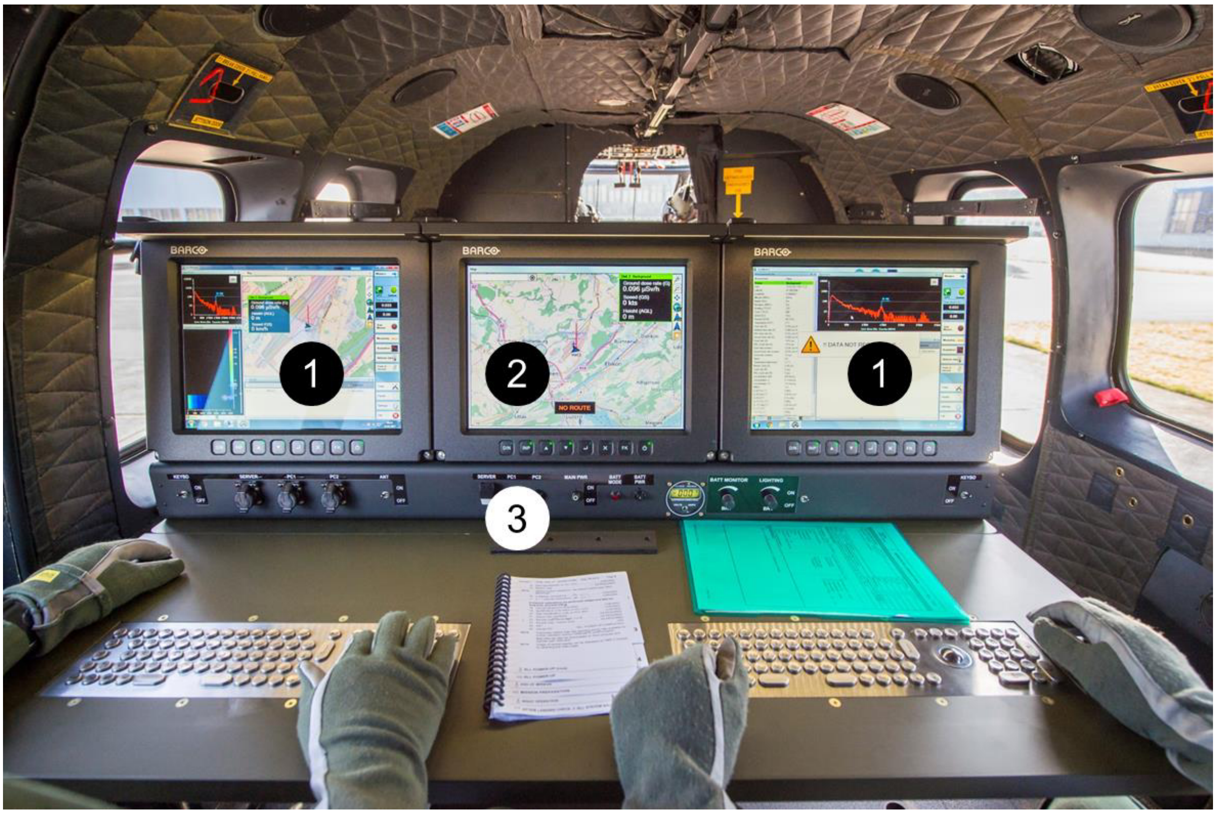

Figure 2: Operator console of the RLL system. 1. Displays of the client computers. 2. Common display (mirrored in the cockpit). 3. Control panel with switches for power, lighting and communication and USB ports for file exchange.

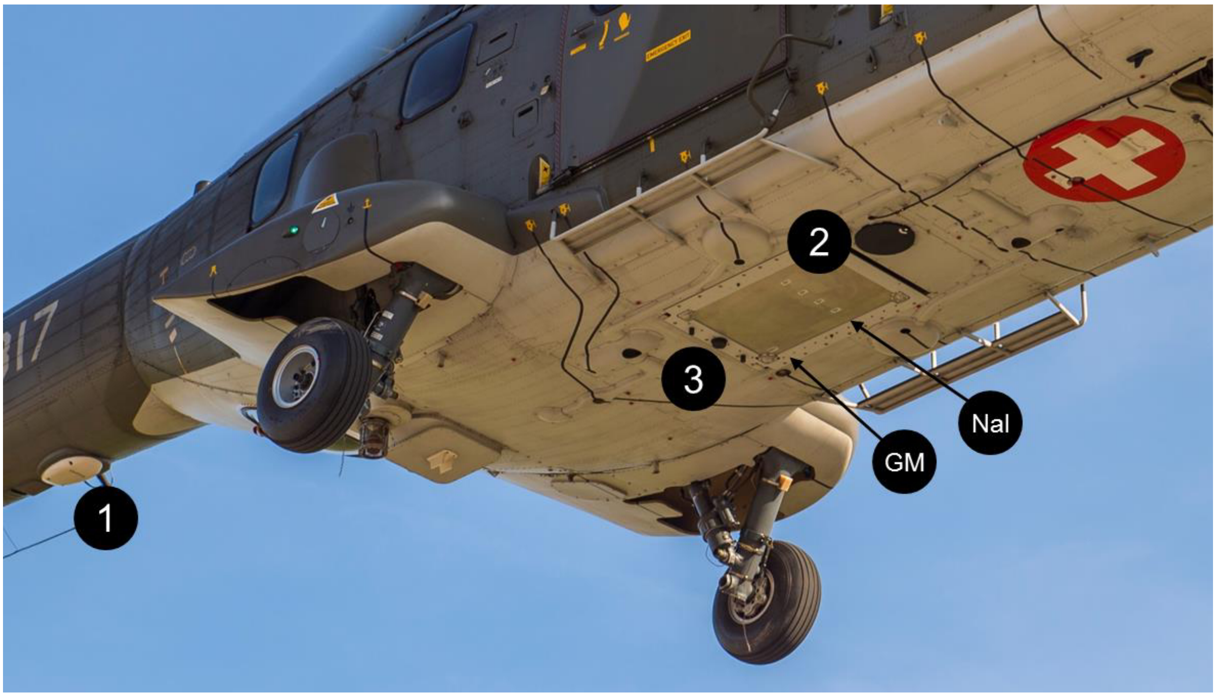

Figure 3: RLL detector mounted in the cargo bay of a Super Puma helicopter. 1. Radar altimeter. 2. Detection container marked with detector reference points. 3. UMTS antenna for data upload.

1.2 Measuring flights

The advantage of aeroradiometric measurements lies in the high velocity of measurements in a large area, even over rough terrain. Uniform radiological information of an area is obtained from a regular grid of measuring points. This grid is composed from parallel flight lines which are 100 m to 500 m apart, depending on the scope of the measurement. The flight altitude above ground is aspired to be constant during the measuring flight. Typical values lie between 50 m and 100 m above ground. The spectra are recorded in regular time intervals of typical one second, yielding integration over 28 meters of the flight line at a velocity of 100 km/h.

1.3 Data evaluation

The data evaluation follows the methodology described in Schwarz (1991). Since 2000, the software developed by the Research Group for Geothermics and Radiometry of the Institute of Geophysics of the Swiss Federal Institute of Technology Zurich (ETHZ) (Bucher, 2001) is used.

1.4 Data presentation

A first brief report (Kurzbericht) of the measurement results is compiled by the measurement team and published immediately after the end of the exercise on the homepage of NEOC. These reports are archived at `http://www.far.ensi.ch`.
Results of a further data evaluation are published in the form of a PSI-report, within the responsibility of the FAR. These reports are also archived at `http://www.far.ensi.ch`.
For all measuring areas, a map of the total dose rate (measuring quantity H*(10) at 1 m above ground) and the flight lines is presented together with a map of the Man-Made-Gross-Count (MMGC) ratio. A map of the ^{232}Th activity concentration (measuring quantity activity per dry mass) yields quality information as it can be expected that this quantity is constant over time. As an additional quality measure, an appendix with the basic parameters of the data evaluation is added to simplify a re-evaluation of the data in the future. If the MMGC-ratio indicates elevated values, maps of individual radionuclides are added based on the average photon spectrum over the affected area. In the case of large changes of topography in the measured area, a map of the terrestrial dose rate consisting of the total dose rate reduced of the altitude dependent cosmic component is included. In the case of measuring flights with the main purpose of mapping natural radionuclide concentrations, a supplementary map of the ^{40}K activity concentration (measuring quantity activity per wet mass) is also presented. All maps use a gradual colour scale from blue for low values to red for high values. The maximum and minimum values are specified in the legend together with the measurement unit of the depicted quantity. The colours for 10 percent steps between minimum and maximum values of the scale are given in Table 1. Minimum and maximum of the colour scale for the measured quantity are generally set to standard values to facilitate easier comparison of maps. Maps with different value ranges are added if considered helpful to the reader.

Percentage	≤0	10	20	30	40	50	60	70	80	90	≥100
Color											

Table 1: Quantification of the color scale.

2 Results of the measuring flights during the exercises ARM18 and CONTEX18

The flights of the exercise ARM18m of the NBC-EOD Centre of Competence were performed from March 20th to March 22nd in the vicinity of Yverdon-les-Bains. The flights of the exercise ARM18z of NEOC were performed between May 28th and June 1st, 2018. The flights of the international exercise CONTEX18 were performed between June 19th and 21st. Flight velocity of the Super Puma helicopters of the Swiss Air Force was around 30 m/s with a ground clearance of 90 m for all measuring flights. The counting interval of the spectra was one second.
Personnel of the military units Stab BR NAZ and NBC-EOD Centre of Competence performed the measurements supported by experts from ENSI, PSI, NBC-EOD and NEOC. A short report of the measurement results of ARM18z was placed on the NEOC website `https://www.naz.ch/` on June 1st, 2018.
Flight parameters of the measuring flights are listed in Table 2.

Location	Flight number	Measuring time [s]	Length of run [km]	Area [km^2]
KKB, KKL, PSI, Zwilag	Heli2_20180528 0855 Heli2_20180528 1400 Heli2_20180529 0840 Heli2_20180528 1400	18179	838	238
Fribourg	Heli2_20180530 1330	5201	235	44
Solothurn	Heli2_20180529 1405	5334	265	49
Yverdon-les-Bains	Heli 3_20180320 1445 Heli 3_20180320 1540 Heli 3_20180321 1015 Heli 3_20180321 1345 Heli 3_20180321 1445 Heli 3_20180322 0830	18175	806	195
Mont Vully	Heli2_20180530 0900	5324	286	73
Lake Geneva	Heli2_20180531 0950	1373	-	-
North Sea	Heli2_20180619 1135	954	-	-
CONTEX18 exercise area	Heli2_20180619 1105	871	35	12
CONTEX18 exercise area	Heli2_20180620 0845	2662	101	21
CONTEX18 exercise area	Heli2_20180621 0900	2260	92	18

Table 2: Flight data of ARM18 and CONTEX18.

2.1 Recurrent measurement area KKB, KKL, PSI and Zwilag

According to a biannual rotation of routine measurements, the environs of the nuclear power plants Beznau (KKB) and Leibstadt (KKL), the Paul Scherrer Institute and the intermediate storage facility Zwilag were inspected in 2018 extended with an area to the west (sectors

4 and 5 of the emergency management zone). Following a request of German authorities, the measuring area was extended beyond the Rhine river into German territory. The line spacing in the additional region was widened to 1 km to increase area coverage versus measuring time.
The maps of dose rate (figure 4) and its terrestrial component (figure 5) show clearly elevated values over KKL and a location in German territory north of the Rhine river at coordinates (644887, 267409).
The elevated dose rate over the premises of KKL is caused by high energy photon radiation of the activation product ^{16}N, a typical result for operating boiling water reactors. The high energy photon radiation of ^{16}N leads also to misinterpretations in the maps of ^{40}K, ^{232}Th and ^{238}U (figures 7, 8 and 9). This effect was already observed in previous years and described in detail in the respective reports (for example PSI-reports 07-02, 09-02 and 11-02).
The map of the MMGC-ratio (figure 6) as an indicator for the presence of man-made radionuclides indicates no man-made radionuclides in the vicinity of coordinates (644887, 267409), where elevated dose rates were observed. The spectrum over this area shows an elevation of the peaks associated with the 583 keV and 2615 keV photon emission of ^{208}Tl (figure 11). ^{208}Tl is one of the radionuclides in the natural Thorium decay series. The radionuclides of the natural decay series provide various photon emissions with different photon energies. This leads together with the additional effect of Compton-scattering in ground and air to an increase of count rates throughout the spectrum. The map of the ^{232}Th activity concentration confirms elevated concentrations of the Thorium decay series (figure 8) at the location with elevated dose rates. The map of the ^{238}U activity concentration (figure 9) shows in the vicinity of coordinates (644887, 267409) a less pronounced elevation of activity concentrations, whereas no elevated ^{40}K activity concentrations were observed at the location (figure 7). An internet research associates a company processing minerals with coordinates (644887, 267409). The more distinct elevation of ^{232}Th activity concentration compared to ^{238}U activity concentration indicates a mineral with a high Thorium to Uranium ratio like Monazite (Hurley and Fairbairn, 1957).
The slightly elevated dose rate at Rotbergegg at coordinates (657113, 257267) is due to a known anomaly of the natural radionuclide ^{232}Th, which can be seen more clearly in the ^{232}Th map (Figure 8). With the extension of the measuring area to the west, a larger structure with elevated thorium concentrations becomes visible. This structure coincides with the lithostratigraphic unit Brown Jurassic (formerly also called Dogger), depicted in blue-gray color in figure 10.
The dose rate maps (figures 4 and 5) show very lightly increased values over the accelerator building at the Paul Scherrer Institute area West. The map of the MMGC-ratio indicates clearly the presence of man-made radionuclides (figure 6). The spectrum over the accelerator building indicates the radionuclide ^{60}Co as source for the measured signal (figure 12). The main proton accelerator was in maintenance shut-down during the measuring flights. Radiation protection officers at PSI informed NEOC that the shielding on top of the vacuum system conducting protons to the various experiments was opened for maintenance during the measuring flights. During operation of the accelerator, ^{60}Co is produced in steel components of the accelerator system by activation.

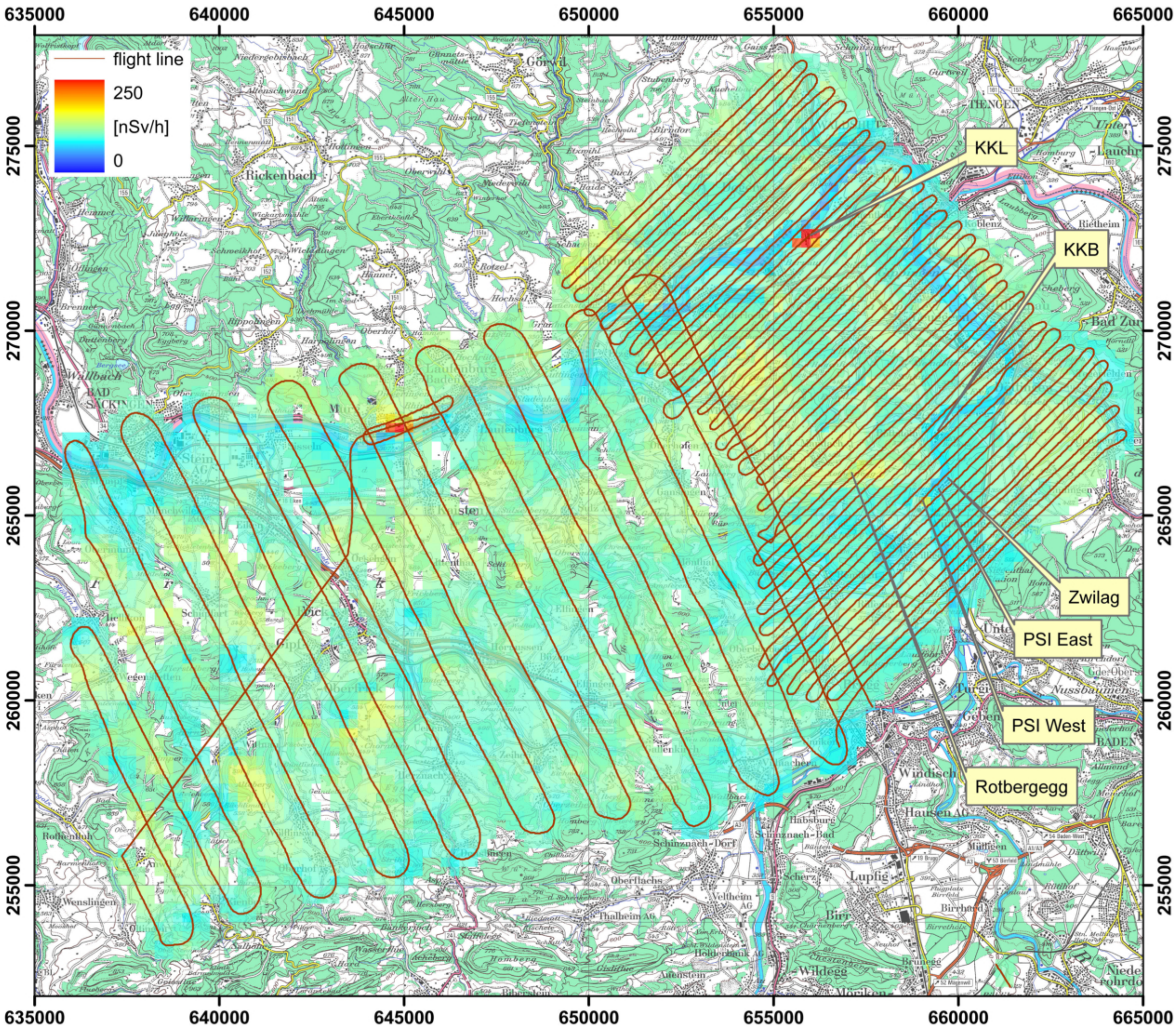

Figure 4: Dose rate in the vicinity of KKB, KKL, PSI and Zwilag.
PK100 ©2018 swisstopo (JD100042).

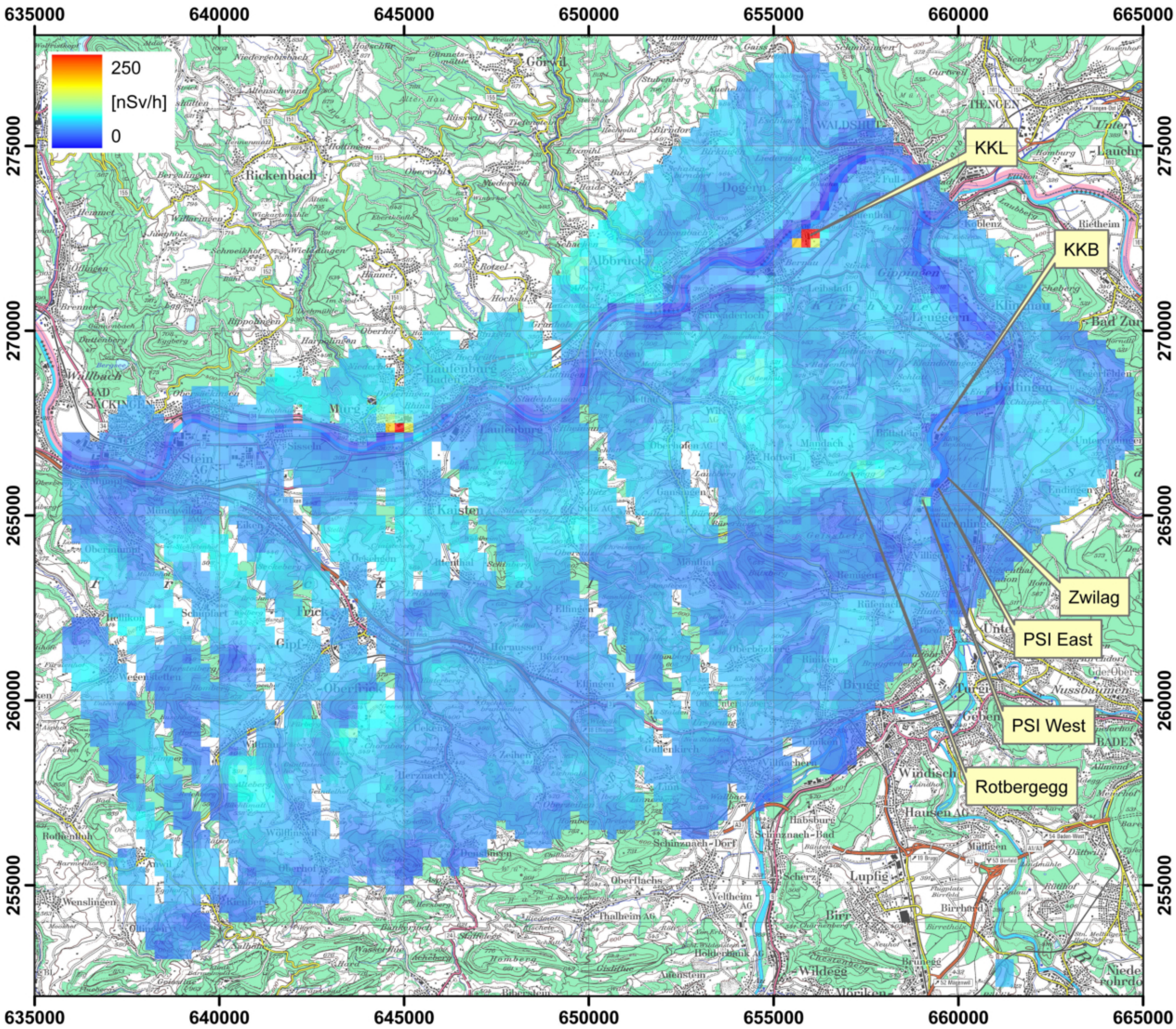

Figure 5: Terrestrial component of the dose rate in the vicinity of KKB, KKL, PSI and Zwilag. PK100 ©2018 swisstopo (JD100042).

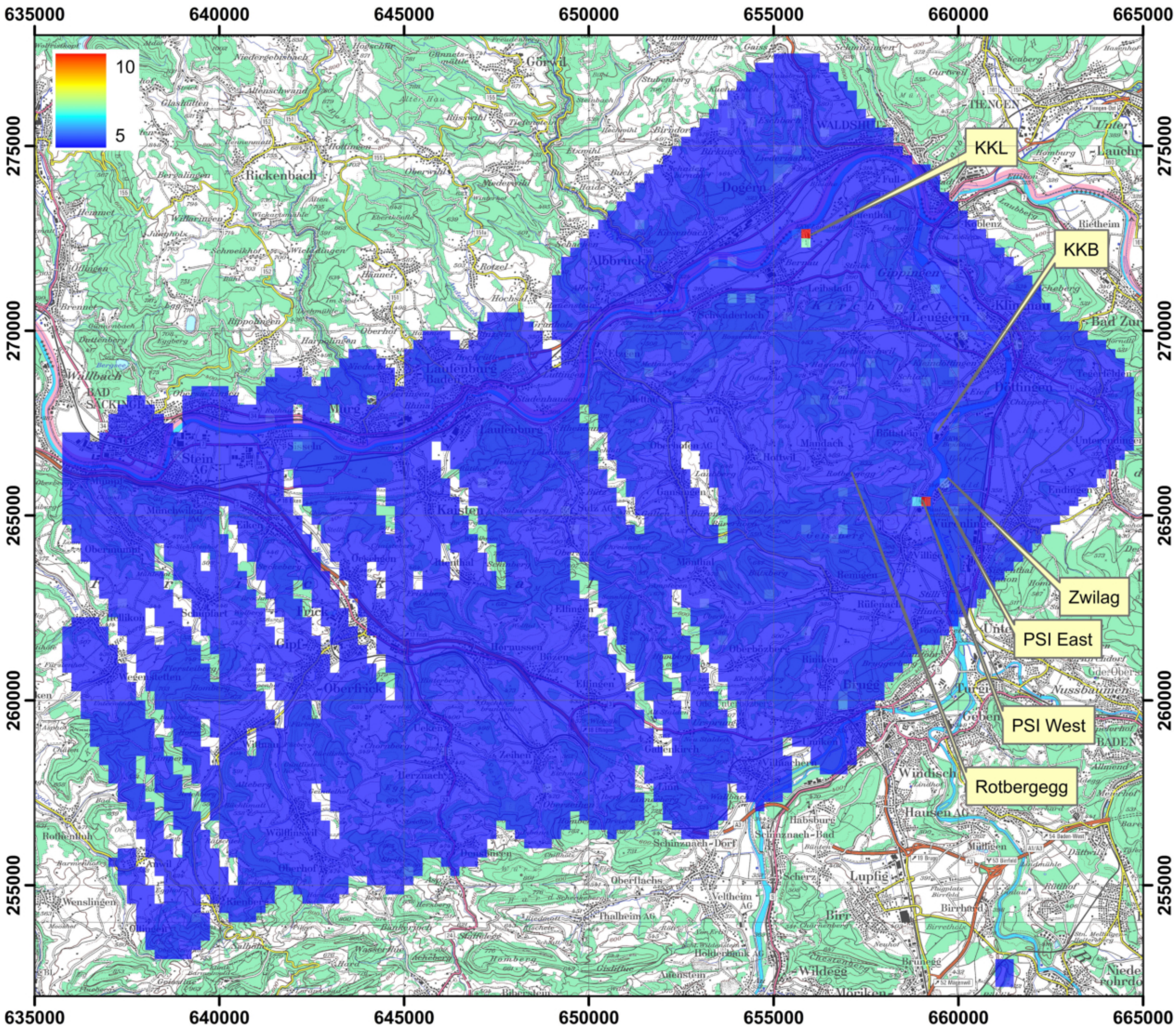

Figure 6: MMGC-ratio in the vicinity of KKB, KKL, PSI and Zwilag.
PK100 ©2018 swisstopo (JD100042).

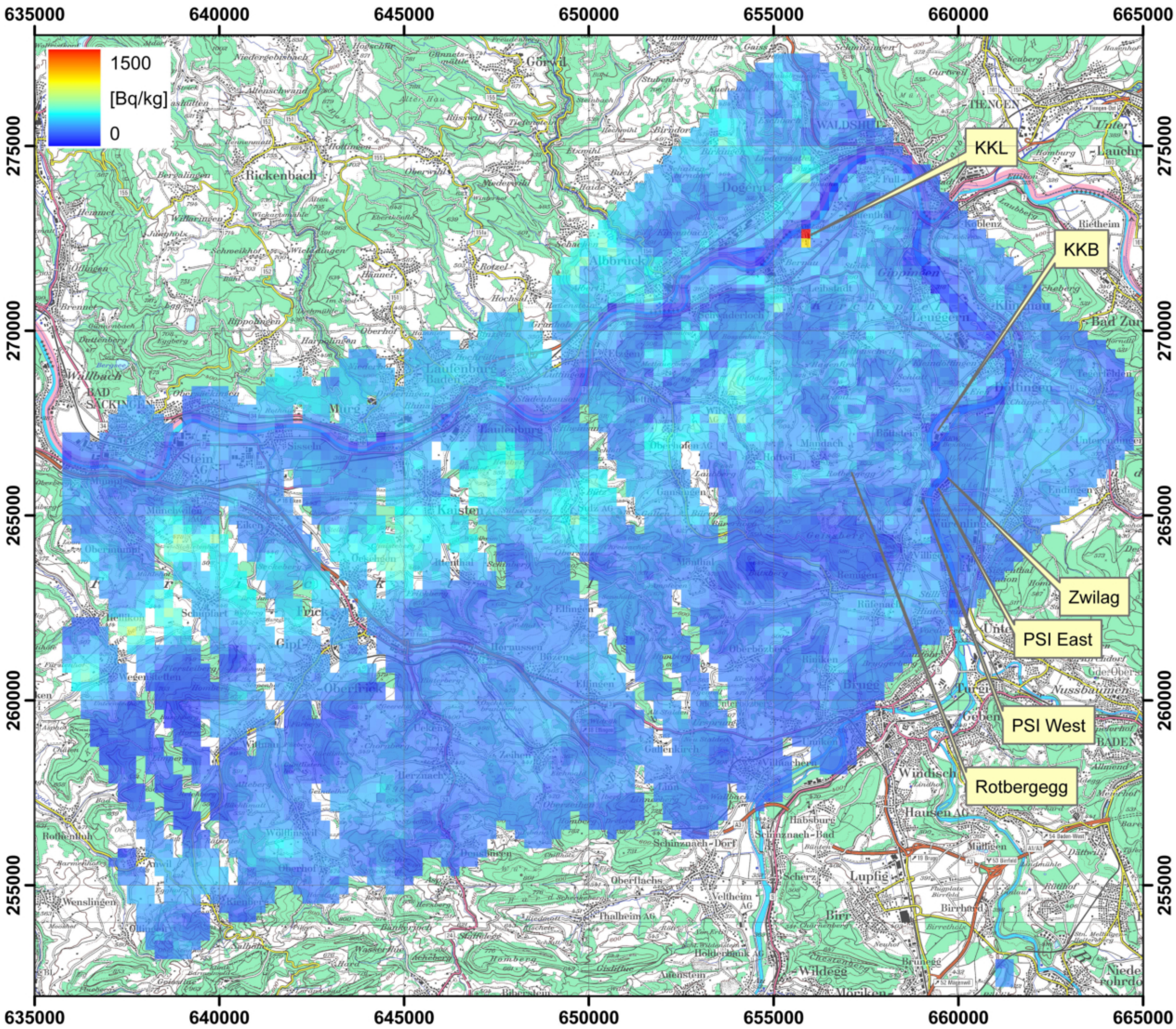

Figure 7: ^{40}K activity concentration in the vicinity of KKB, KKL, PSI and Zwilag. The high ^{40}K activity concentrations depicted over KKL are an artefact caused by a misinterpretation of photons emitted from ^{16}N.
PK100 ©2018 swisstopo (JD100042).

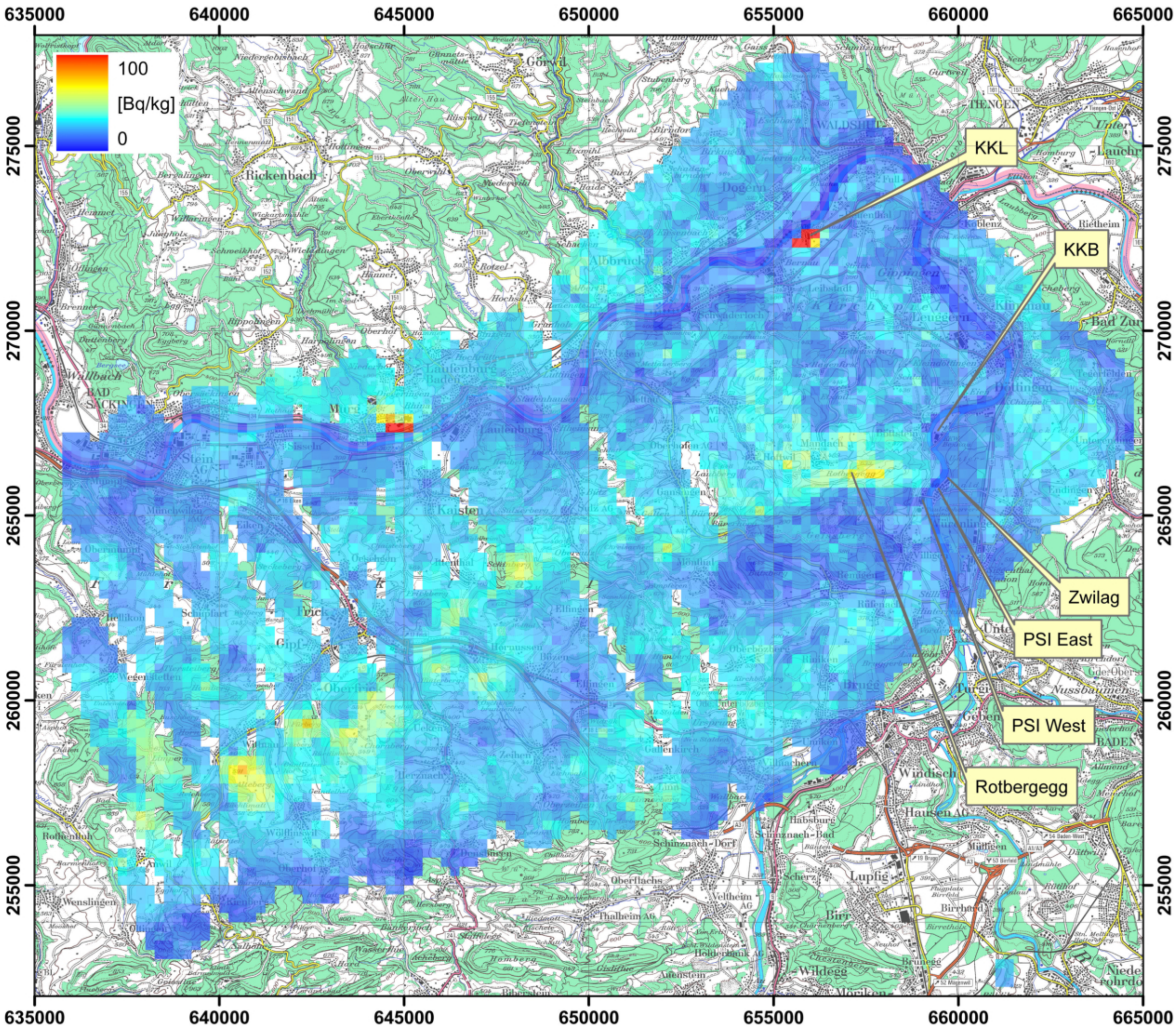

Figure 8: ^{232}Th activity concentration in the vicinity of KKB, KKL, PSI and Zwilag. The high ^{232}Th activity concentrations depicted over KKL are an artefact caused by a misinterpretation of photons emitted from ^{16}N; the hot spot at coordinates (644887, 267409) originates from a mineral-processing company (details see text). PK100 ©2018 swisstopo (JD100042).

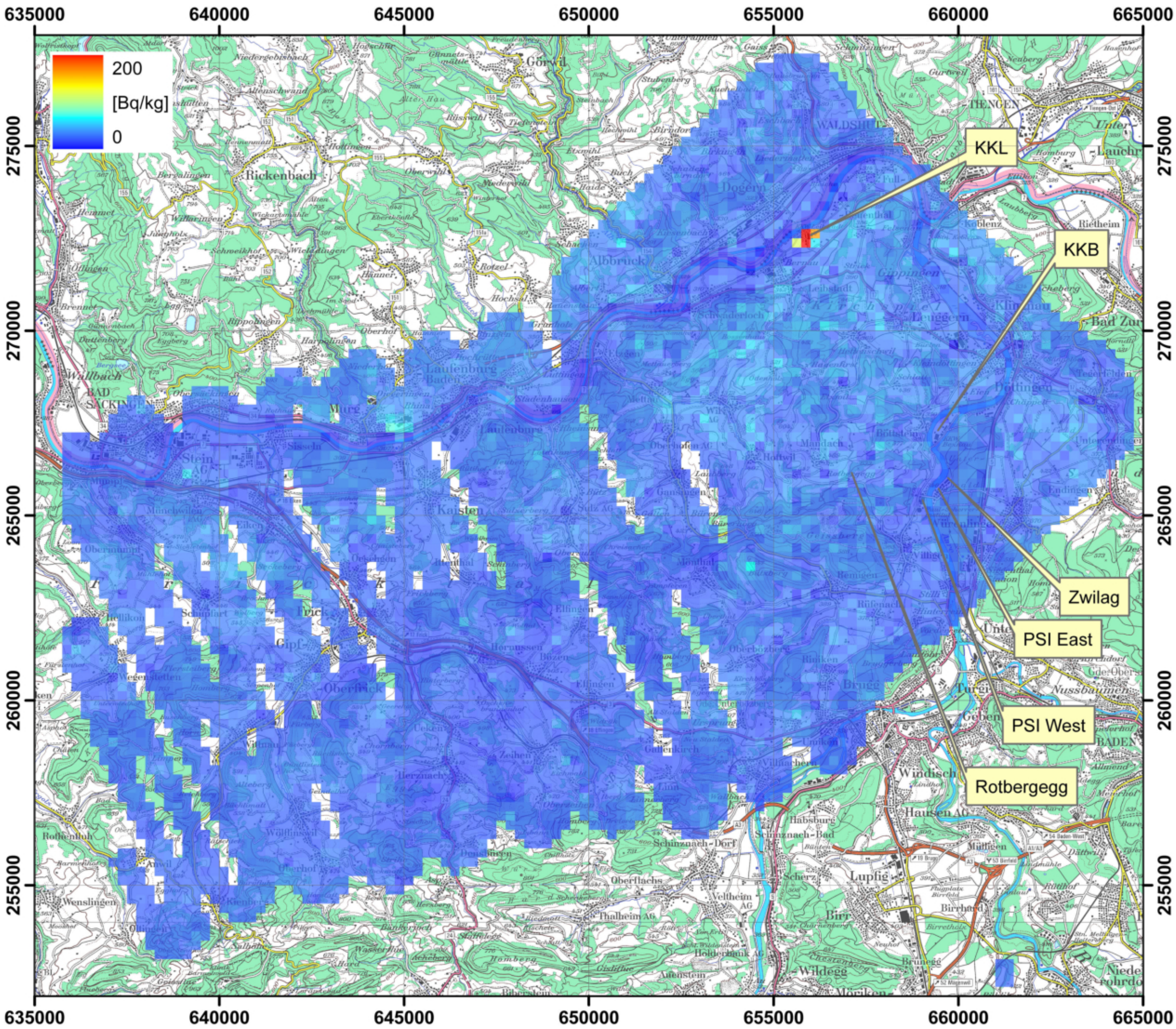

Figure 9: ^{238}U activity concentration in the vicinity of KKB, KKL, PSI and Zwilag. The high ^{238}U activity concentrations depicted over KKL are an artefact caused by a misinterpretation of photons emitted from ^{16}N.
PK100 ©2018 swisstopo (JD100042).

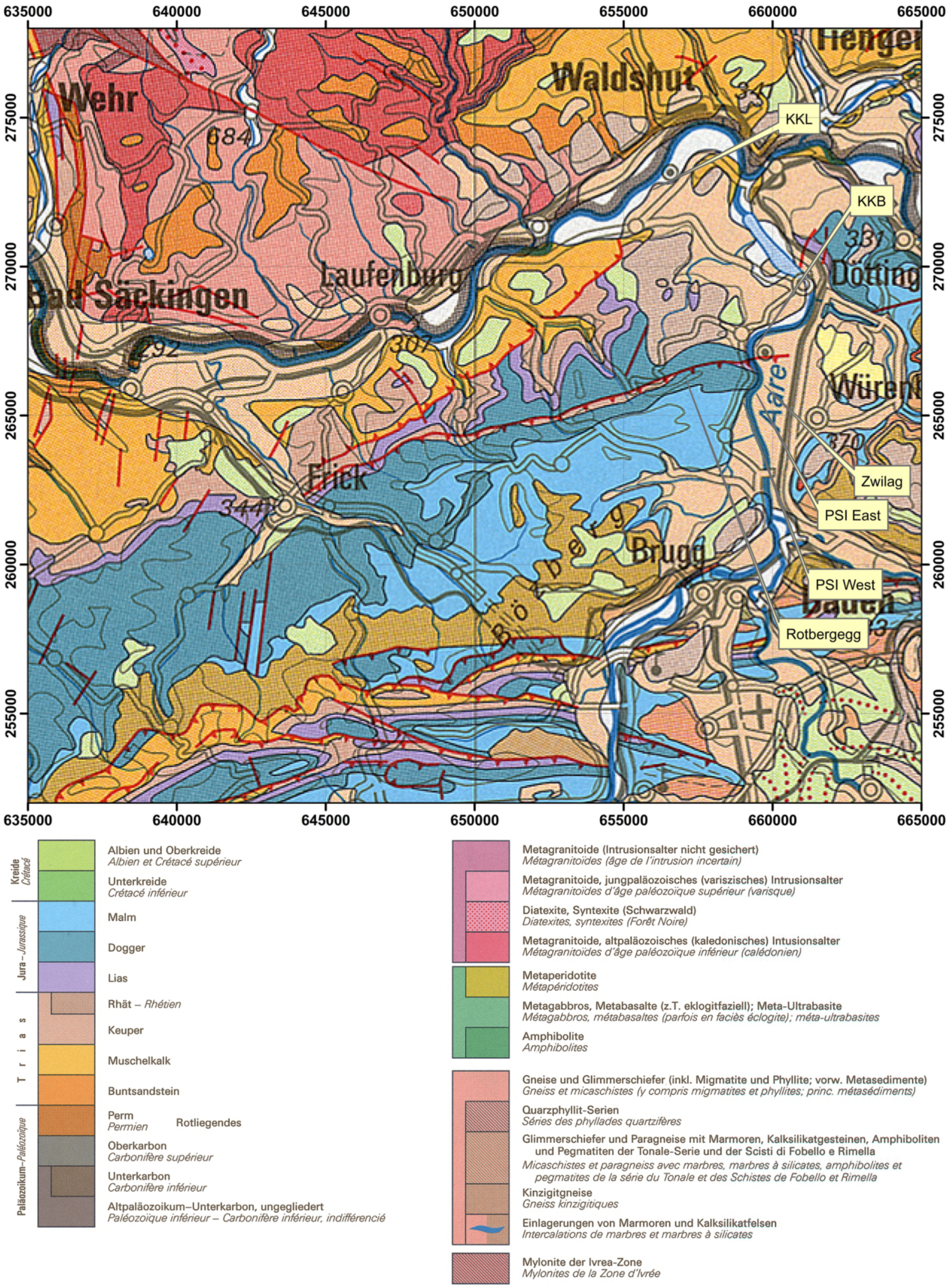

Figure 10: Geology in the vicinity of KKB, KKL, PSI and Zwilag with legend (in German). The Brown Jurassic is depicted in blue-gray color. Geologische Karte 1:500000 ©2018 swisstopo (JD100042).

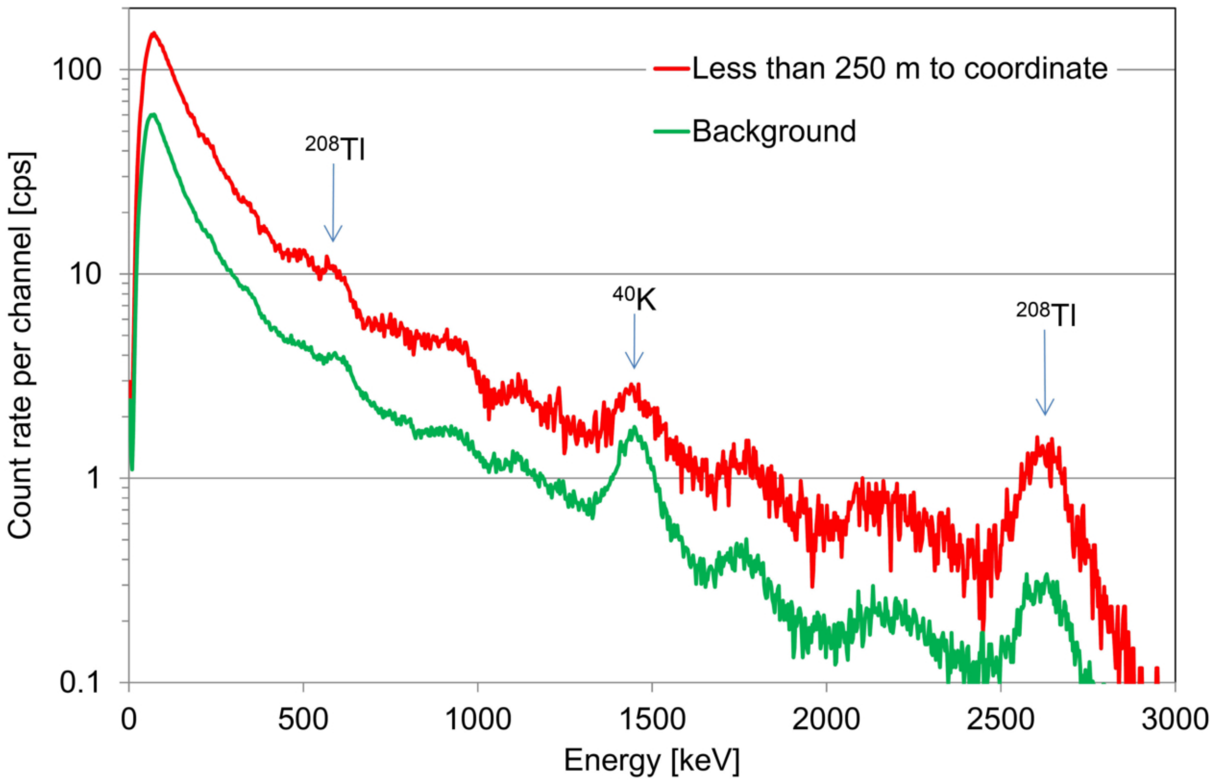

Figure 11: Photon spectrum over the vicinity of coordinates (644887, 267409) compared to a background spectrum.

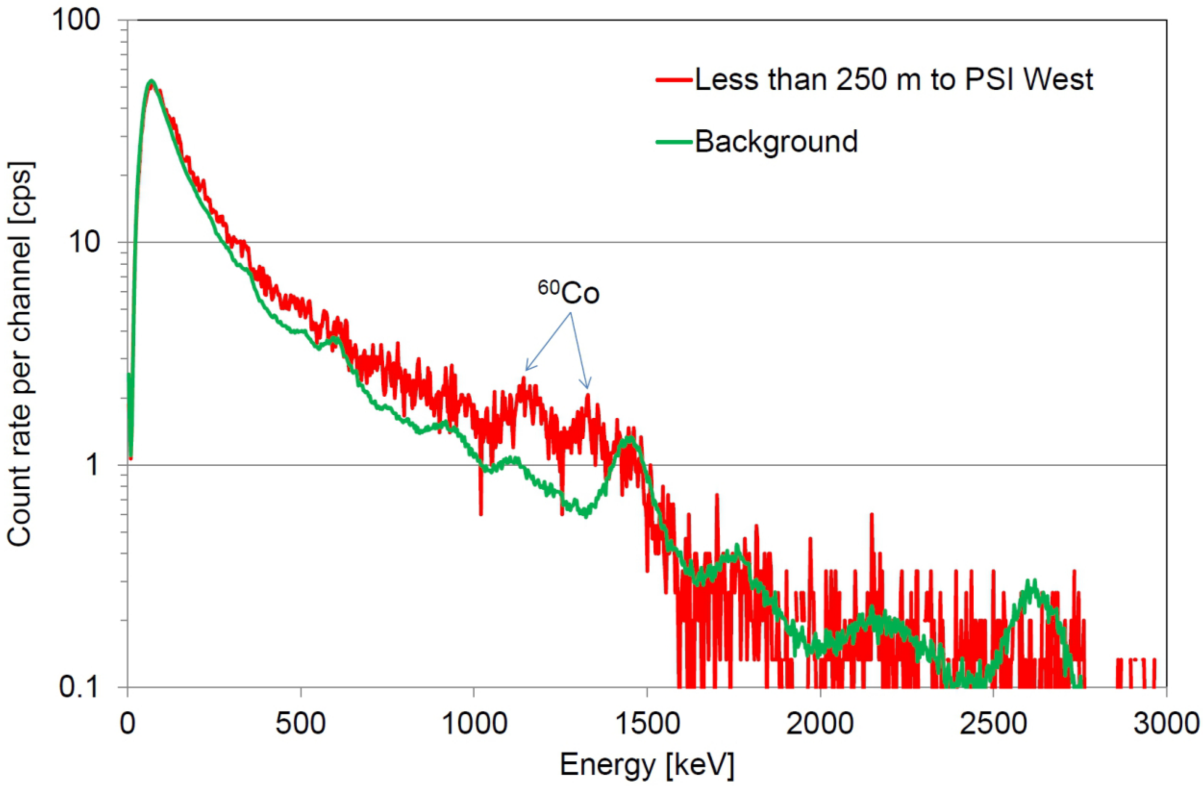

Figure 12: Photon spectrum over the accelerator building at PSI West compared to a background spectrum.

2.2 Fribourg and Solothurn

For the extension of the series of radiological background maps over Swiss cities, the vicinity of Fribourg and Solothurn was measured during ARM18z. The maps of the ambient dose rate (Figures 13 and 16) show reduced values over the measured areas of the Saane/Sarine and Aare Rivers, respectively. The dose rate reduction is caused by the attenuation of photon radiation originating from natural radionuclides in rock and soil in the overlaying water layer. The maps of the MMGC-ratio (Figures 14 and 17), an indicator for the presence of man-made radionuclides, do not show any elevated values in the measured areas. The maps of the ^{232}Th activity concentration (Figures 15 and 18) depict typical values over land and reduced readings over the rivers due to the attenuation of the water layer.

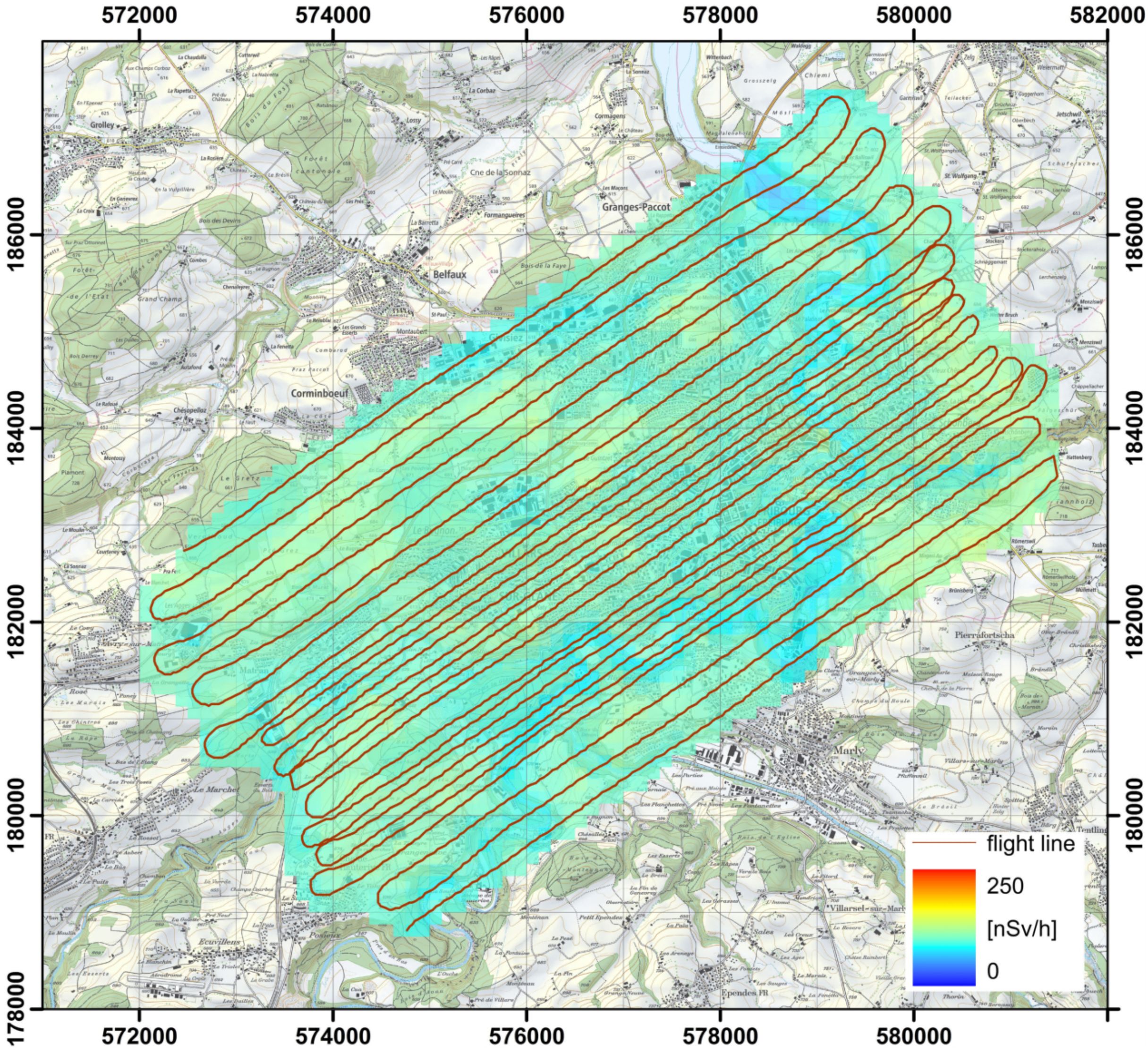

Figure 13: Dose rate in the vicinity of Fribourg.
PK25 ©2018 swisstopo (JD100042).

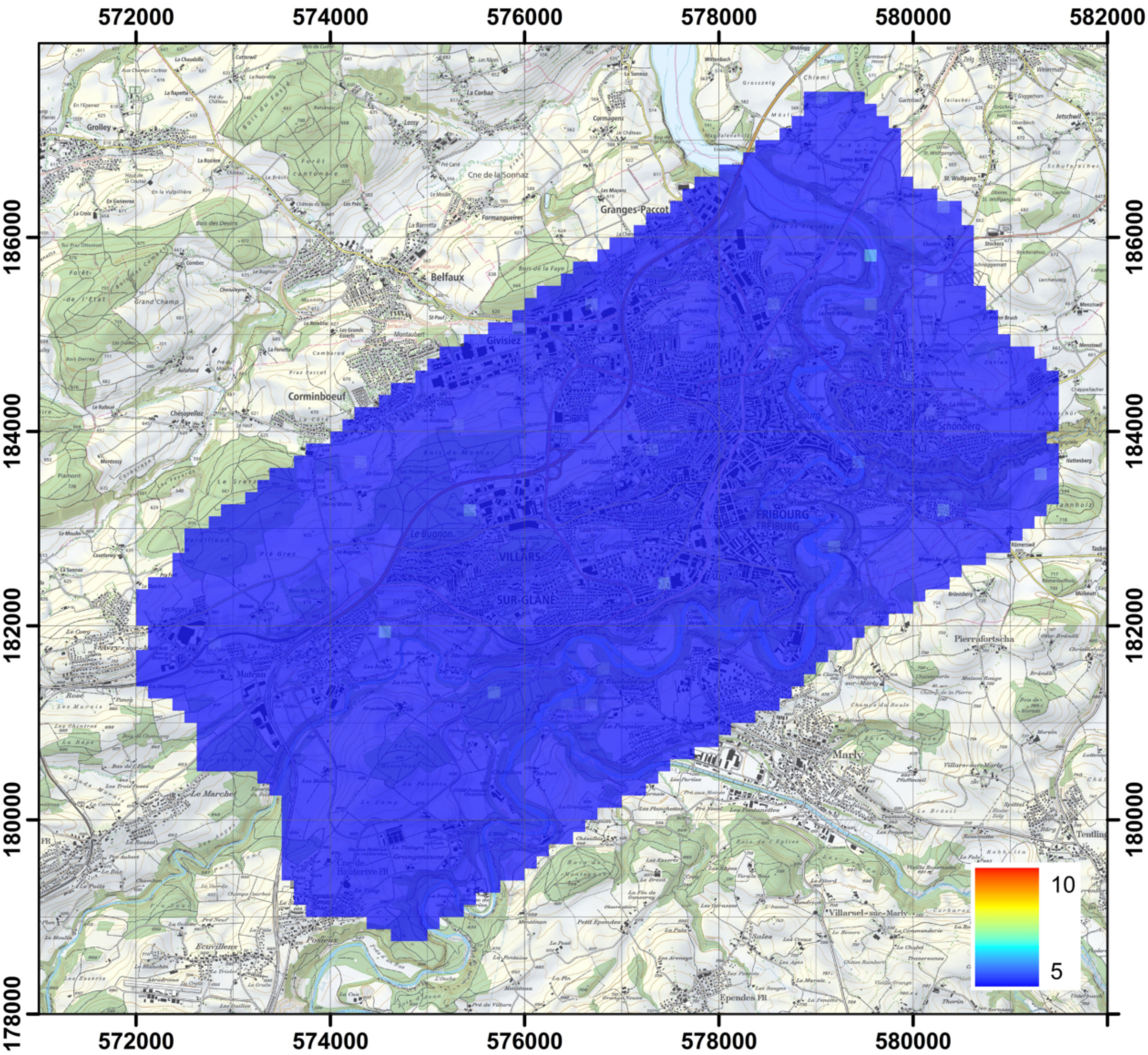

Figure 14: MMGC-ratio in the vicinity of Fribourg.
PK25 ©2018 swisstopo (JD100042).

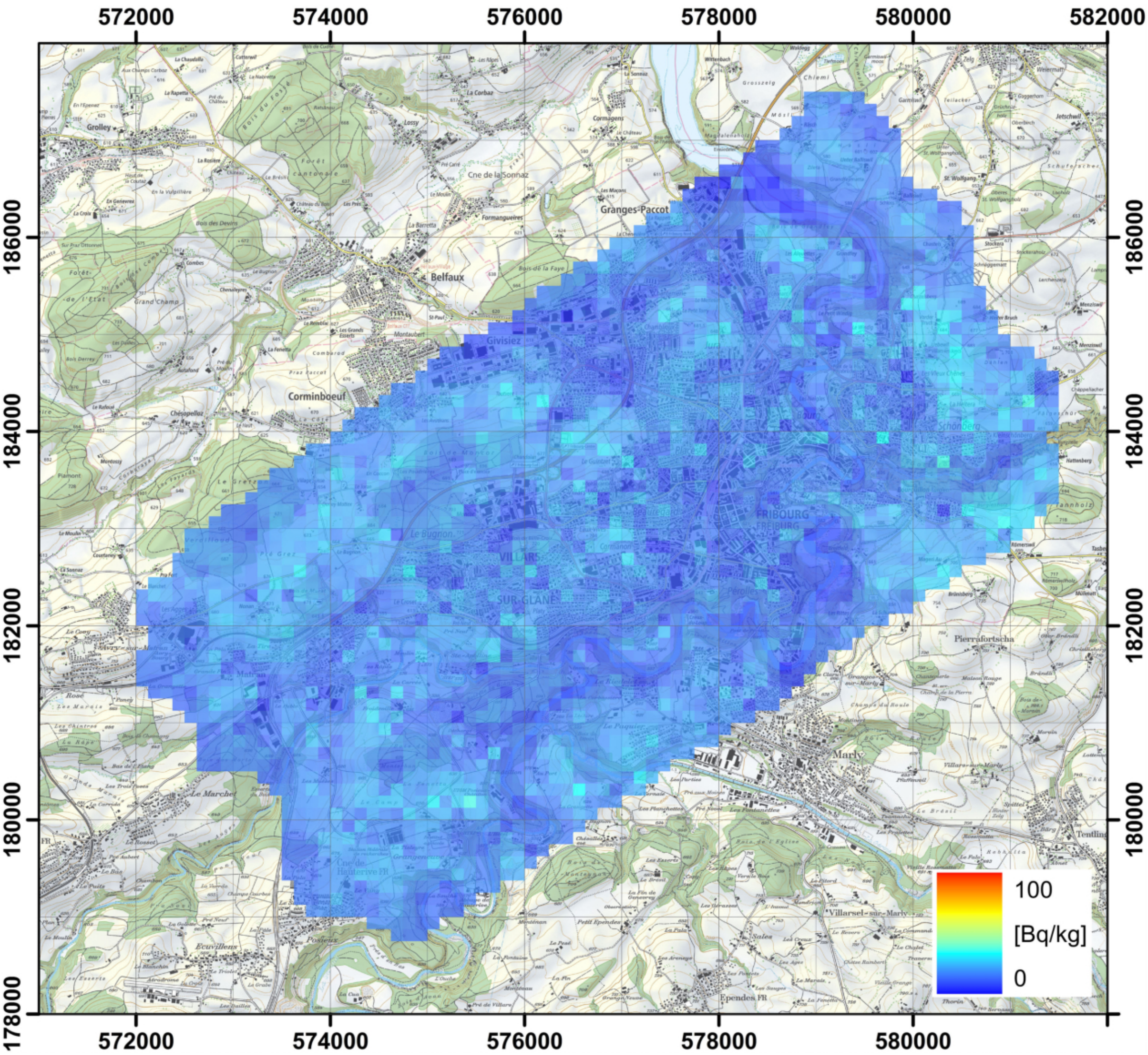

Figure 15: ^{232}Th activity concentration in the vicinity of Fribourg.
PK25 ©2018 swisstopo (JD100042).

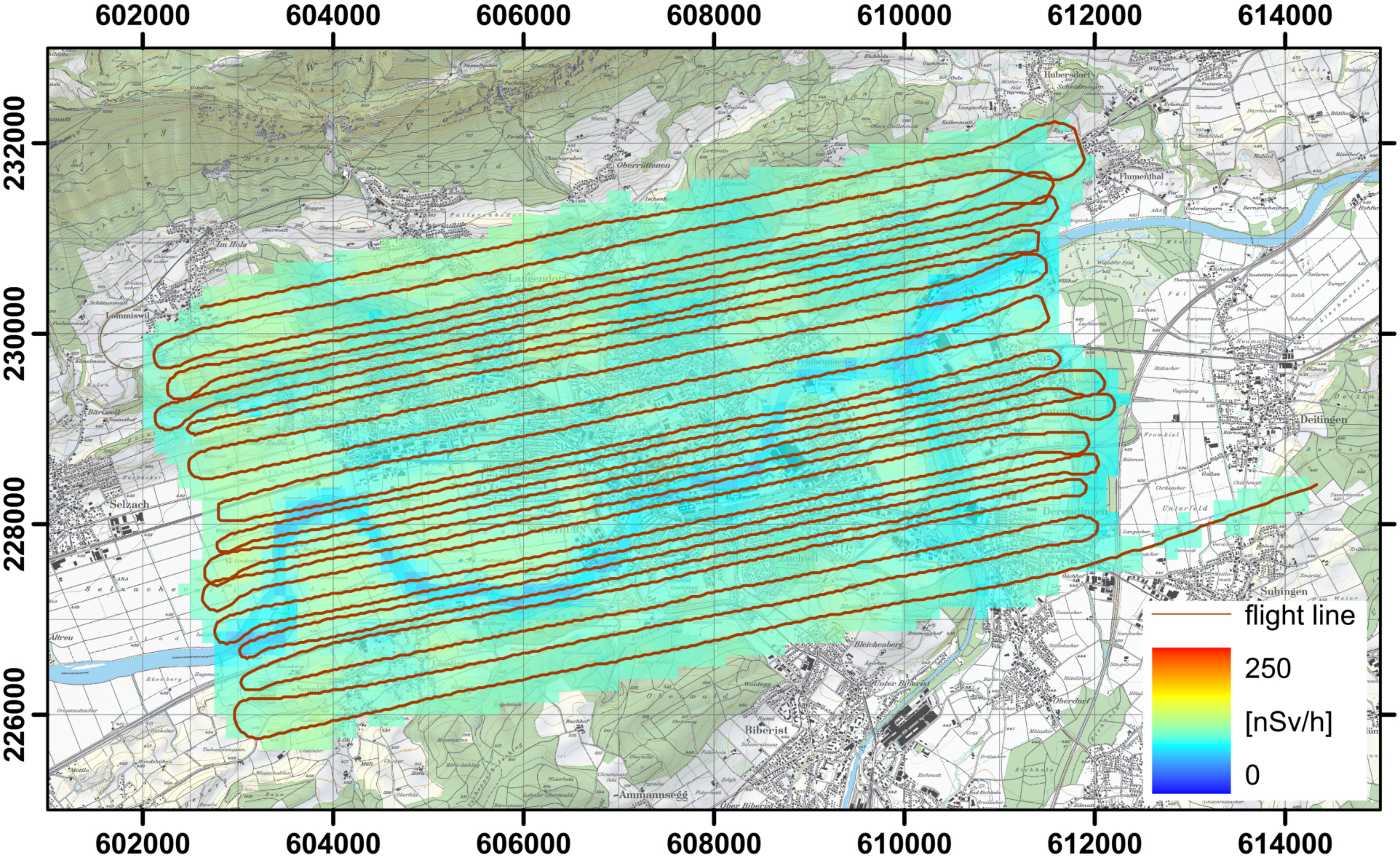

Figure 16: Dose rate in the vicinity of Solothurn. PK25 ©2018 swisstopo (JD100042).

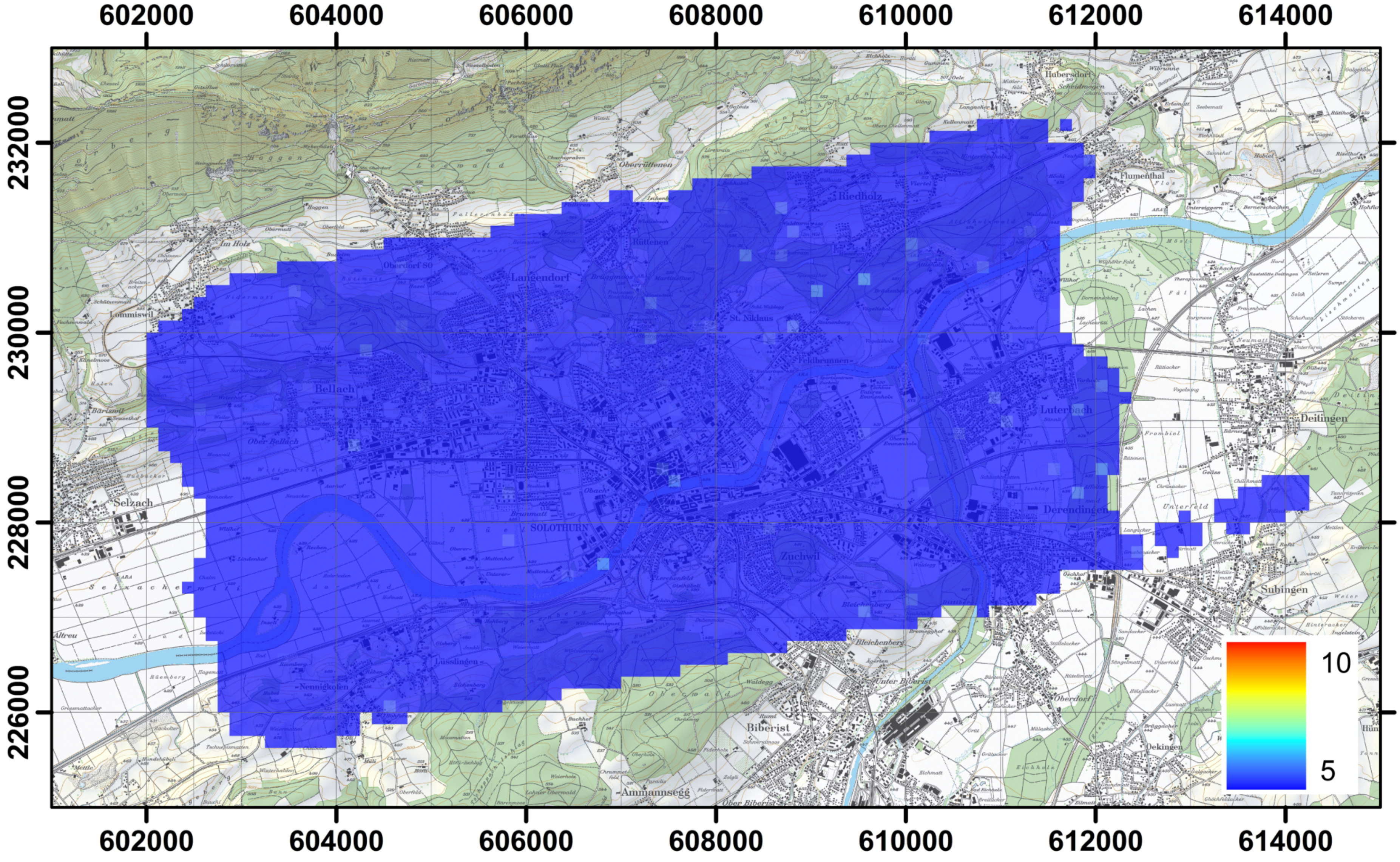

Figure 17: MMGC-ratio in the vicinity of Solothurn. PK25 ©2018 swisstopo (JD100042).

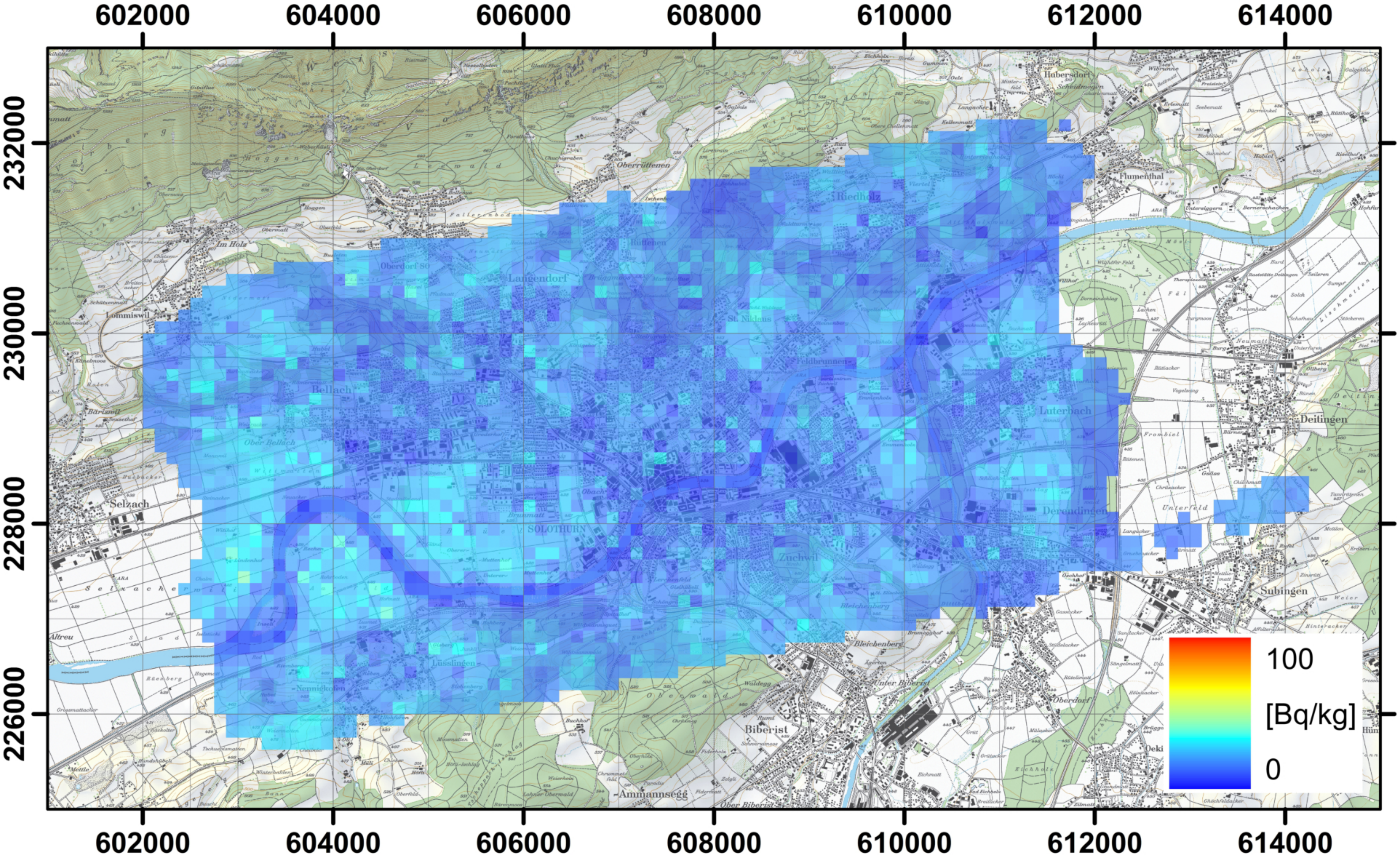

Figure 18: ^{232}Th activity concentration in the vicinity of Solothurn. PK25 ©2018 swisstopo (JD100042).

2.3 Yverdon-les-Bains

For the extension of the series of radiological background maps over Swiss cities, the vicinity of Yverdon-les-Bains was measured by the team of NBC-EOD Centre of Competence (KompZen ABC-Kamir) in Spring 2018. The measured raw data were evaluated with both the proprietary evaluation software of the manufacturer of the RLL system (Mirion) and the data evaluation software developed for the previous ARM system (MGS32). The maps of the ambient dose rate (Figures 19 and 20) show reduced values over Lake Neuchâtel. The dose rate reduction is caused by the attenuation of photon radiation originating from natural radionuclides in rock and soil in the overlaying water layer. The maps of the dose rate derived by both data evaluations are very similar. The contours are more clearly expressed in the map obtained with the ARM (MGS32) software compared to the RLL (Mirion) evaluation. This behaviour could be expected as the ARM (MGS32) data evaluation is based on raw spectra with a measuring time of one second, whereas the RLL (Mirion) software uses moving averages over a measuring time of five seconds.

For a detailed comparison, the frequency distributions of evaluated dose rates of all data points were generated for both evaluations (figure 26). The frequency distributions derived from the two data evaluations of identical raw data show two peaks, which can be associated with data points located over Lake Neuchâtel and ground without water attenuation. The peaks at 41 Sv/h (Mirion) and 52 nSv/h (MGS32) have a significantly different shape, indicating different computing strategies at very low dose rates. The difference between both distributions may be due to a constant offset or a difference between calibrations. A scatter plot of the data was used to investigate, which of these two explanations is more probable. Figure 27 shows a scatter plot of the calculated dose rate values with both programs together with a linear regression of the data. The same scatter plot is shown in figure 28, but compared to a linear regression with fixed intercept chosen to render a slope of one. Both models represent the data well with coefficients of determination of 0.893 and 0.89, respectively. Thus, a simple offset between both data evaluations of 10.6 nSv/h would be consistent with the observed data. Due to the results during the exercise ARM2017, the MGS32 calculation of cosmic dose rate was adapted to include also the dose rate caused by neutron radiation. The revised formula leads to an increase of dose rate of 7.5 nSv/h at the altitude of Yverdon-les-Bains of 435 m compared to the old calculation of cosmic dose rate, roughly the same difference as observed between the Mirion and MGS32 evaluation.

The map of the MMGC-ratio (figure 21), an indicator for the presence of man-made radionuclides, does not show any elevated values in the measured area. The MMGC-ratio is directly calculated from the raw spectra, thus both evaluation programs should yield identical values. As MGS32 was programmed originally for a spectral resolution of 256 channels, the spectra obtained by the RLL system at a resolution of 1024 channels are transformed to this lower resolution. The energy windows are also defined with the lower resolution, leading to slight differences in the calculation of the MMGC-ratio between both evaluation programs. Nevertheless, these small differences would not be detectable in the map of the MMGC-ratio, therefore only one of the maps is presented.

The maps of the ^{232}Th activity concentration (Figures 22 and 23) depict typical values over land and reduced readings over the lake due to the attenuation of the water layer. The according frequency distributions (figure 29) show a bimodal distribution, which can be associated with data points over ground and water. The peaks around an activity concentration of zero differ in shape indicating a different approach to the treatment of low values in the evaluation programs. Analogous to the dose rate, scatter plots with two different linear trends were used to distinguish between a difference in calibration factor and a constant offset. With the exception of negative values, a linear trend fits the data well with a coefficient

of determination of 0.94 (figure 30). Forcing the intercept to render a slope of one yields a visibly worse fit with a coefficient of determination of 0.86 (figure 31). Thus, a difference of 20% in the calibration factors between both evaluation programs seems to be the most likely explanation. A comparison between the ARM measuring system and the RLL system during the exercise ARM16 yielded a difference of 18% between measured ^{232}Th activity concentrations. Together with the presented results, the conclusion can be drawn that this difference is associated with calibration factors used in the different evaluation softwares, whereas the detector efficiencies of the ARM and RLL measuring systems can be considered identical.
The findings for ^{232}Th activity concentration are reproduced for the maps of ^{40}K activity concentration (figures 24 and 25), the frequency distributions (figure 32) and the scatter plots (figures 33 and 34), leading to the conclusion of a difference in calibration factors of 27%.
The compensation of the influence of airborne radon progeny on the measurement of ^{238}U activity concentrations is still under investigation (see section 2.6.1). Therefore a detailed comparison of ^{238}U activity concentrations is not presented.

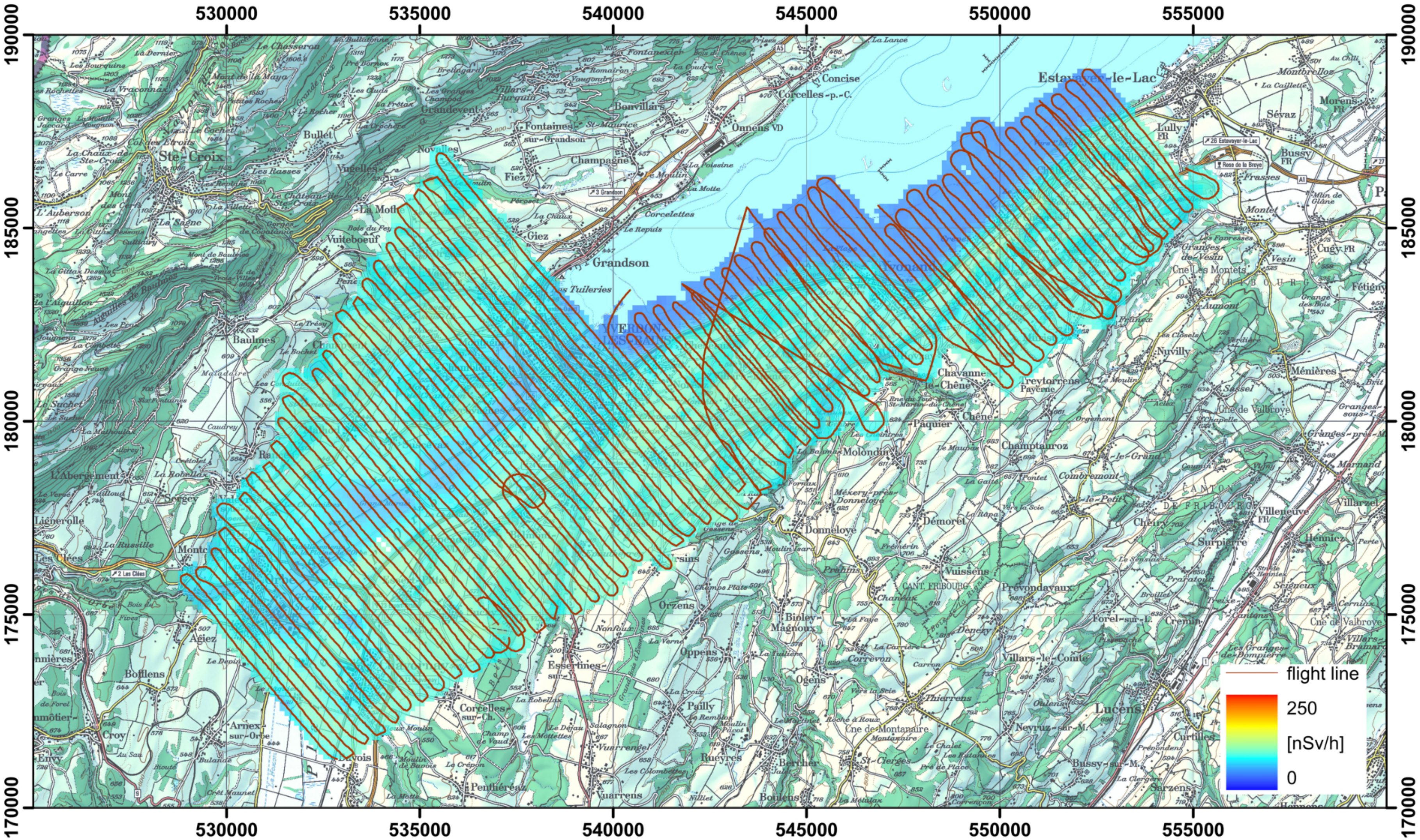

Figure 19: Dose rate in the vicinity of Yverdon-les-Bains. Data evaluated with the RLL (Mirion) software.
PK100 ©2018 swisstopo (JD100042).

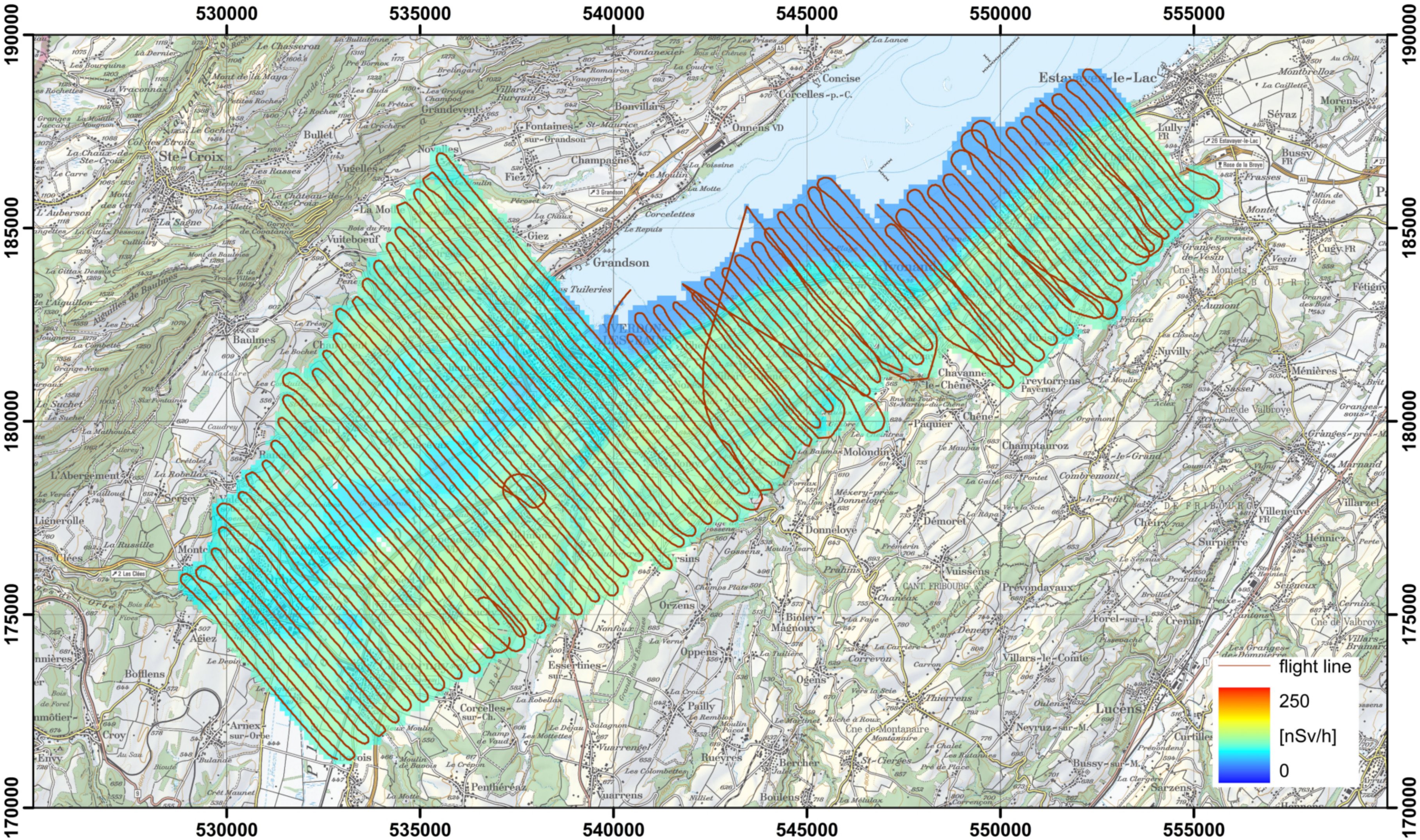

Figure 20: Dose rate in the vicinity of Yverdon-les-Bains. Data evaluated with the ARM (MGS32) software.
PK100 ©2018 swisstopo (JD100042).

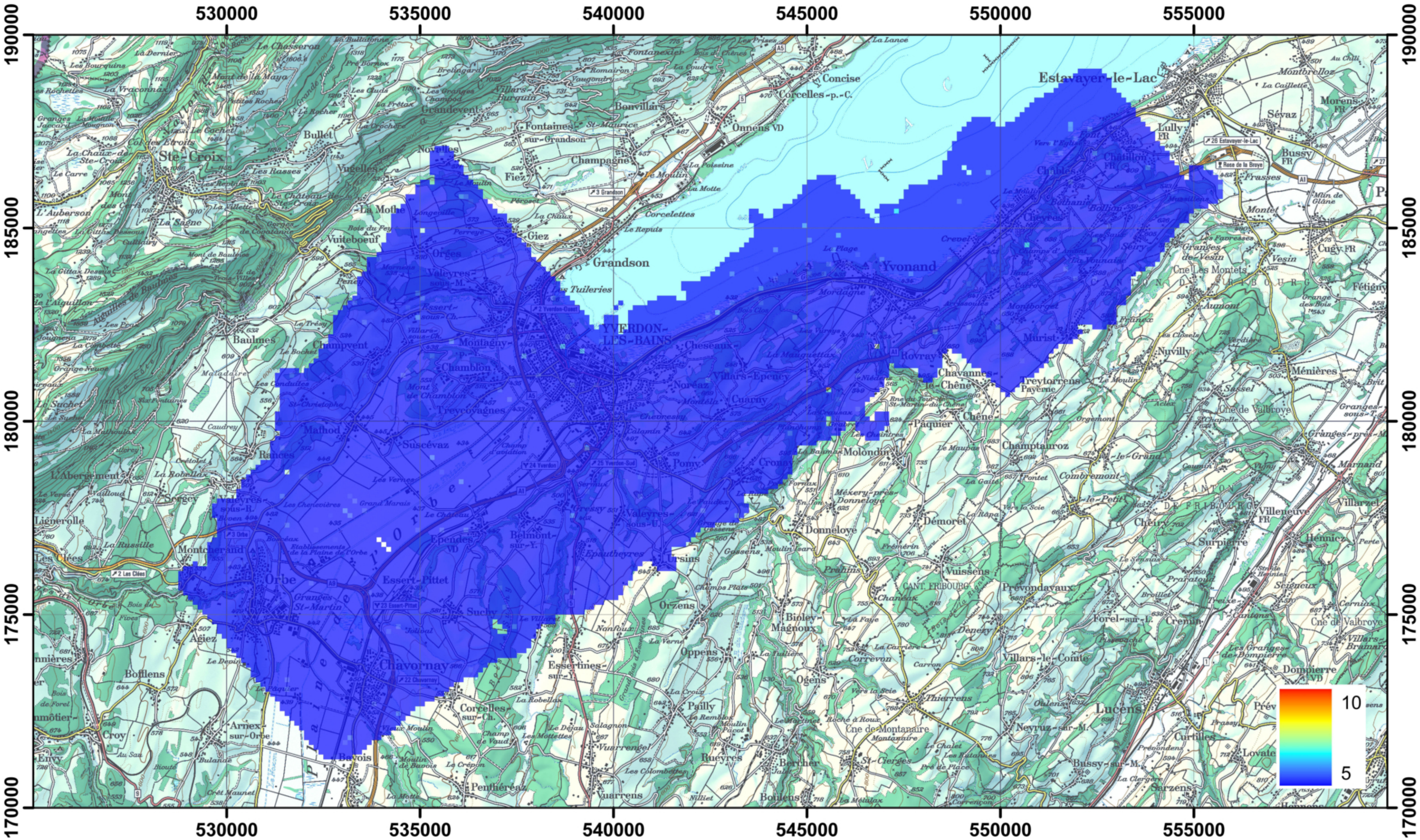

Figure 21: MMGC-ratio in the vicinity of Yverdon-les-Bains. Data evaluated with the RLL (Mirion) software.
PK100 ©2018 swisstopo (JD100042).

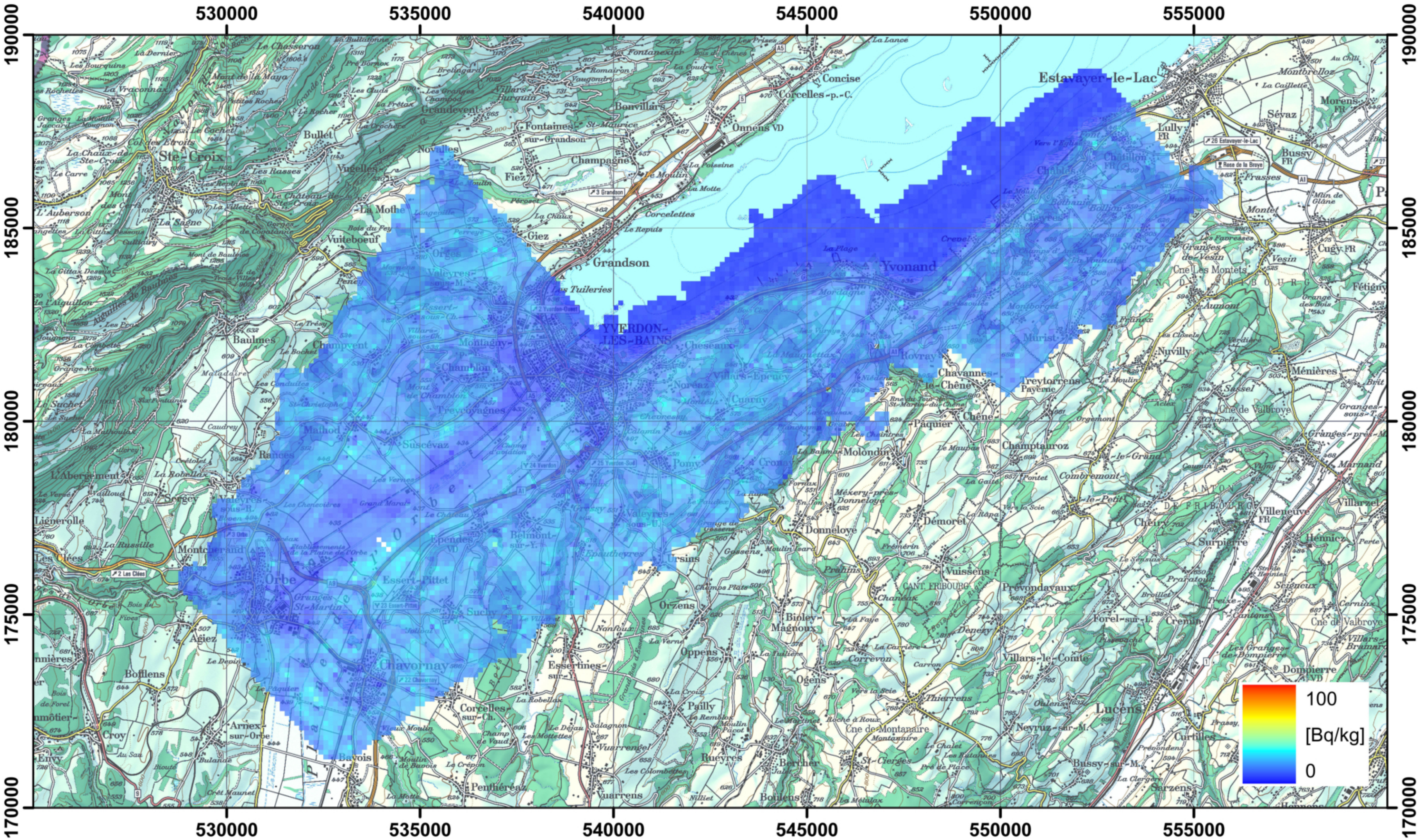

Figure 22: ^{232}Th activity concentration in the vicinity of Yverdon-les-Bains. Data evaluated with the RLL (Mirion) software. PK100 ©2018 swisstopo (JD100042).

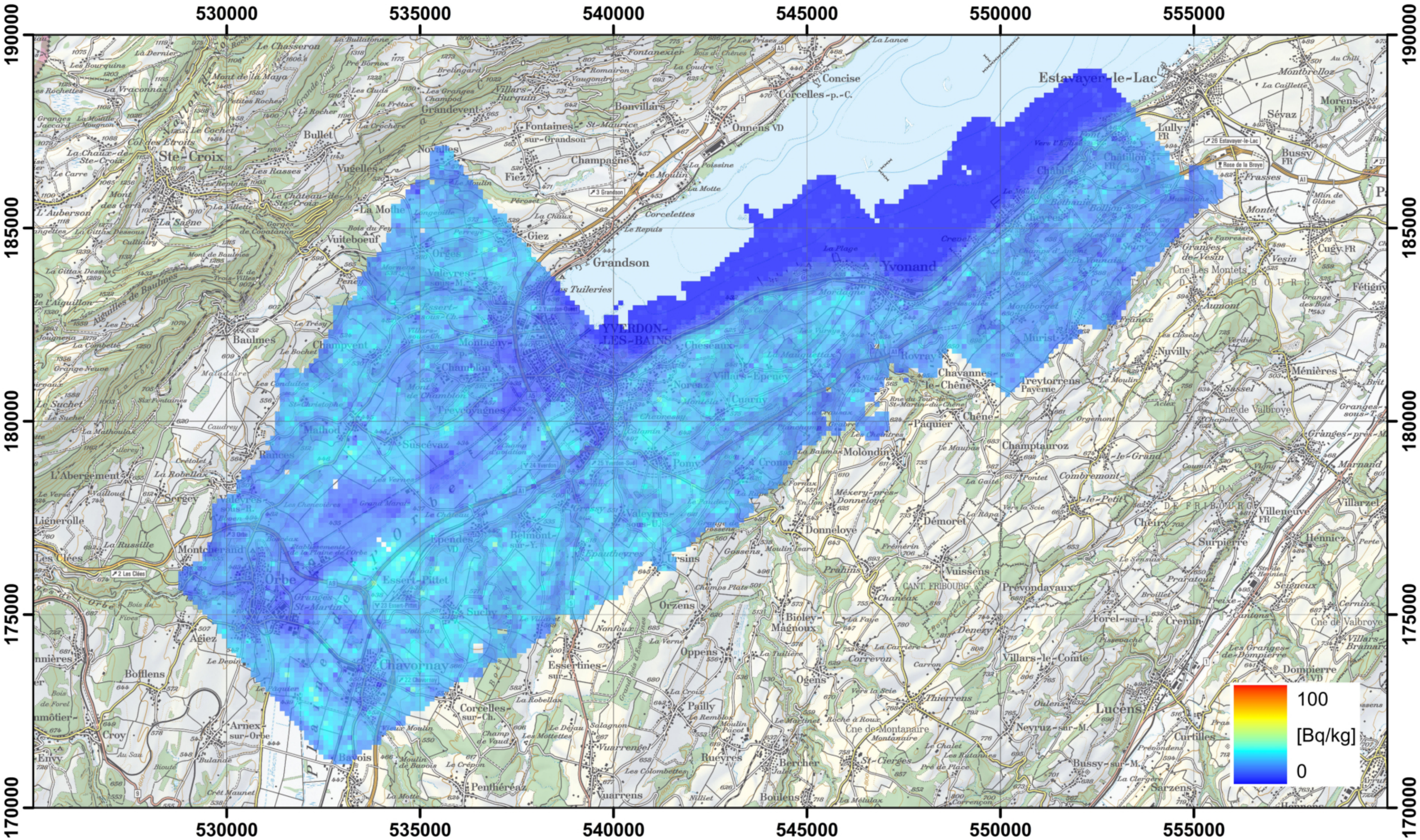

Figure 23: ^{232}Th activity concentration in the vicinity of Yverdon-les-Bains. Data evaluated with the ARM (MGS32) software. PK100 ©2018 swisstopo (JD100042).

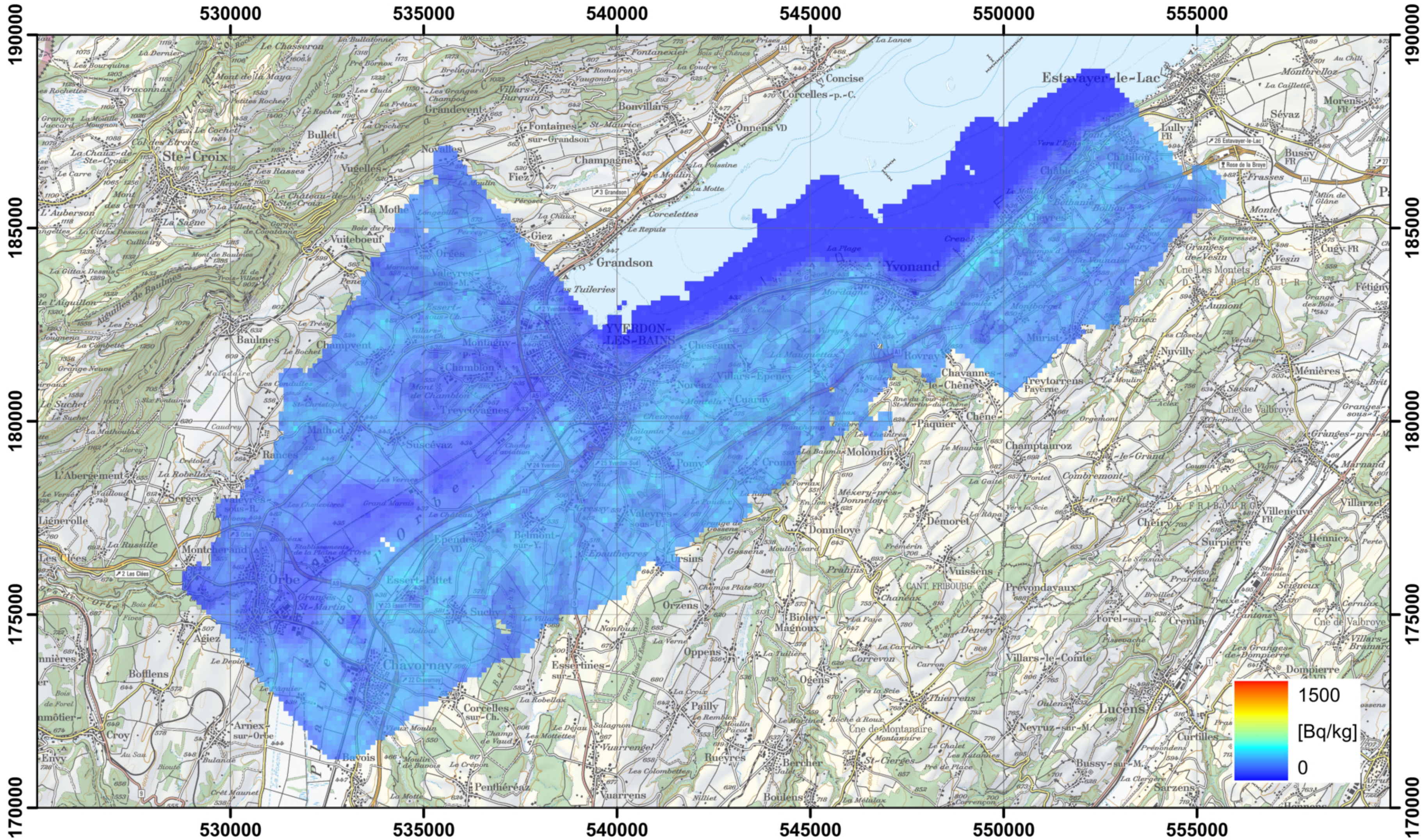

Figure 24: ^{40}K activity concentration in the vicinity of Yverdon-les-Bains. Data evaluated with the RLL (Mirion) software.
PK100 ©2018 swisstopo (JD100042).

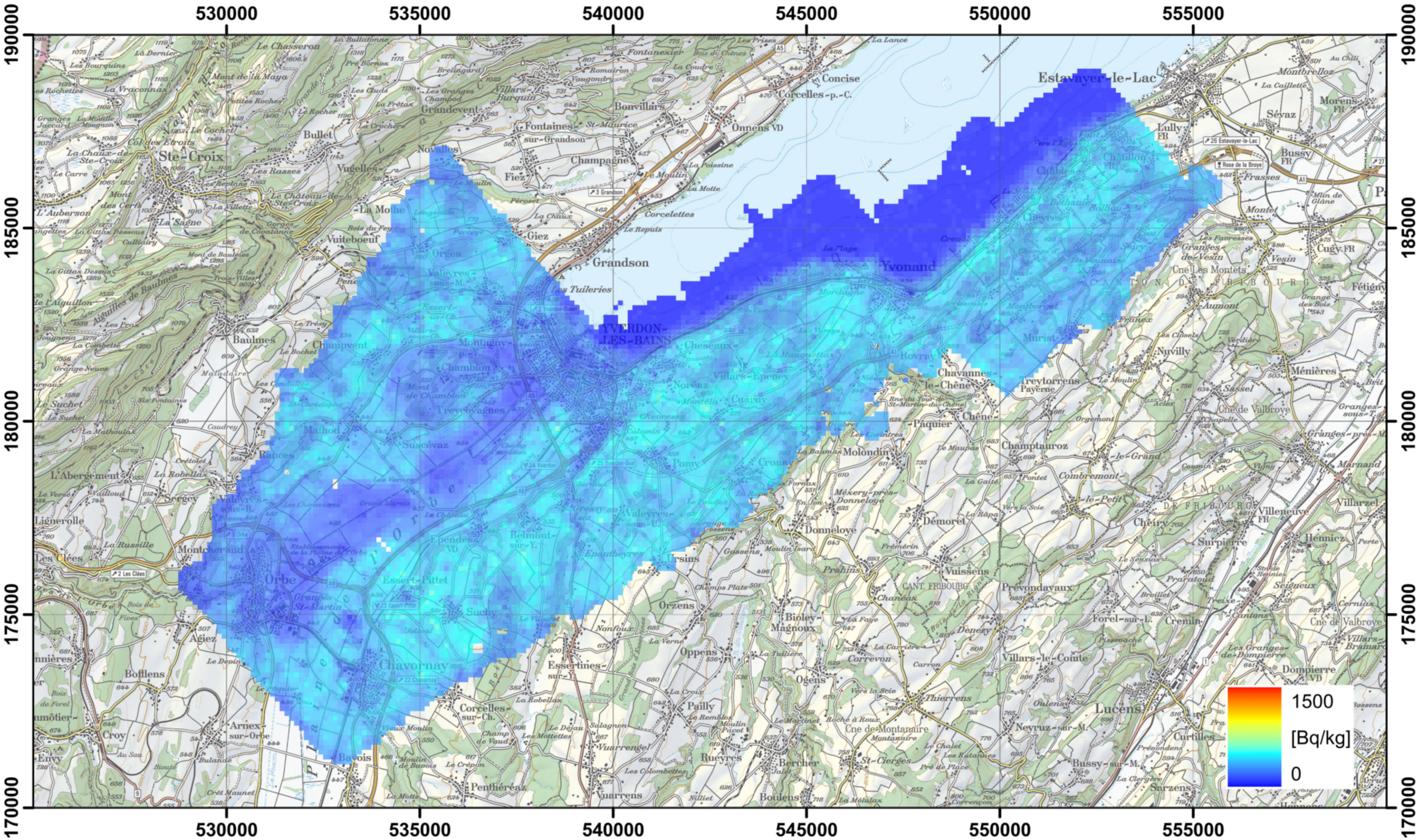

Figure 25: ^{40}K activity concentration in the vicinity of Yverdon-les-Bains. Data evaluated with the ARM (MGS32) software. PK100 ©2018 swisstopo (JD100042).

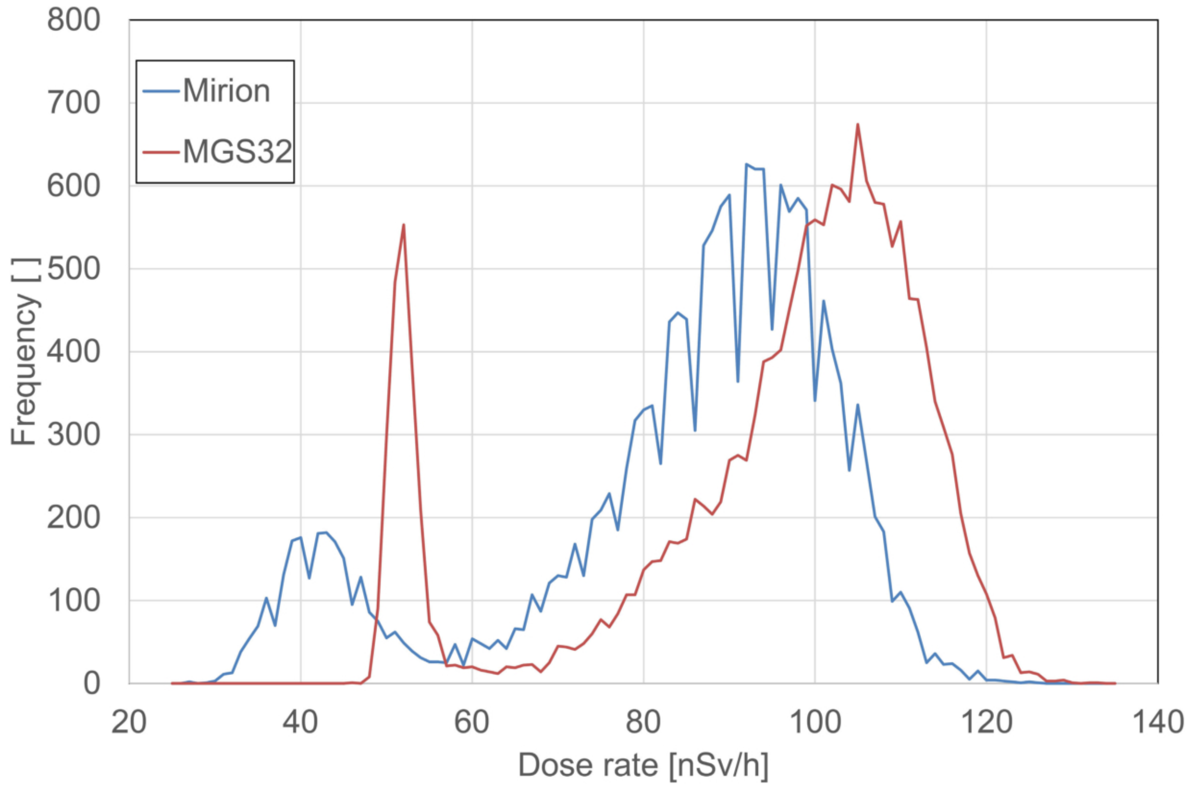

Figure 26: Frequency distributions of dose rates in the vicinity of Yverdon-les-Bains calculated with the RLL (Mirion) and ARM (MGS32) software.

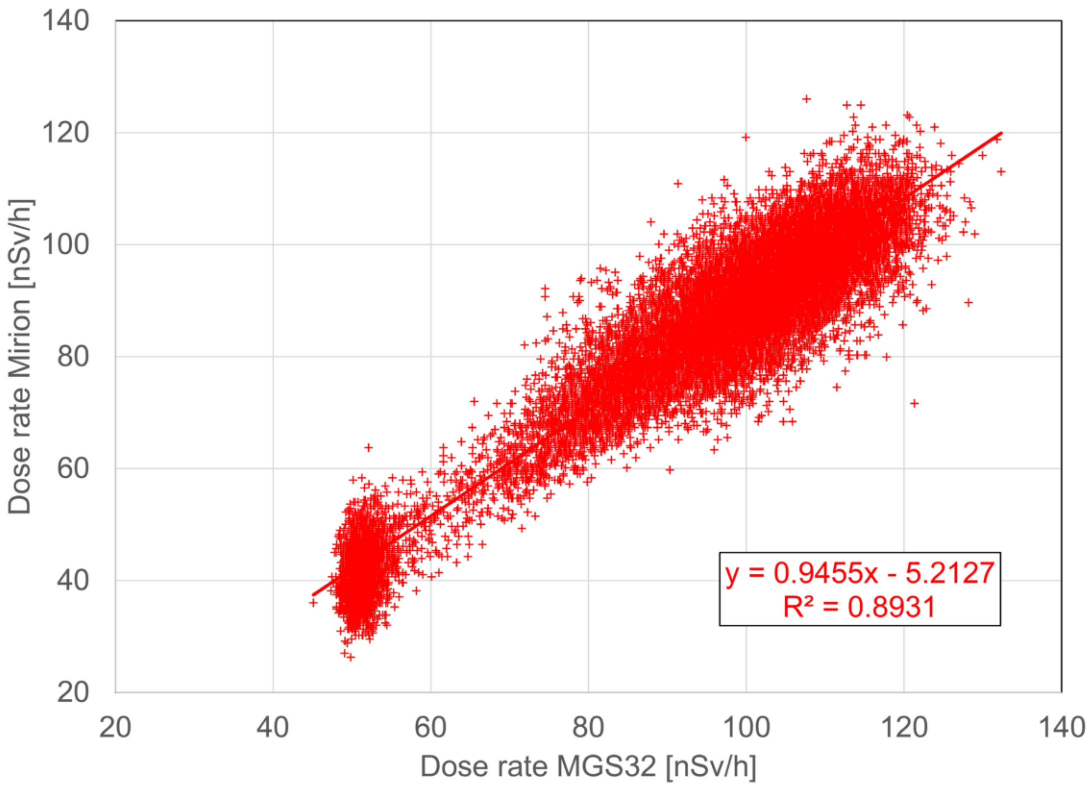

Figure 27: Scatter plot of dose rates in the vicinity of Yverdon-les-Bains calculated with the RLL (Mirion) and ARM (MGS32) software compared to a linear model.

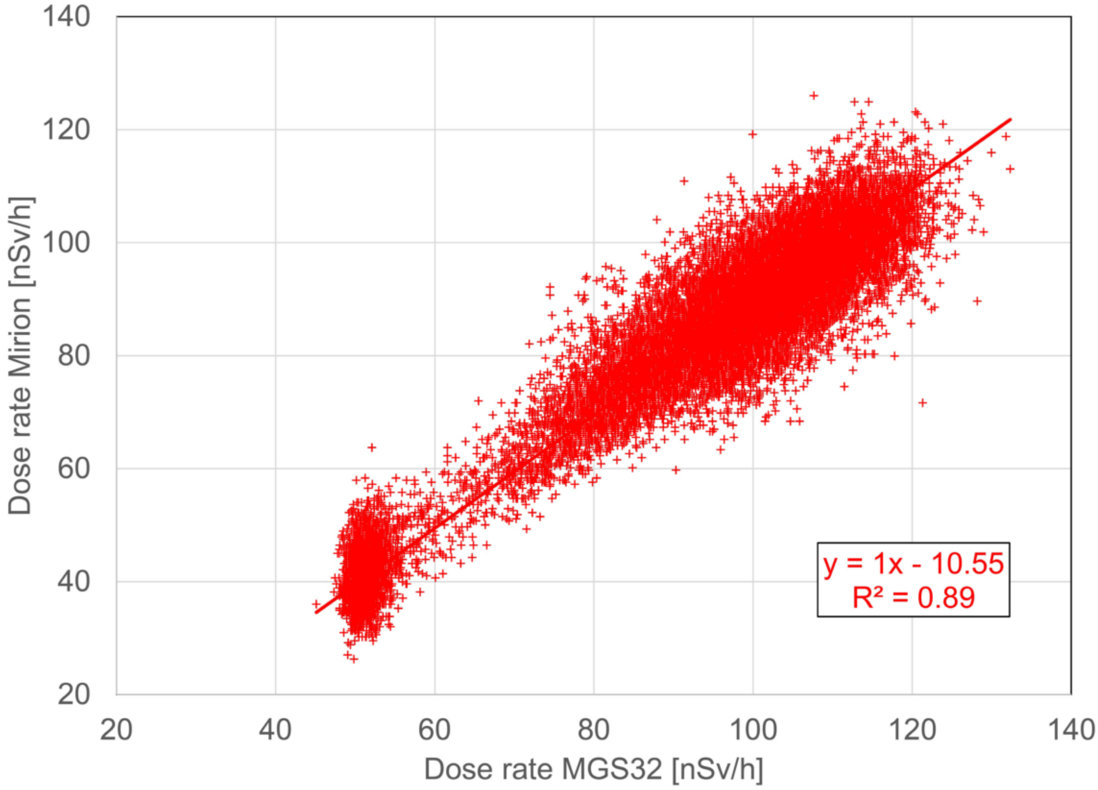

Figure 28: Scatter plot of dose rates in the vicinity of Yverdon-les-Bains calculated with the RLL (Mirion) and ARM (MGS32) software compared to a linear offset model.

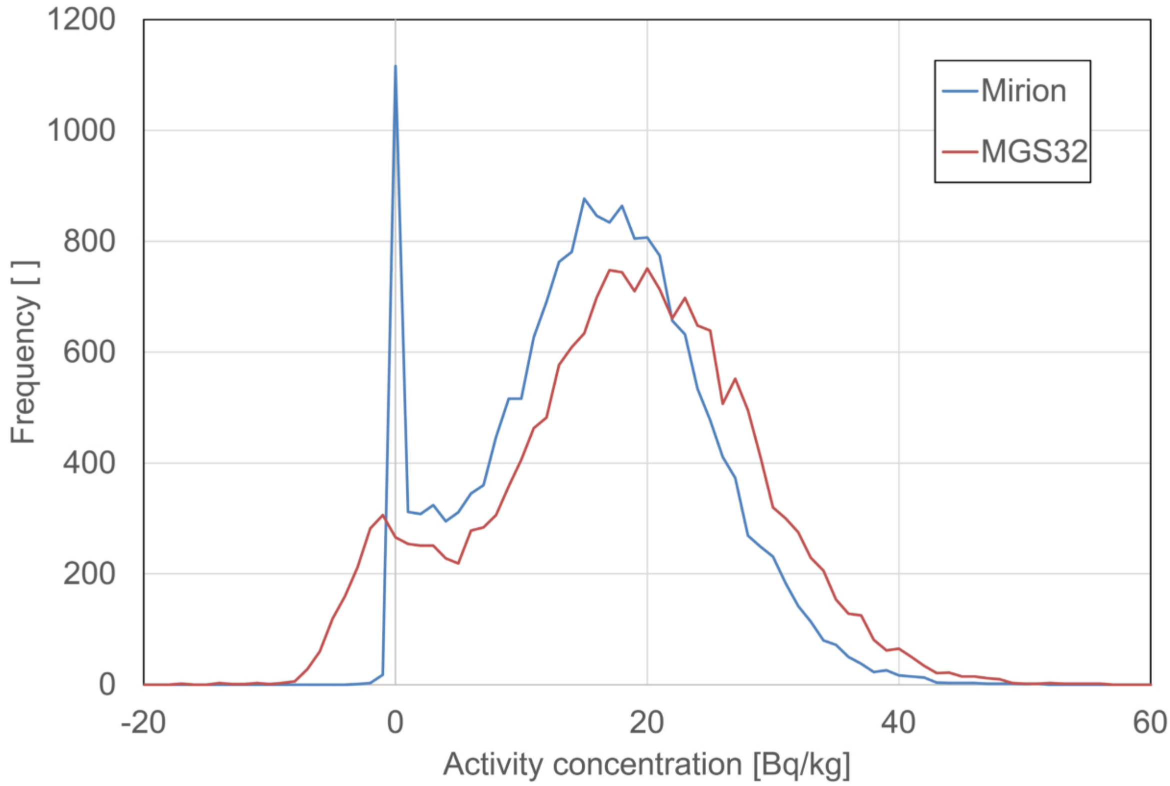

Figure 29: Frequency distributions of ^{232}Th activity concentration in the vicinity of Yverdon-les-Bains calculated with the RLL (Mirion) and ARM (MGS32) software.

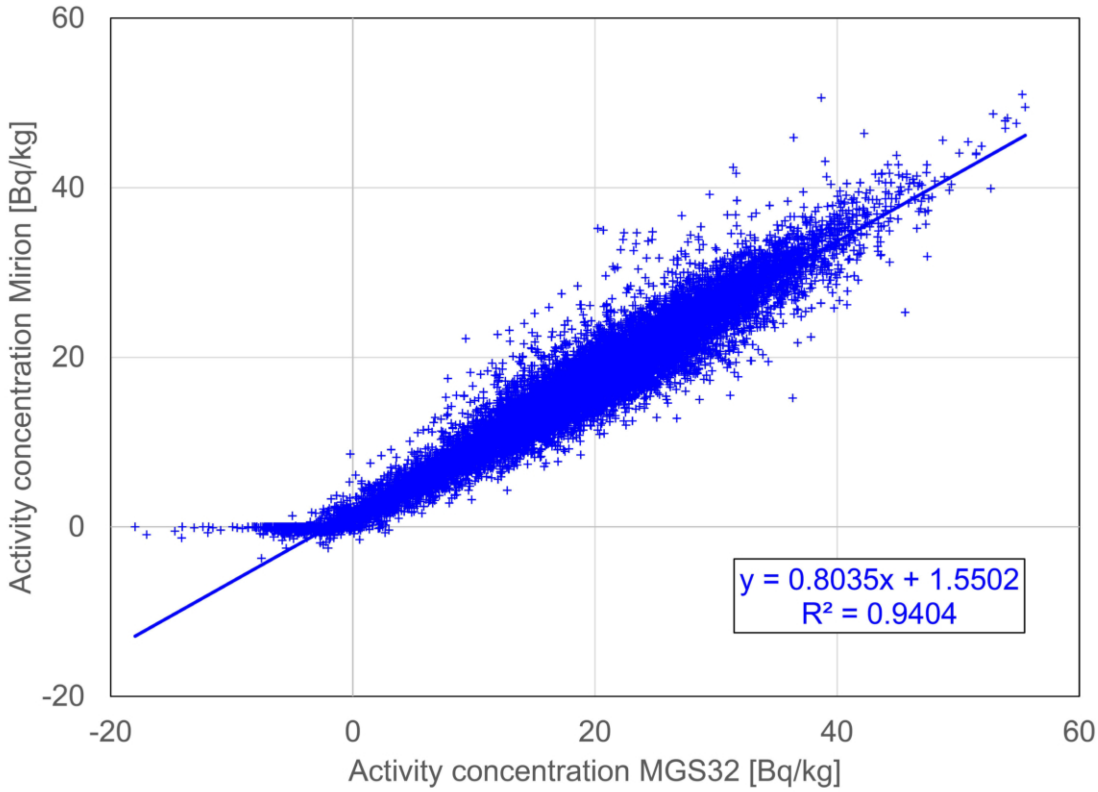

Figure 30: Scatter plot of ^{232}Th activity concentrations in the vicinity of Yverdon-les-Bains calculated with the RLL (Mirion) and ARM (MGS32) software compared to a linear model.

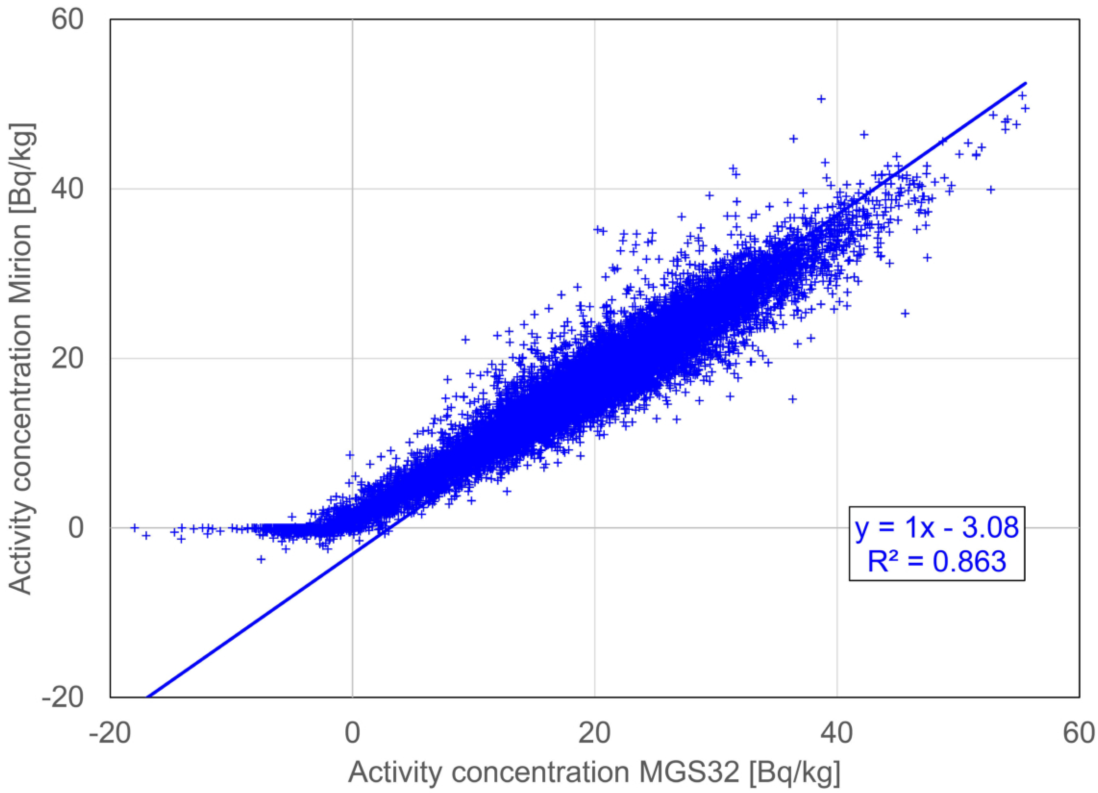

Figure 31: Scatter plot of ^{232}Th activity concentrations in the vicinity of Yverdon-les-Bains calculated with the RLL (Mirion) and ARM (MGS32) software compared to a linear offset model.

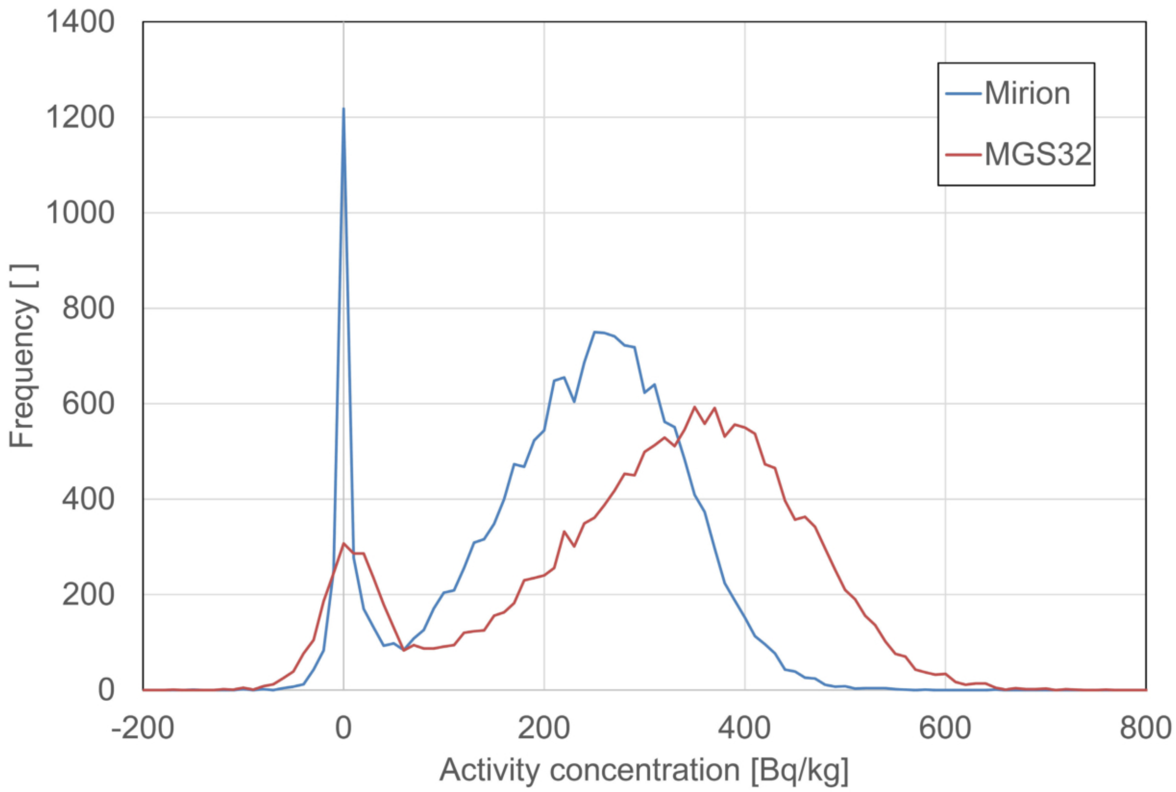

Figure 32: Frequency distributions of ^{40}K activity concentration in the vicinity of Yverdon-les-Bains calculated with the RLL (Mirion) and ARM (MGS32) software.

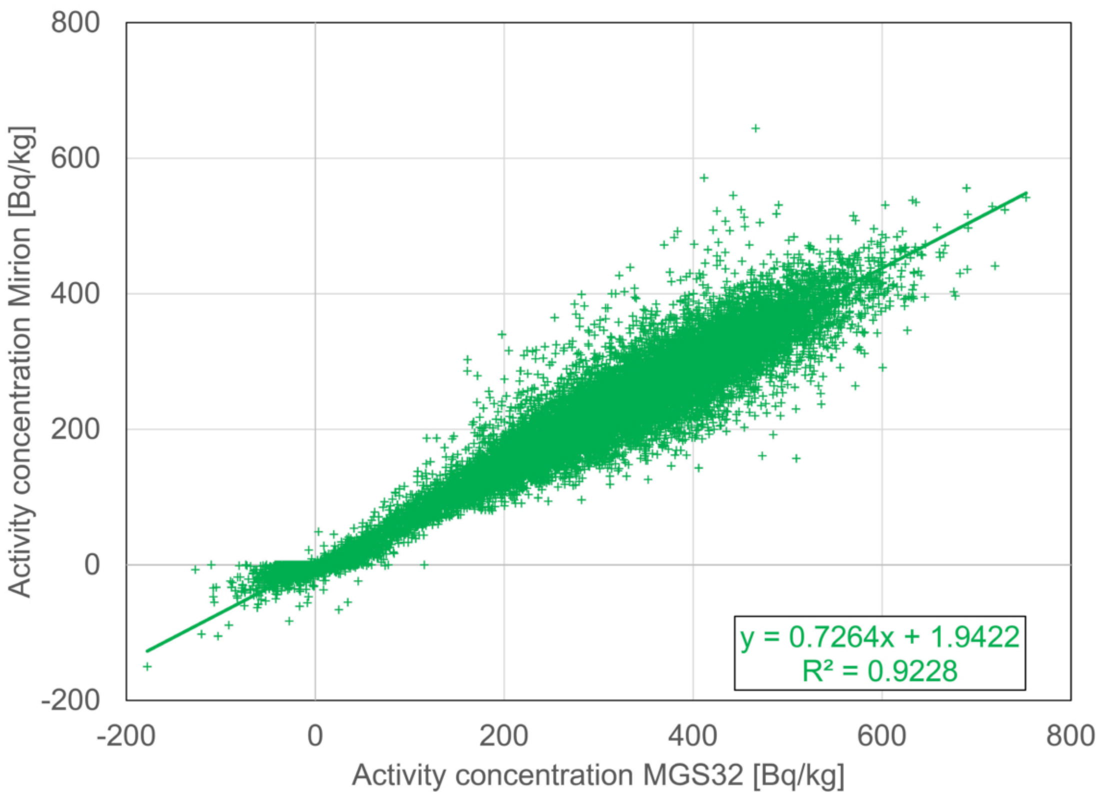

Figure 33: Scatter plot of ^{40}K activity concentrations in the vicinity of Yverdon-les-Bains calculated with the RLL (Mirion) and ARM (MGS32) software compared to a linear model.

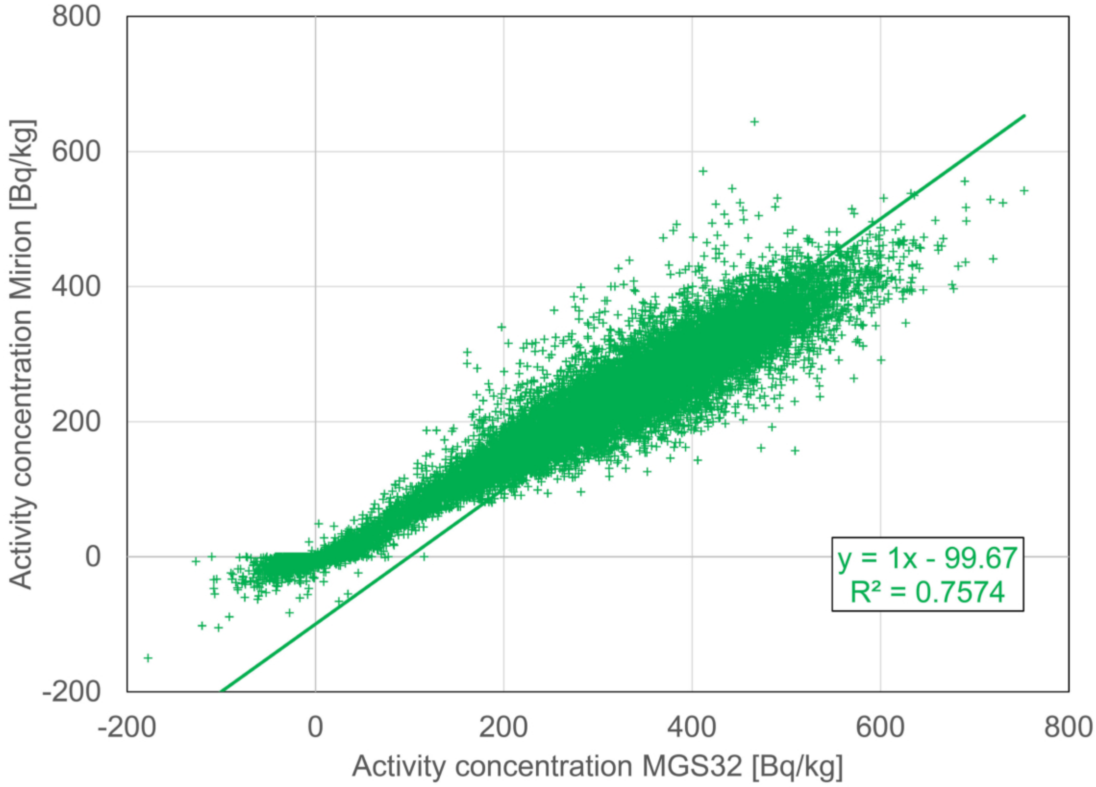

Figure 34: Scatter plot of ^{40}K activity concentrations in the vicinity of Yverdon-les-Bains calculated with the RLL (Mirion) and ARM (MGS32) software compared to a linear offset model.

2.4 Mont Vully

The region around Mont Vully at coordinates (573774, 201490) was inspected with airborne gammaspectrometry on request of the University of Basel. A PhD thesis of this University was investigating elevated concentrations of radionuclides of the natural uranium-radium series in springs and ditches around Mont Vully. The areas with slightly elevated values of total and terrestrial dose rate (figures 35 and 36) can be associated with elevated ^{40}K (figure 37) and ^{232}Th (figure 38) activity concentrations. The map of ^{238}U (figure 39) does not show distinct anomalies as expected from the elevated water concentrations. The soil layer associated with elevated concentrations of the uranium-radium series was identified during the thesis to be a peat layer. Overlaying the peat layer is a layer with normal uranium content of about 1 m thickness. The attenuation of photons originating from the peat layer in the overlaying soil can be assumed as cause for the lack of a clearer gammaspectrometric response.

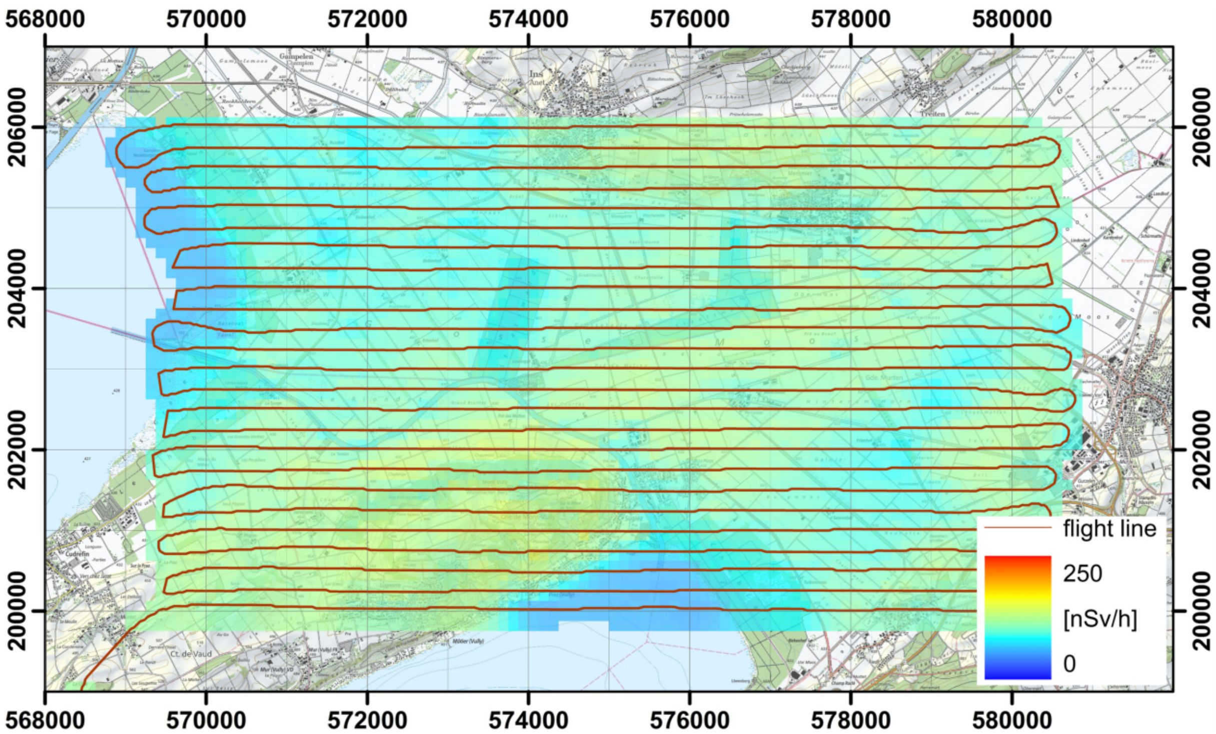

Figure 35: Dose rate in the vicinity of Mont Vully.
PK25 ©2018 swisstopo (JD100042).

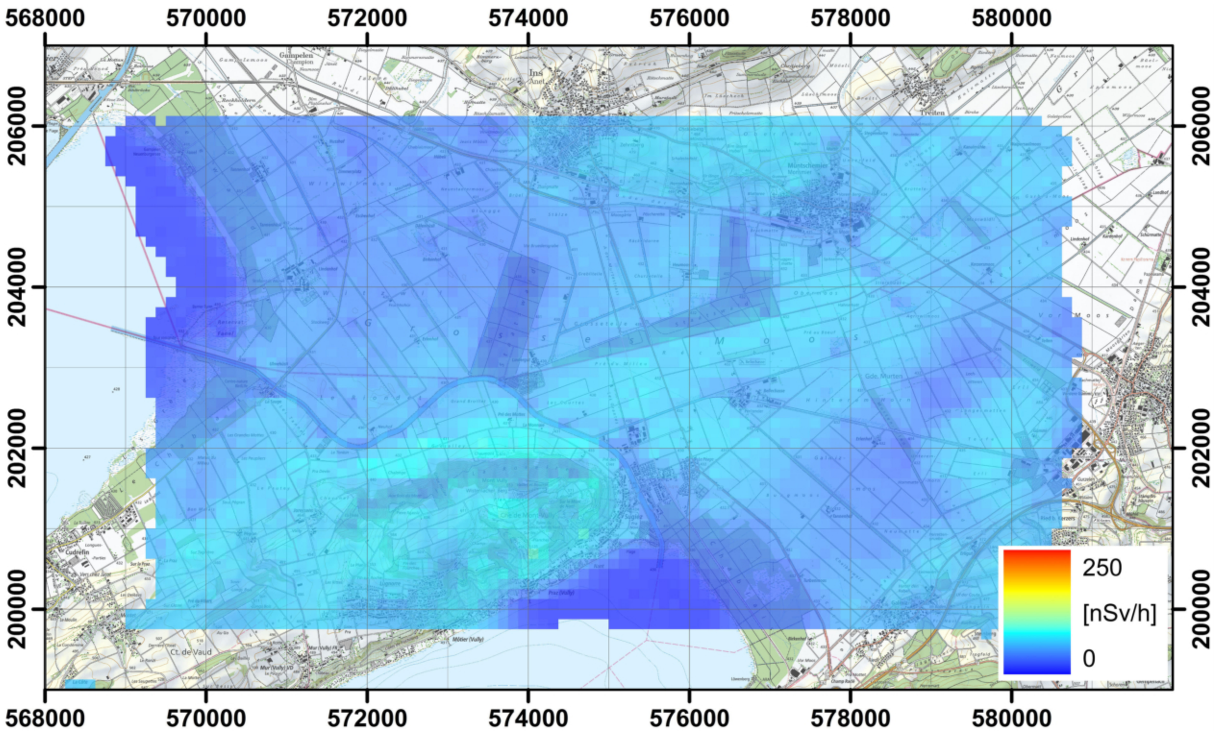

Figure 36: Terrestrial dose rate in the vicinity of Mont Vully.
PK25 ©2018 swisstopo (JD100042).

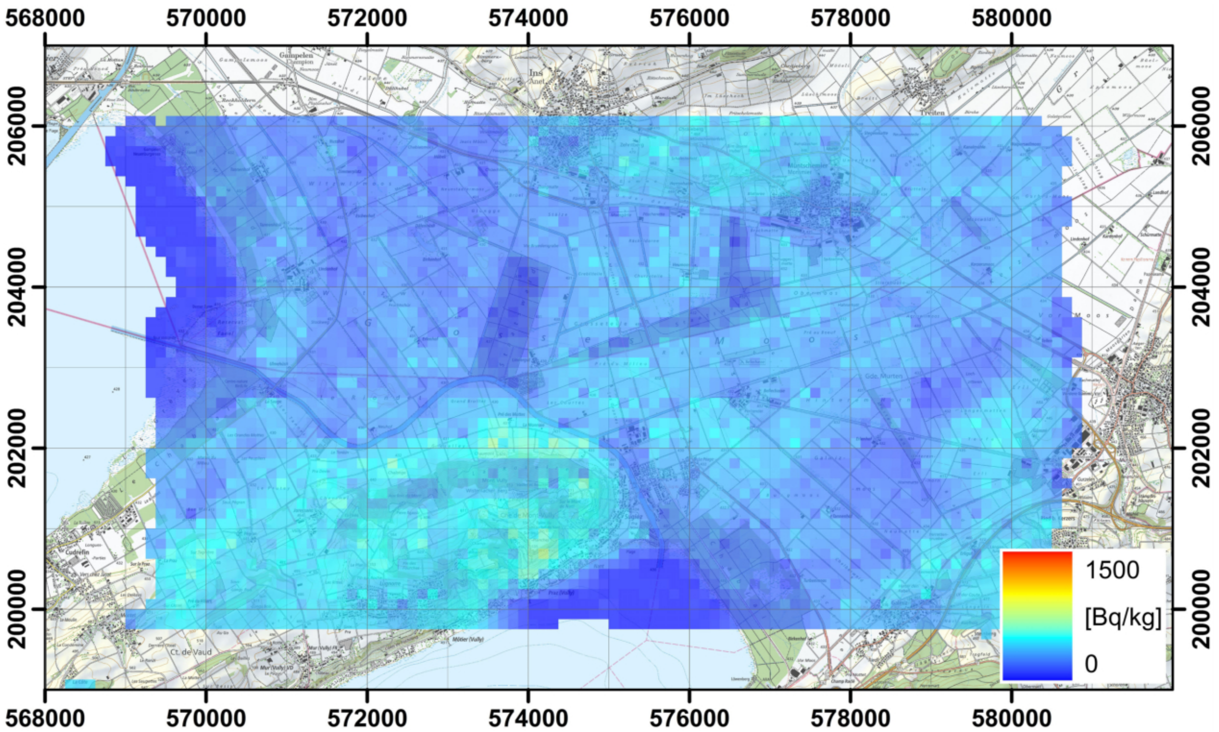

Figure 37: ^{40}K activity concentration in the vicinity of Mont Vully.
PK25 ©2018 swisstopo (JD100042).

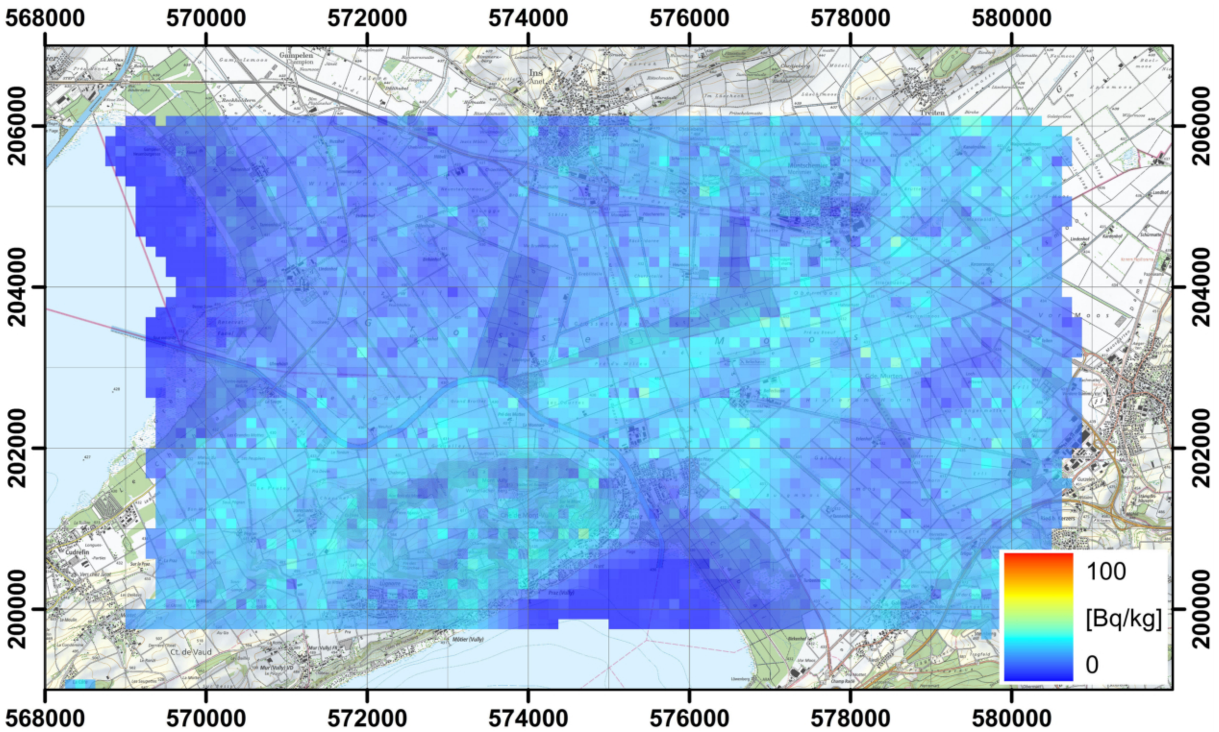

Figure 38: ^{232}Th activity concentration in the vicinity of Mont Vully.
PK25 ©2018 swisstopo (JD100042).

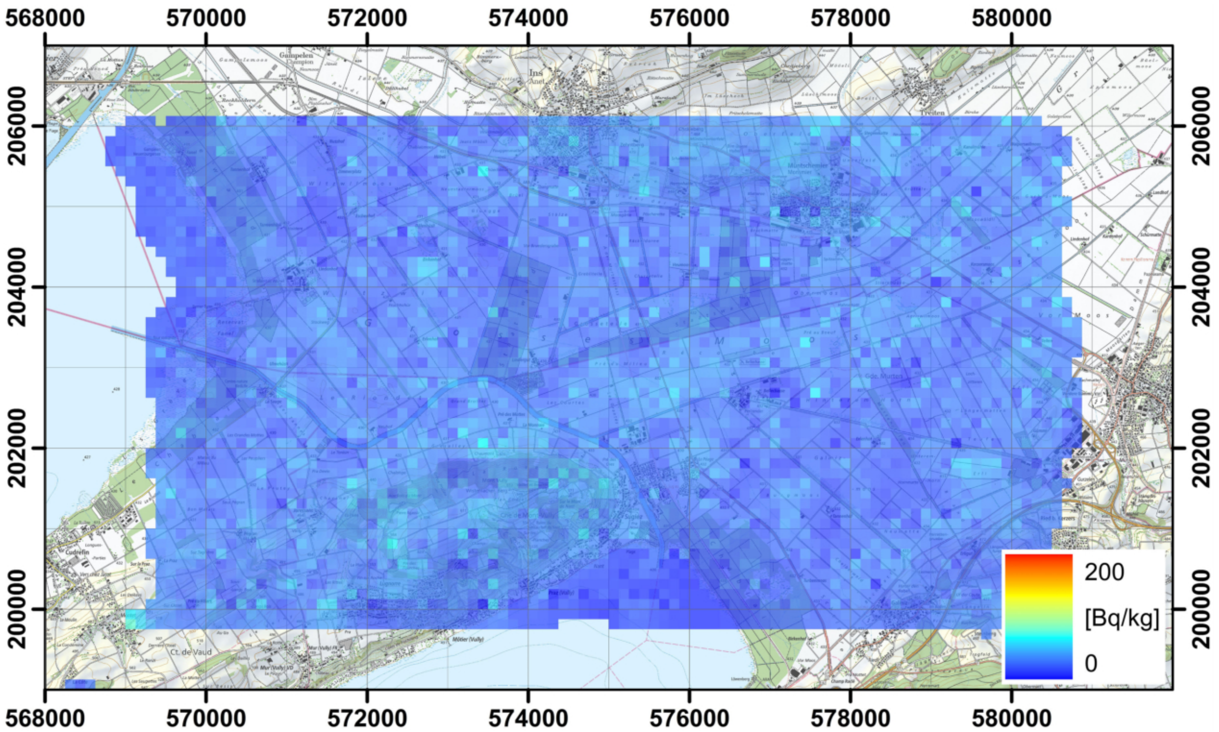

Figure 39: ^{238}U activity concentration in the vicinity of Mont Vully.
PK25 ©2018 swisstopo (JD100042).

2.5 Transversal from Berne to Kandersteg

During ARM18z, a transversal was measured ranging from Berne in the north to Kandersteg in the south. Figure 40 shows the flightline of the transversal. The altitude profile along the transversal, starting in the north, rises from 600 m to 1600 m above sea level (figure 41). The total dose rate along the transversal increases together with the flight altitude due an elevated contribution of cosmic radiation to the dose rate (figure 42). Removing the dose rate contribution of cosmic radiation from the total dose rate yields the terrestrial component of dose rate (figure 43). The terrestrial dose rate is produced by natural radionuclides in soil and rock, like for example ^{40}K (figure 44) and reflects their respective activity concentrations. The peak of the ^{40}K activity concentration at length of run 62.2 km (coordinates (618334, 151921)) is associated with a quarry near Kandergrund.
The photons emitted from the natural radionuclides are attenuated if they have to pass through layers of water. Thus, lower values of dose rates and activity concentrations are observed when the flight line crosses water bodies like the Aare River.

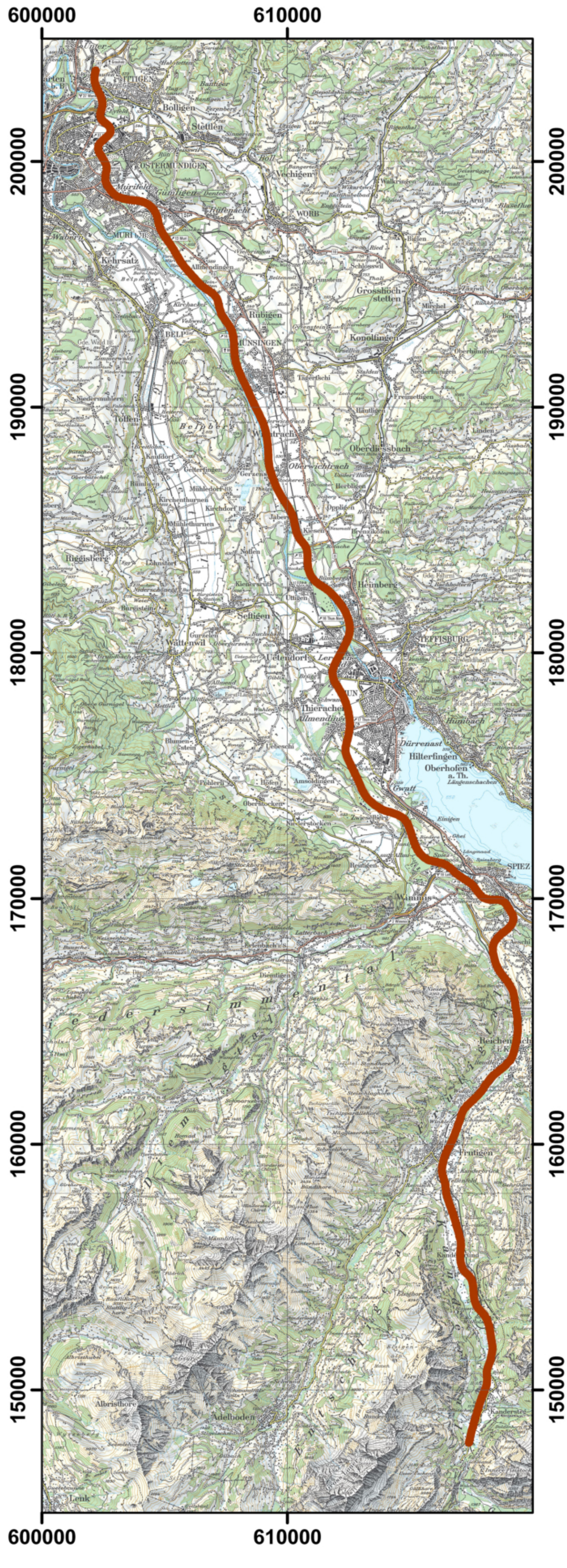

Figure 40: Flight line of the transversal form Berne to Kandersteg
PK100 ©2018 swisstopo (JD100042).

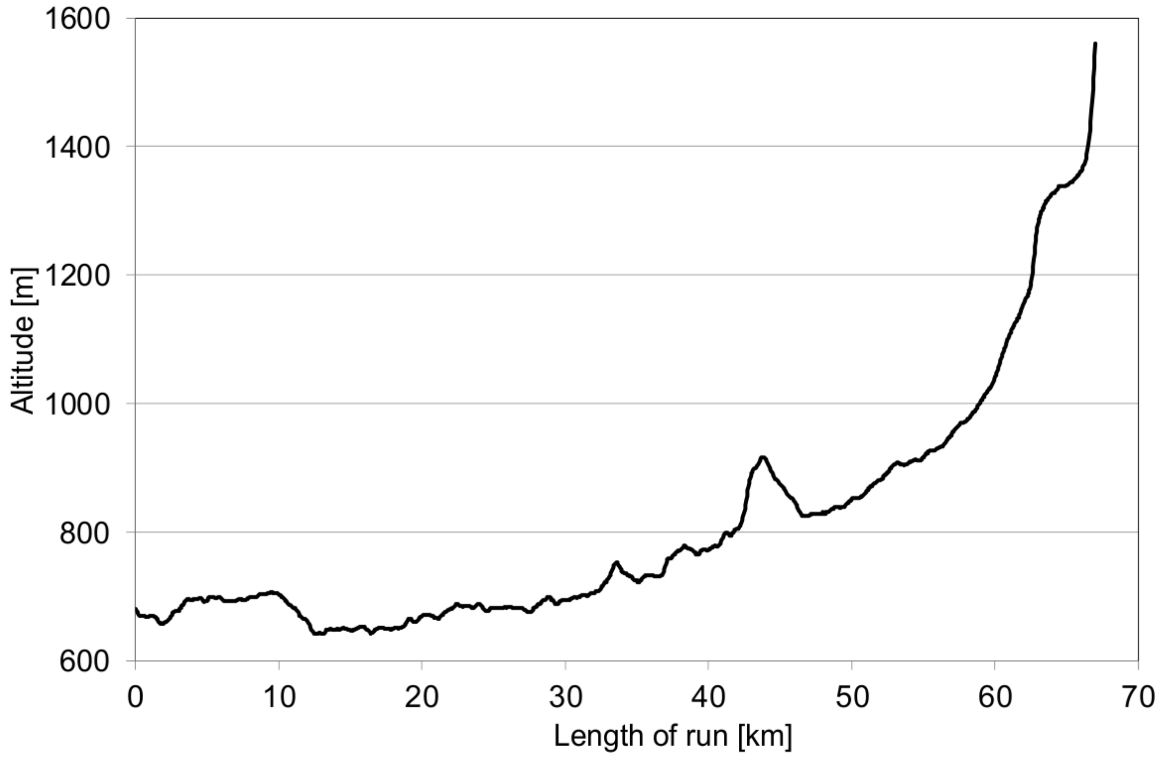

Figure 41: Altitude profile of the transversal from Berne to Kandersteg.

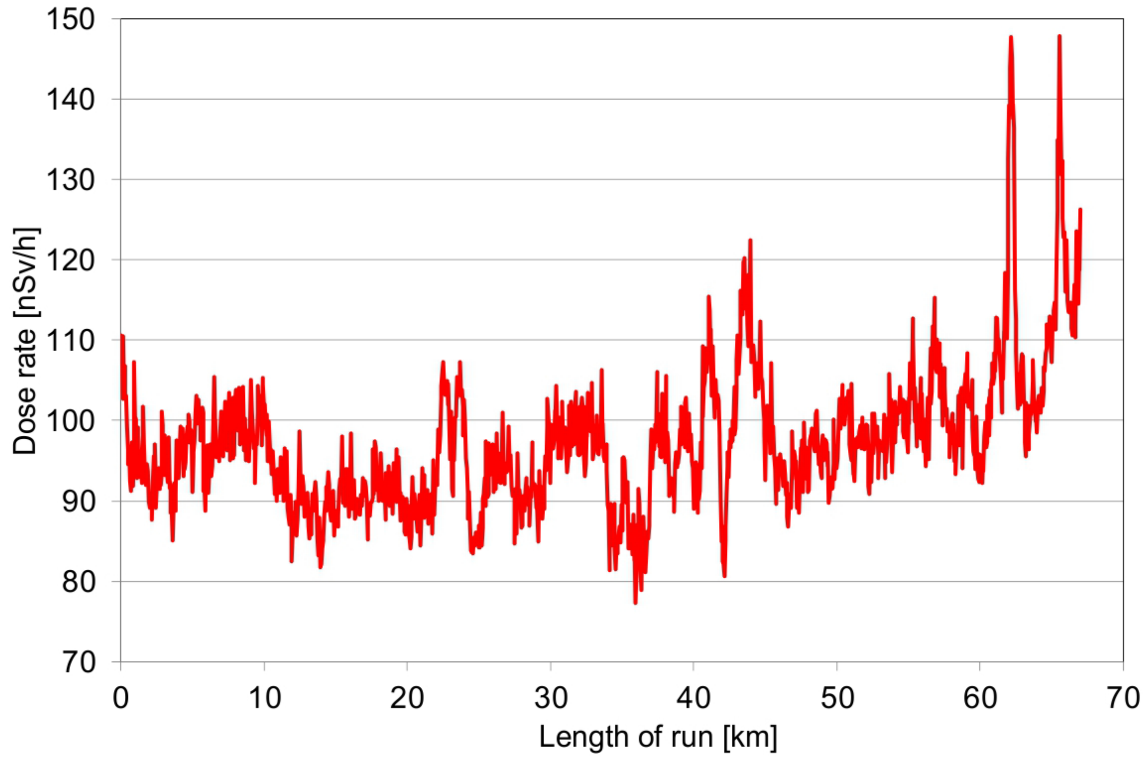

Figure 42: Dose rate along the transversal from Berne to Kandersteg.

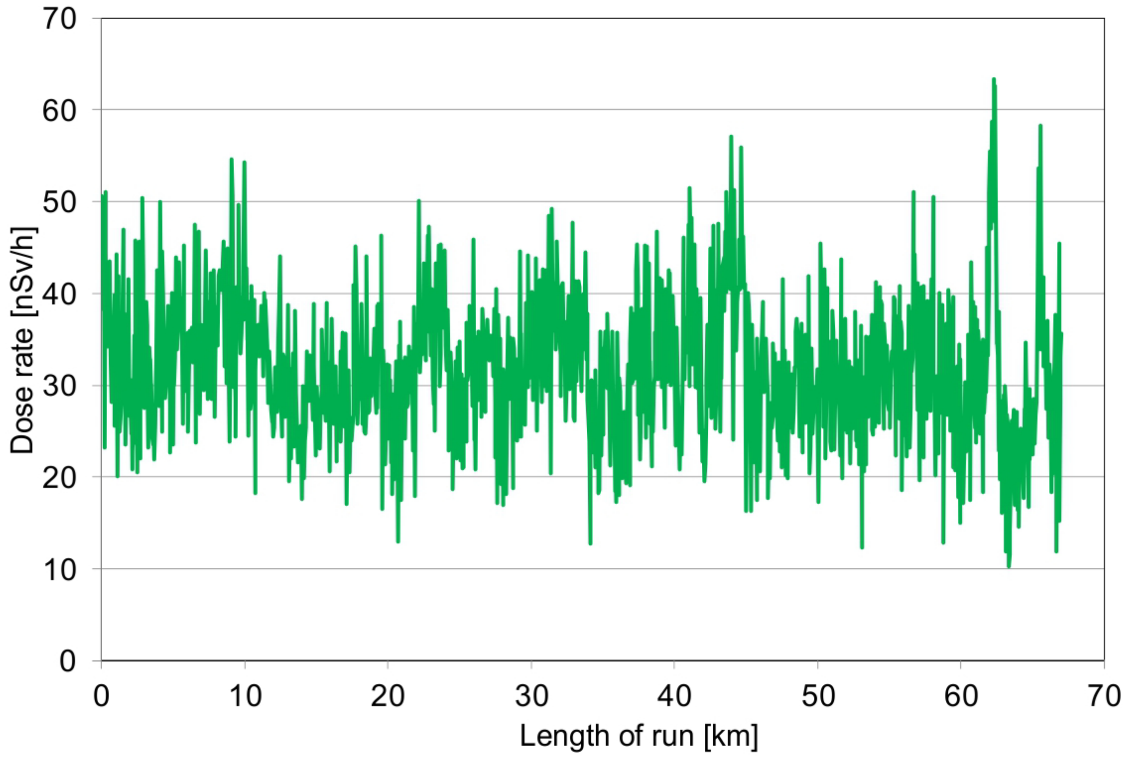

Figure 43: Terrestrial component of the dose rate along the transversal from Berne to Kandersteg.

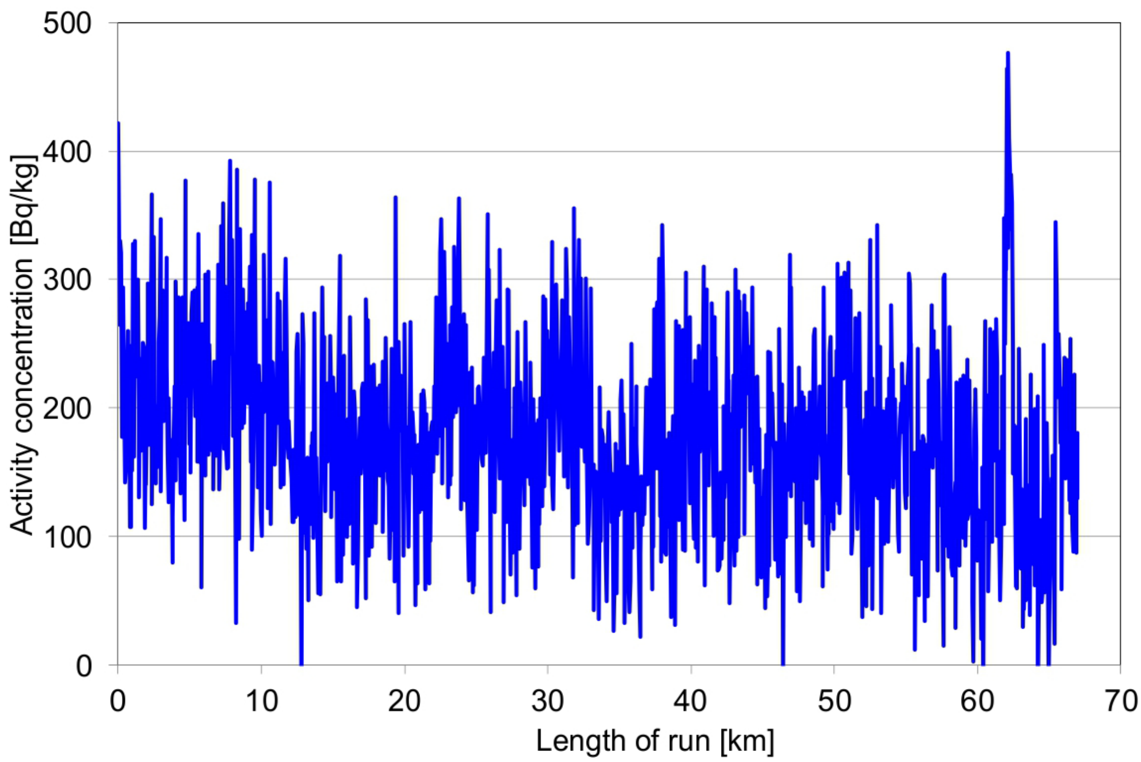

Figure 44: ^{40}K activity concentration along the transversal from Berne to Kandersteg.

2.6 Exercise CONTEX 2018

The Danish field exercise CONTEX (Contamination Exercise) 2018 was conducted by the Danish Emergency Management Agency (DEMA) in western Denmark on June 19th to 21st, 2018. The CONTEX 2018 exercise was based on a plume contamination scenario and took place in a military exercise area called Finderup just west of the city of Viborg. The exercise was directed towards field radiation measurements and cooperation between expert teams in an international context. The exercise was conducted in the framework of IAEA RANET (Response and Assistance Network) guidelines as well as the latest draft of IAEA "Guidelines for response and assistance products during a nuclear or radiological emergency".
Participants in the exercise were the DEMA Emergency Centres, the Danish Joint Military CBRN Company, the German Federal Office for Radiation Protection, the Norwegian Radiation Protection Authority, the Icelandic Radiation Safety Authority, the Swedish Radiation Safety Authority, the Finnish Radiation and Nuclear Safety Authority, Public Health England, the Austrian Agency for Health and Food Safety and the Swiss Federal Office for Civil Protection. The collaboration and coordination between Field Assistance Teams (FAT) from all the countries was the focal point of the exercise.
As the exercise area was located close to the North Sea, the Swiss team took the opportunity to measure an altitude profile offshore during a period with land-bound wind. Thus, the influence of airborne radon progeny on the measured spectra can be considered minimal.
The location of the exercise area and an altitude profile over the North Sea are shown in figure 45.

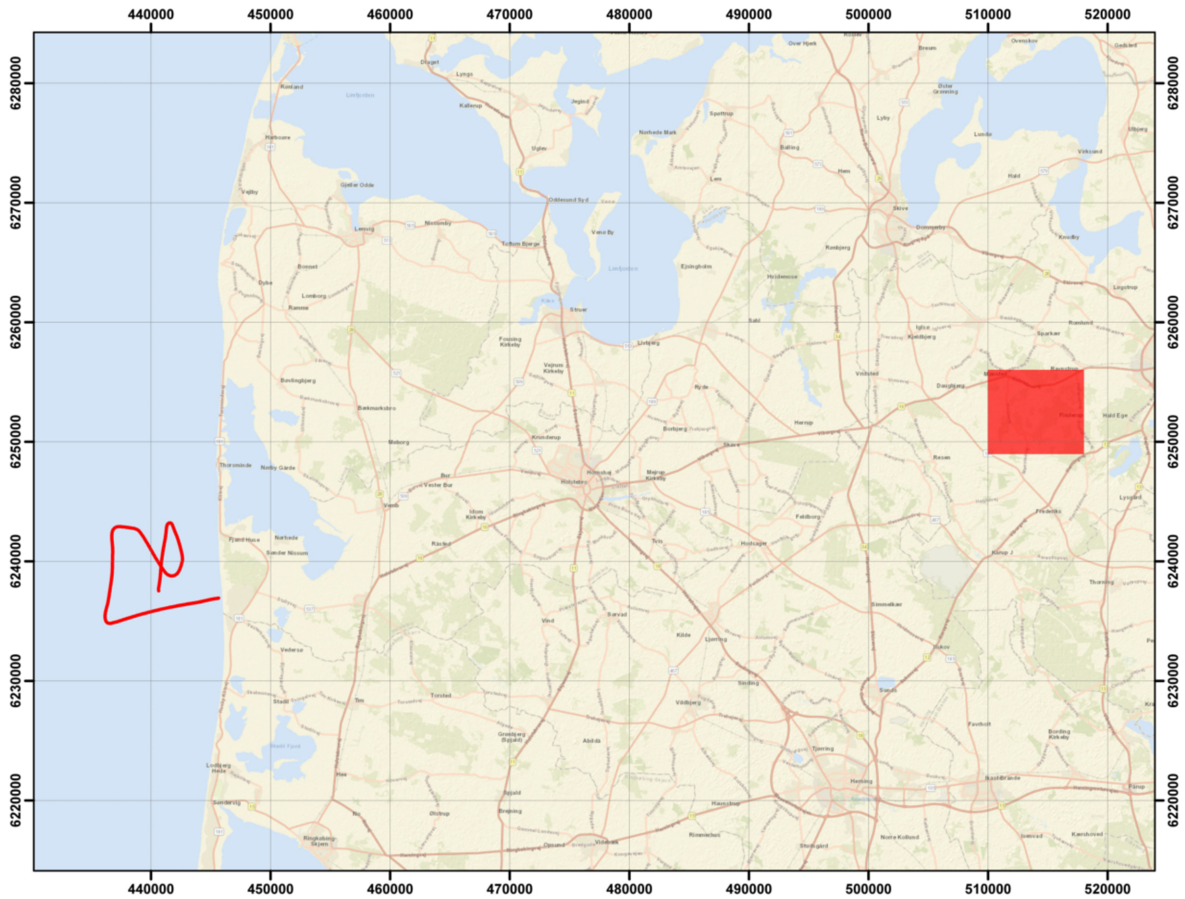

Figure 45: Location of the Contex 2018 exercise area (red rectangle) and the altitude profile (red line). World street map ©2018 ESRI Inc.

2.6.1 Altitude profiles

The altitude profile over the North Sea is compared to two altitude profiles measured over Swiss lakes in 2017 (Lake Zug) and 2018 (Lake Geneva) with the identical detector. Figure 46 depicts the count rate in the cosmic window between 2.9 MeV and 3.5 MeV in dependence on flight altitude for all data points measured along the altitude profiles, showing identical behaviour for all three locations. The maximum flight altitude over the North Sea was limited by the Danish air traffic control.
The count rate in the cosmic window is used for cosmic and background corrections in the other energy windows, assuming a linear dependence of the count rate in the individual energy window to the cosmic count rate. Figure 47 shows clear differences between the different flight locations. As the detector for all three altitude profiles was identical, the count rate differences would be attributed to changes in the helicopter background radiation. However, the magnitude of the difference of a factor of two between the altitude profile over the North Sea and the altitude profile over Lake Geneva makes this interpretation unlikely. An alternative interpretation would be the assumption of additional counts from airborne radon progeny. Under this assumption, a larger effect could be expected at low photon energies, as the radon decay product ^{214}Pb emits mainly photons below 352 keV. Thus, a low energy window between 100 keV and 400 keV was introduced to test this assumption. Figure 48 shows indeed an even clearer separation of the different altitude profiles. The count rates in the low energy window are higher compared to the total energy windows from 400 keV to 3000 keV.
In a next step, the altitude profile over the North Sea was assumed to be not influenced by radon progeny. Thus, the derived stripping correction for system background and cosmic contribution (table 3) can be considered as applicable for all flights. The residual counts remaining in the different energy windows after application of this stripping correction for the altitude profiles over the inland lakes are assumed to be associated with airborne radon progeny. For a separation of counts from airborne radon progeny and radon progeny in the ground, the method suggested by Minty et al. (1997) was adapted. The residual counts after the initial cosmic and background stripping are correlated to the ratio of the count rates in the low energy window (100 keV to 400 keV) and a high energy (MMGC2) window (1400 keV to 3000 keV), denominated as “Rn-ratio”. The residual counts in the total energy window are depicted as red crosses in figure 49 as function of the Rn-ratio. The error bars drawn for the three data points representing the three altitude profiles (average Rn-ratios: North Sea 6.9, Lake Zug 7.1, Lake Geneva 8.5) represent the twice the standard deviation of the average.
A simple square root model

$$CR_{Rn} = F_{Rn}\sqrt{R_{Rn} - R_{Rn,0}}$$

with:

CR_{Rn}:	Additional count rate due to airborne radon progeny [cps]
F_{Rn}:	Factor correlating the Rn-ratio to the additional count rate [cps]
R_{Rn}:	Rn-ratio [ ]
$R_{Rn,0}$:	Baseline Rn-ratio without airborne radon progeny [ ]

can be used to fit the data for the total and all other energy windows (figures 50, 51, 52 and 53) with the exception of the thorium energy window. In the energy range of the thorium window between 2407 keV and 2797 keV radon progeny has less than one percent photon emission probability. Thus, this window is nearly uninfluenced by airborne radon progeny and statistical fluctuations obscure the potential small dependence on the Rn-ratio. Table 4 lists the radon progeny correlation factors derived from the three altitude profiles for the different energy windows. In this early phase of development, an estimate of uncertainties would be premature. In a next step, the presented prediction of additional counts due to radon progeny has to be tested with additional altitude profiles over inland lakes.

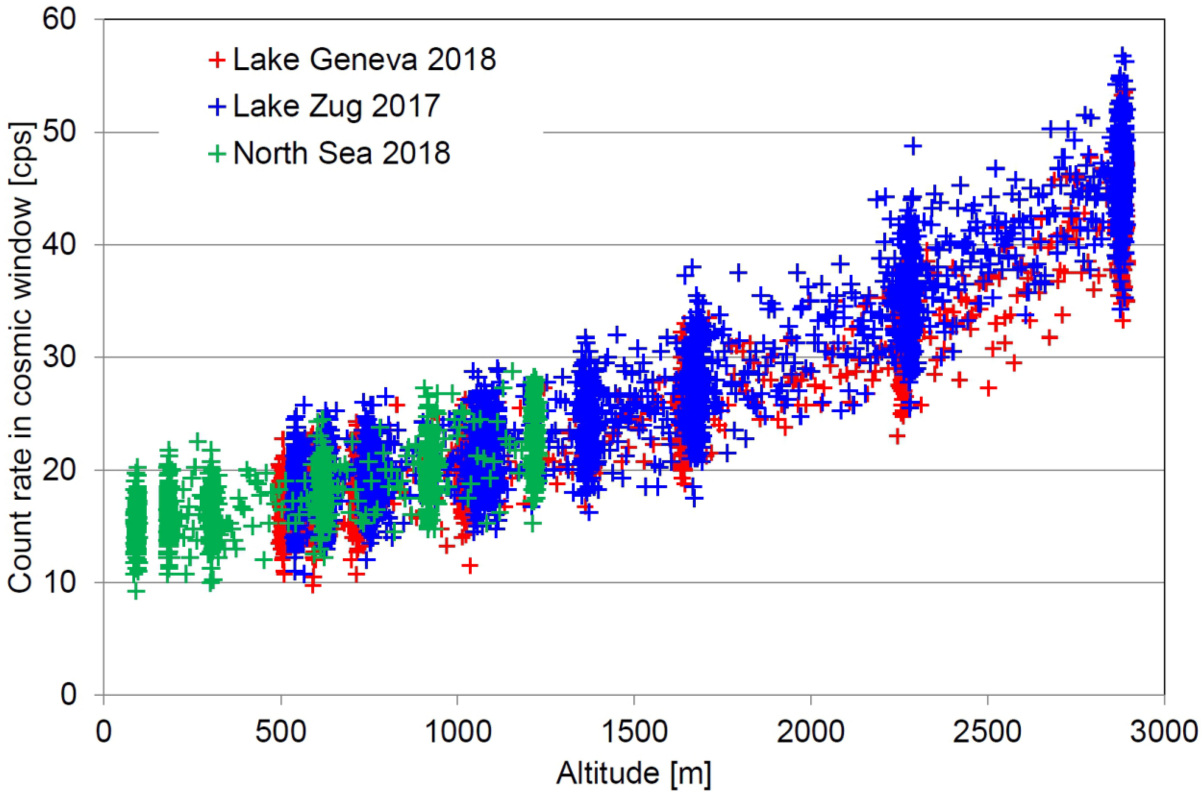

Figure 46: Count rate in the cosmic window in dependence on flight altitude.

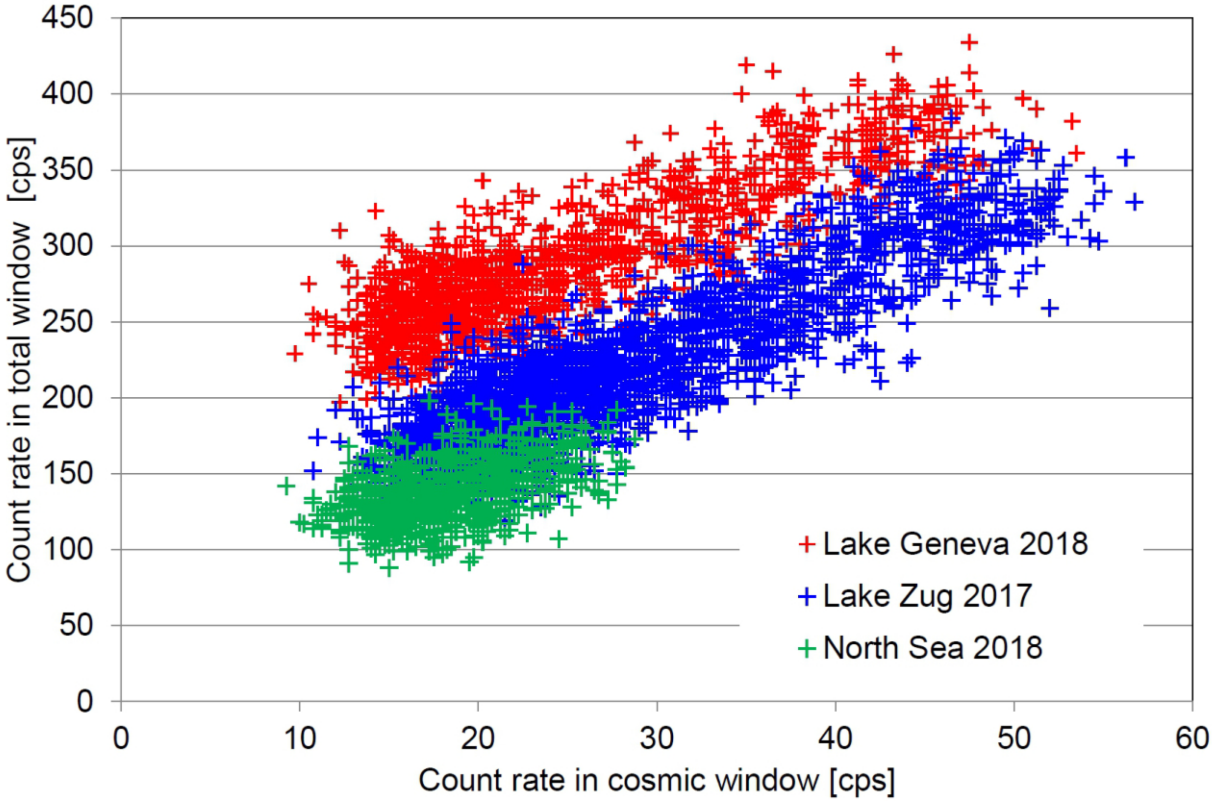

Figure 47: Count rate in the total energy window in dependence on the cosmic count rate.

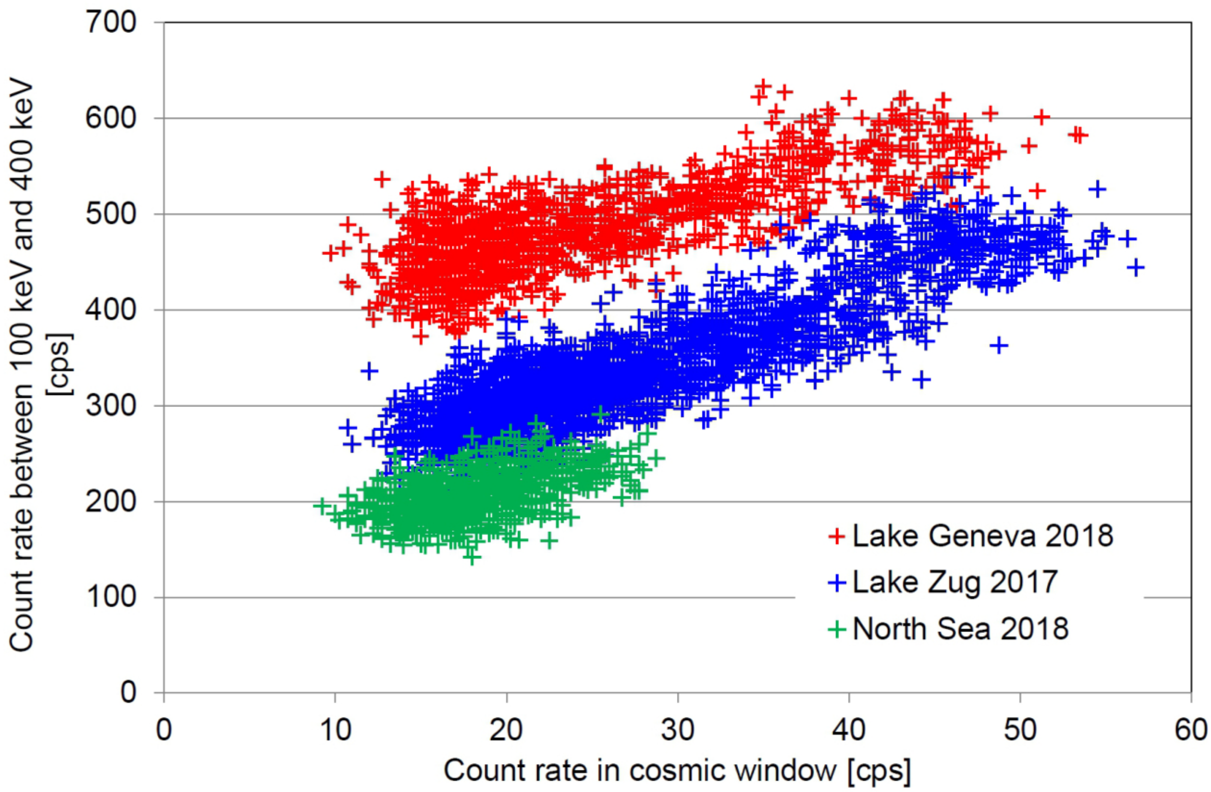

Figure 48: Count rate in the low energy window in dependence on the cosmic count rate.

Energy window	S_c	$U(S_c)$	CR_B [cps]	$U(CR_B)$ [cps]
Total	2.73	0.15	88	3
Potassium	0.06	0.03	9	0.6
Uranium	0.15	0.02	2	0.4
Thorium	0.17	0.03	2	0.5
Caesium	0.21	0.04	12	1
Cobalt	0.19	0.04	11	1
MMGC1	1.84	0.12	73	2
MMGC2	0.88	0.07	16	1
Low	3.55	0.18	143	3

Table 3: Parameters of cosmic and background stripping corrections derived from the altitude profile over the North Sea. S_c: Slope, CR_B: Background count rate, $U(S_c)$, $U(CR_B)$: Respective uncertainties.

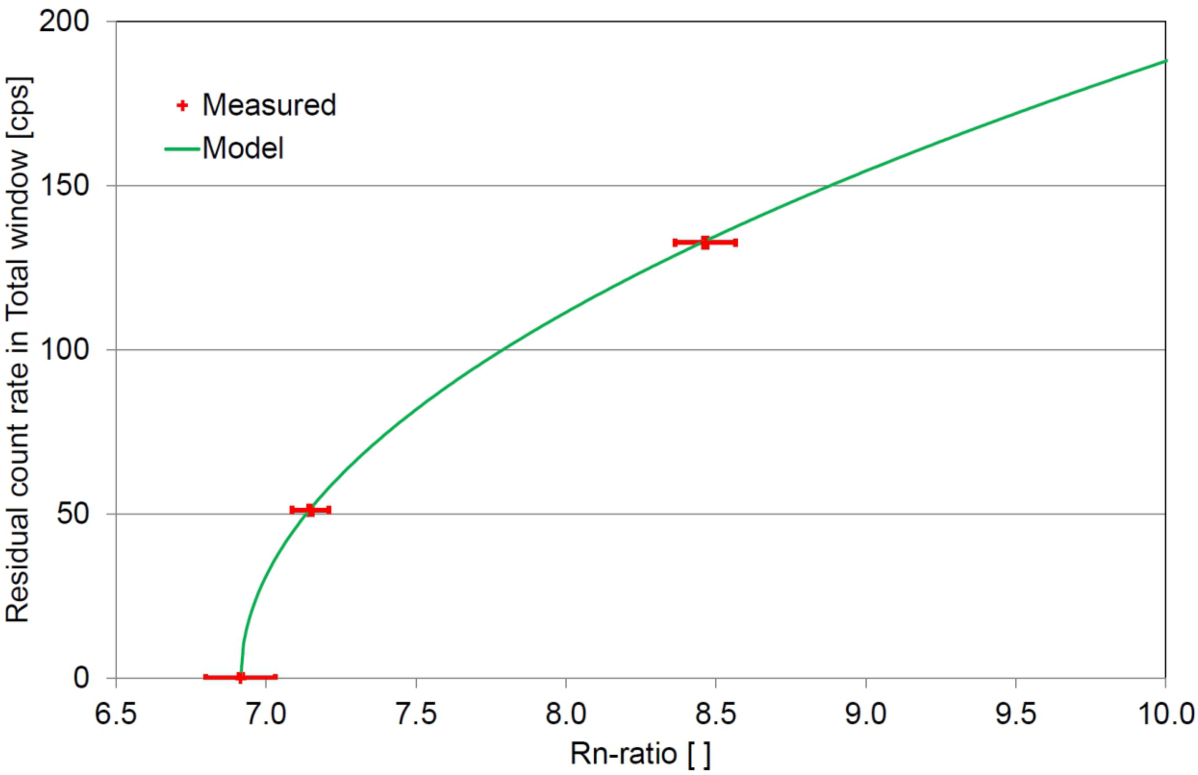

Figure 49: Residual count rate in the total window in dependence on the Rn-ratio.

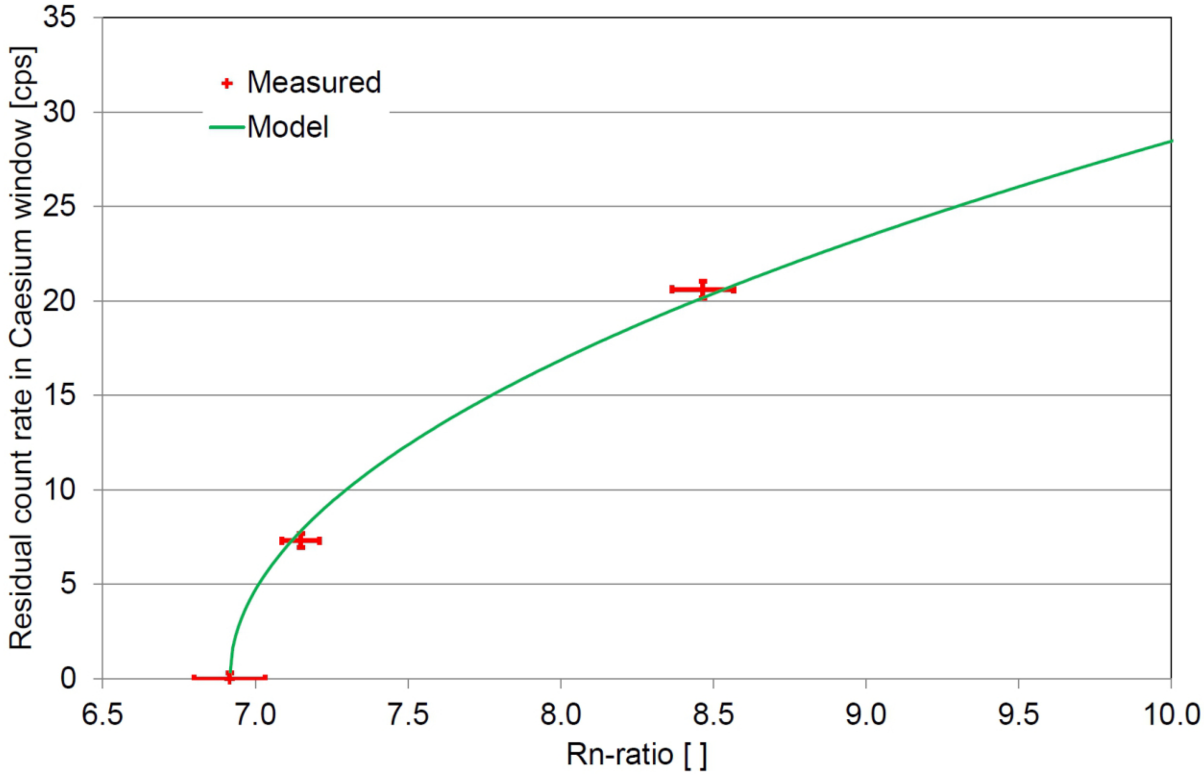

Figure 50: Residual count rate in the caesium window in dependence on the Rn-ratio.

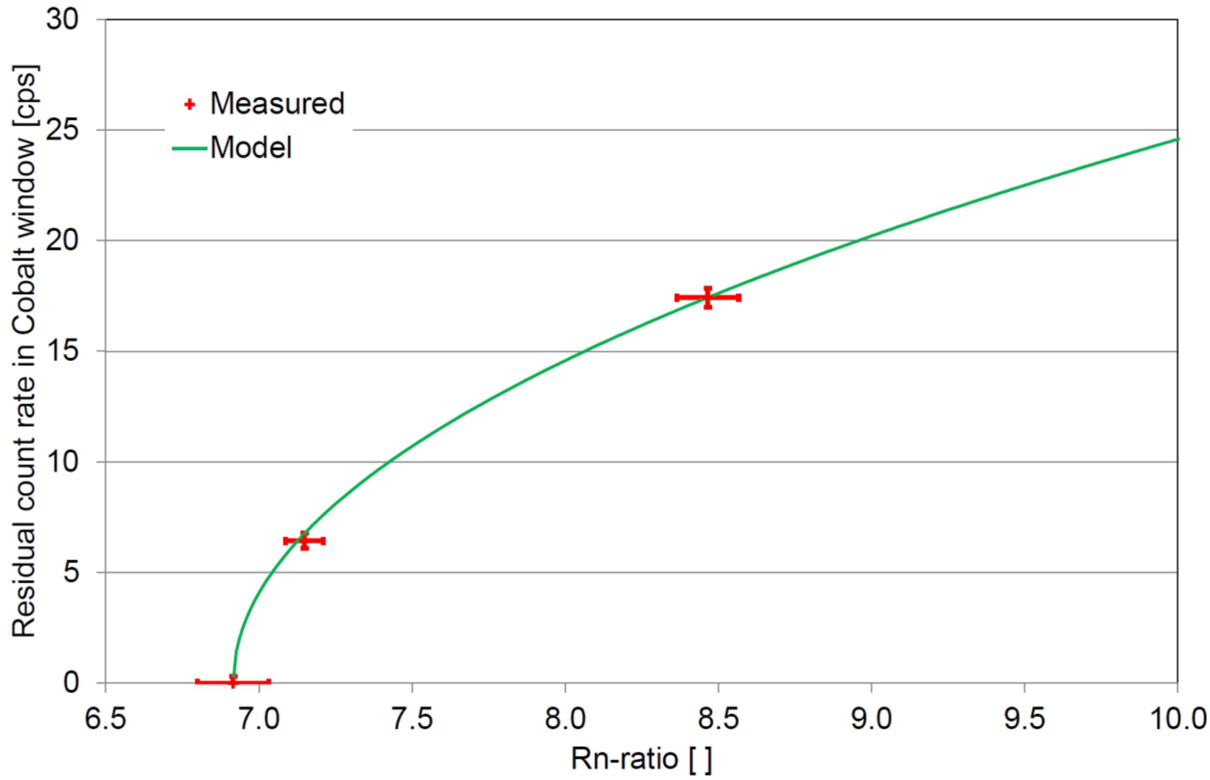

Figure 51: Residual count rate in the cobalt window in dependence on the Rn-ratio.

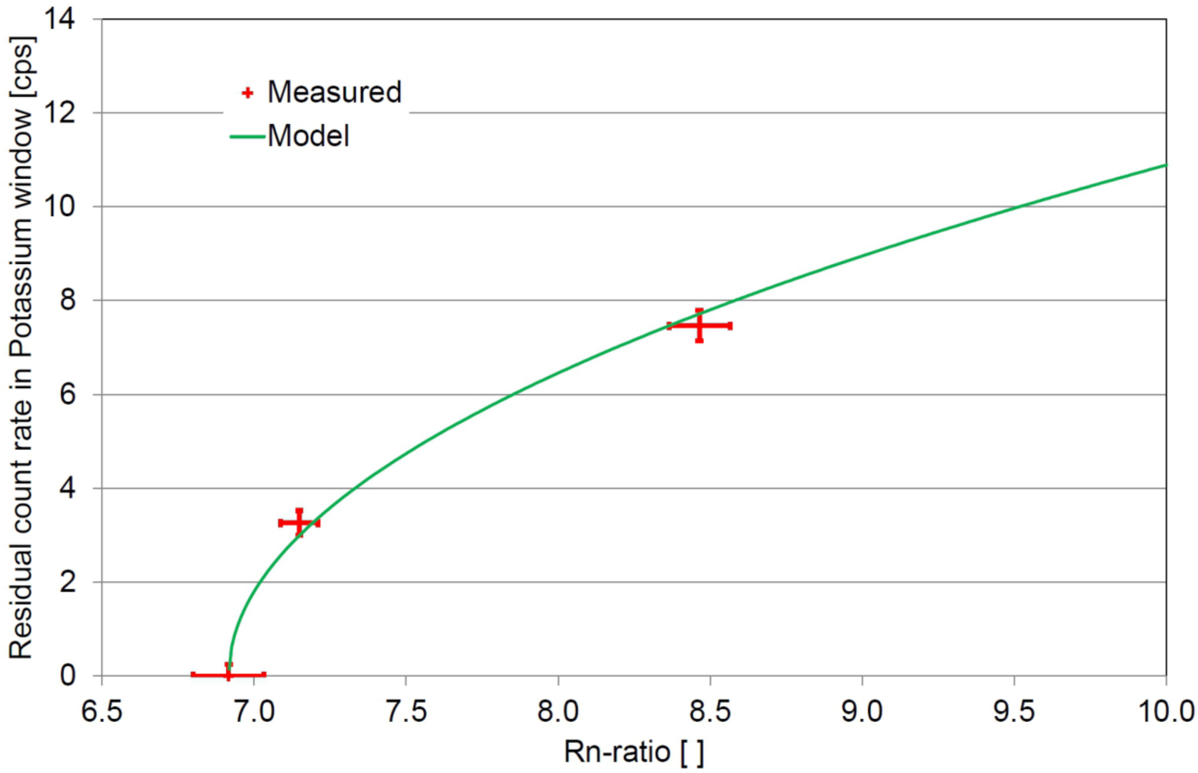

Figure 52: Residual count rate in the potassium window in dependence on the Rn-ratio.

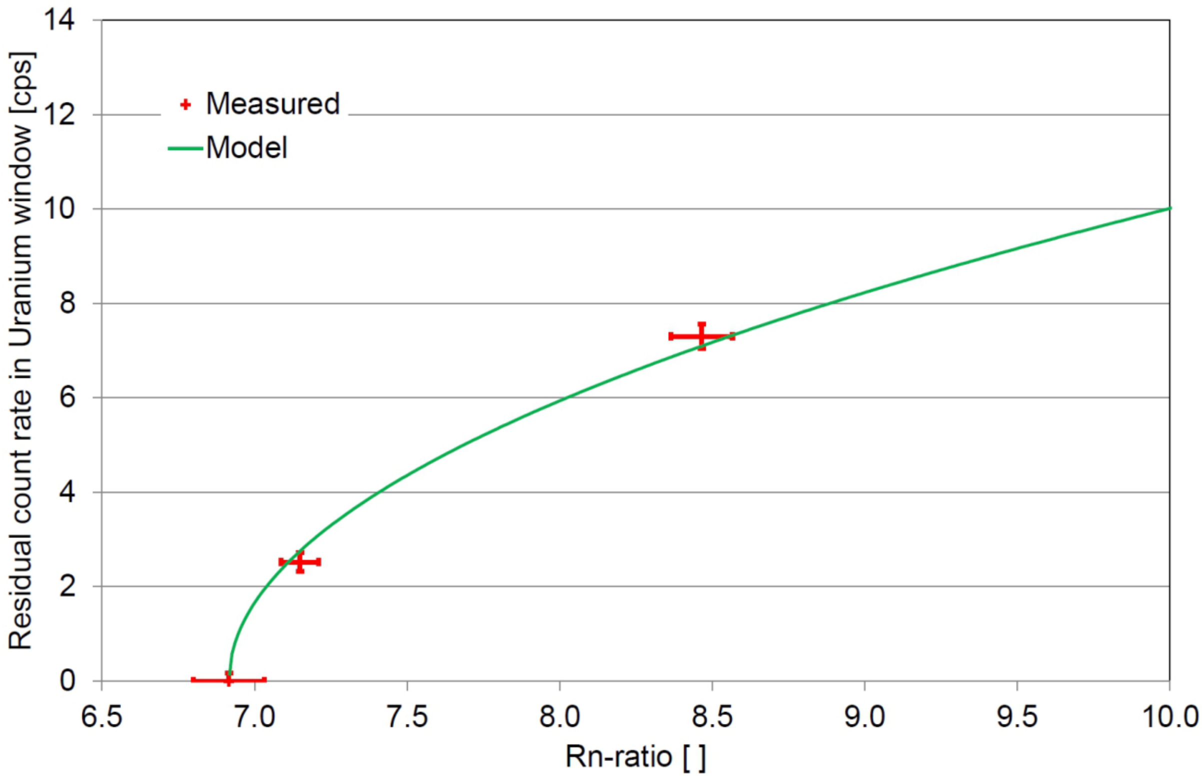

Figure 53: Residual count rate in the uranium window in dependence on the Rn-ratio.

Energy window	F_{Rn} [cps]
Total	107
Potassium	6.2
Uranium	5.7
Thorium	-
Caesium	16
Cobalt	14
MMGC1	86
MMGC2	19

Table 4: Radon correlation factor derived from three altitude profiles.

2.6.2 Exercise area

For each day of the exercise Contex 2018, the exercise area was inspected with airborne gamma-spectrometry. The configuration of radioactive sources was changed for each day of the exercise by the organisers.
As multiple sources could be expected in the exercise area, a procedure was tested to separate different sources. The spectra for all data points within the field of view of airborne gamma spectrometry (125 m) at ground clearance of 100 m around the maximum MMGC-ratio (named MMGC-maximum 1 in the further text) were averaged and analysed. This procedure was repeated with the remaining data points (MMGC-maximum 2, 3, ..., 20) .
The maps of dose rate (figure 54) and man-made gross count (MMGC) ratio (figure 55) show for June 19th a single area with elevated readings. The distribution of the twenty largest MMGC-maxima with distances larger than the averaging area with a diameter of 125 m around each maximum is shown in figure 56. The spectra of the first three MMGC-maxima are depicted in comparison to a background spectrum in figure 57. The background spectrum was calculated as average over all measuring points with at least 1 km distance to the location of any of the 20 MMGC-maxima. The photon background is produced by natural radionulides in soil and rock. As an example, the photon peak of ^{40}K at 1460 keV is marked in figure 57.
The average spectrum of the first MMGC-maximum at UTM coordinates (514825, 6253495) (marked in figure 55) shows clearly a photo peak which can be associated with the photon emission of ^{137}Cs at 662 keV. The associated value of the MMGC-ratio of 15.5 is well above the background average value of 4.3. The location of the second MMGC-maximum with a MMGC-ratio of 7.0 at UTM coordinates (514698, 6253514) is just outside (128 m distance) of the averaging circle of 125 m around MMGC-maximum 1. The spectrum at this location shows still a slight peak of ^{137}Cs, originating from the source indicated at MMGC-maximum 1. In contrast, the average spectrum associated with MMGC-maximum 3 at coordinates (514877, 6253782) with a MMGC-ratio of 6.9 has a lower overall count rate than the background average. This measuring point is located over a small lake in the exercise area. Due to attenuation of photons from the natural radionuclides in the water layer, the count rate is decreased leading to artefacts in the MMGC-ratio. Analysis of the average spectra associated with MMGC-maxima 4 to 20 did not give an indication of the presence of further radioactive sources in the exercise area.

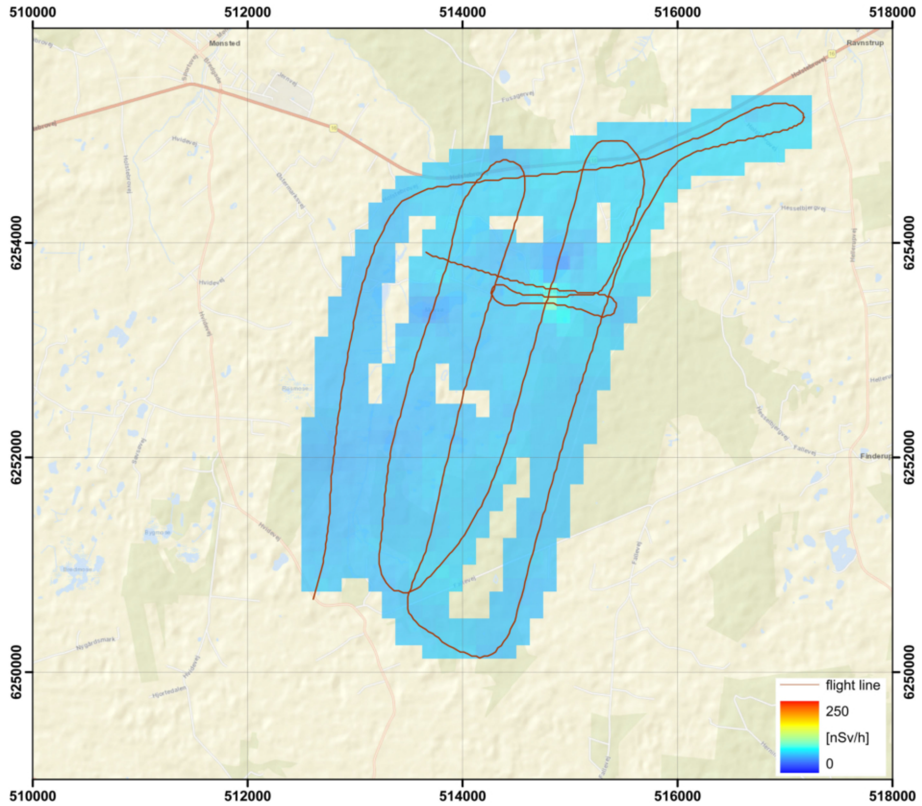

Figure 54: Dose rate over the Contex 2018 exercise area on June 19th. World street map ©2018 ESRI Inc.

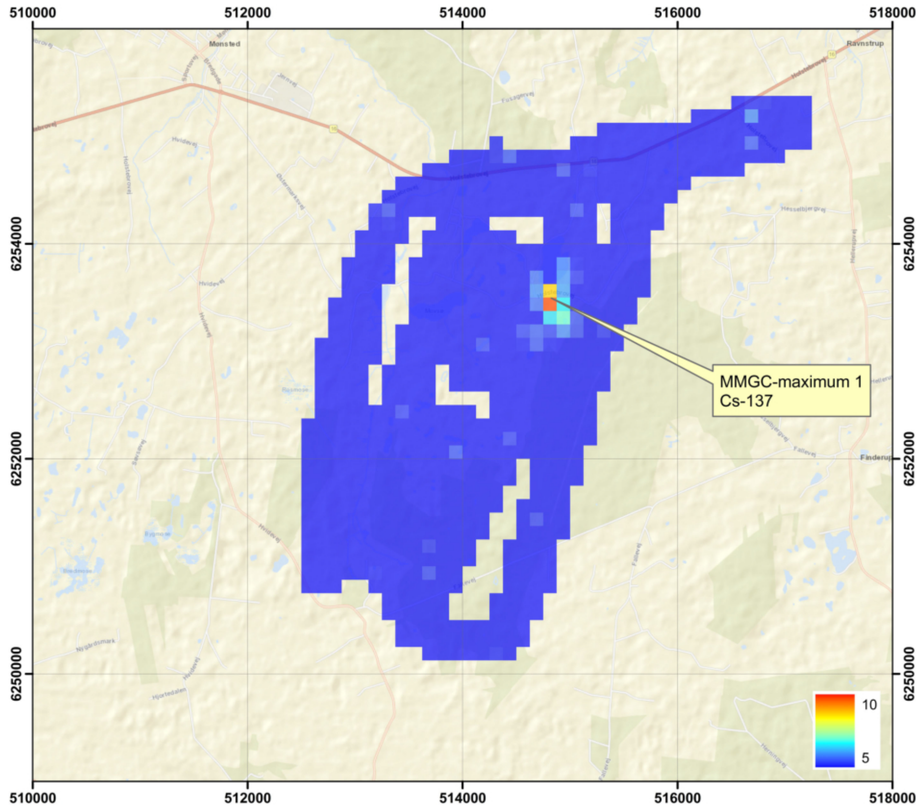

Figure 55: Man-made gross counts (MMGC) - ratio over the Contex 2018 exercise area on June 19th. World street map ©2018 ESRI Inc.

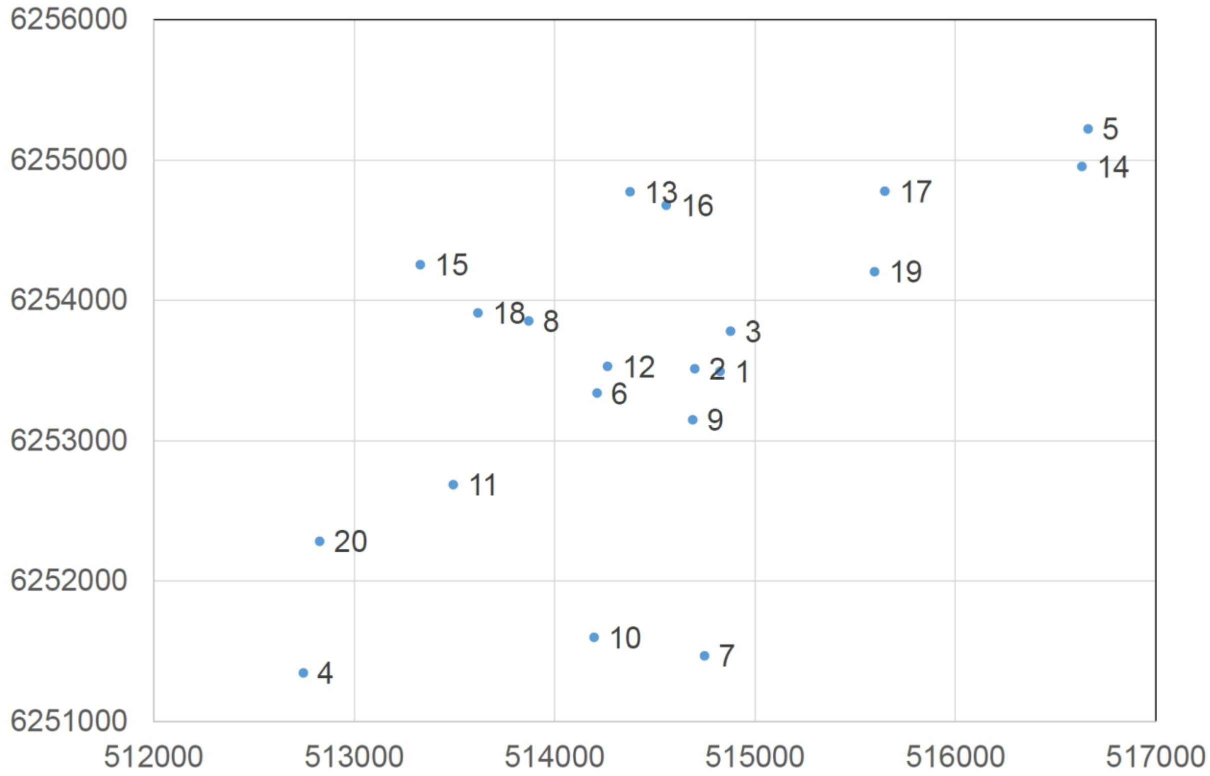

Figure 56: Location of the twenty largest MMGC values with distances larger than 125 m measured at June 19th (UTM32 coordinates).

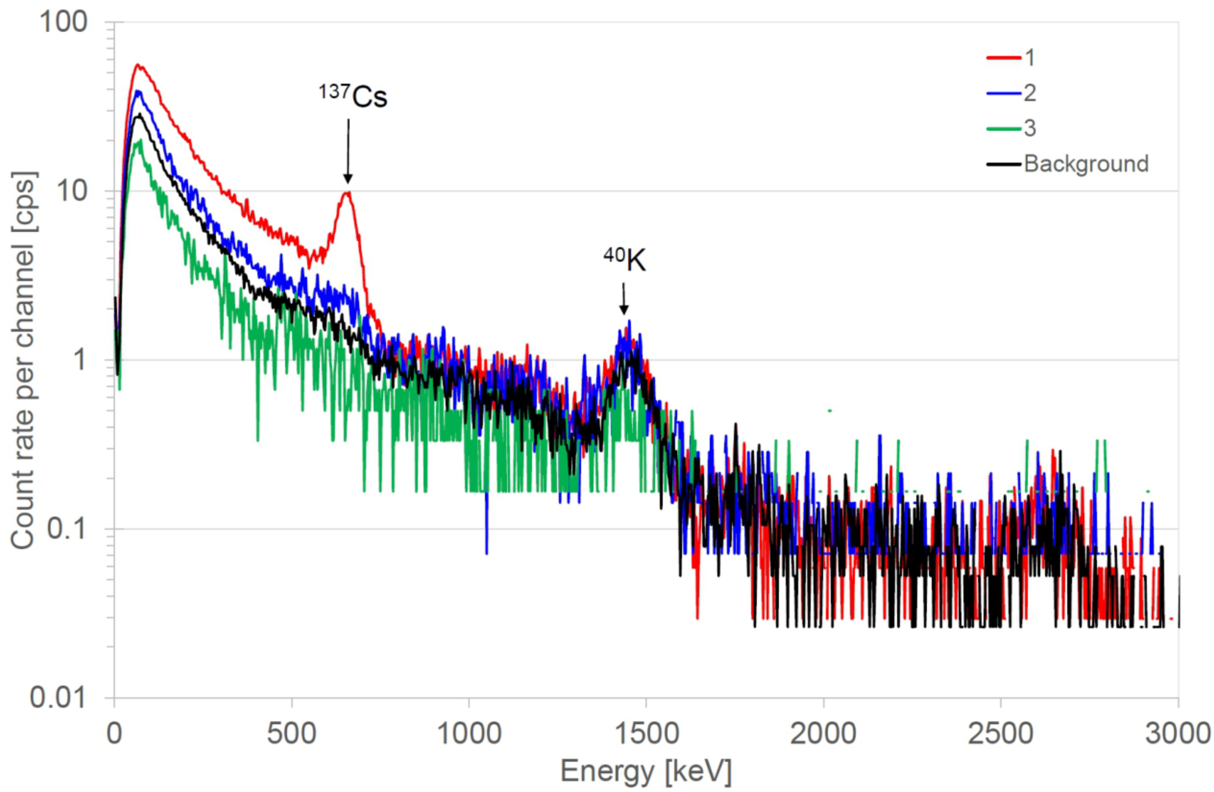

Figure 57: Average spectra over the three largest MMGC-maxima measured on June 19th compared to a background spectrum.

For the second day of the exercise (June 20th), maps of dose rate (figure 58) and man-made gross count (MMGC) ratio (figure 59) show several areas with elevated readings. Figure 60 shows the twenty largest MMGC-maxima derived with the procedure described above for June 20th. MMGC-maxima 3, 4 and 6 are clustered close to the first MMGC-maximum. The MMGC-ratio value of 1999 at the first MMGC-maximum located at coordinates (514772, 6253514) indicates a very strong artificial radionuclide source. The spectra of this cluster of MMGC-maxima (figure 61) identifies the radionuclide of the strong source as ^{192}Ir with three main groups of photon emissions around 310 keV, 470 keV and 610 keV. The spectra of MMGC-Maxima 3 and 4 can be associated with scattered radiation from the ^{192}Ir source, whereas MMGC-maximum 6 at UTM coordinates (514719, 6253648) additionally indicates the presence of a much weaker ^{137}Cs source.
MMGC-maximum 2 at UTM coordinates (514273, 6254029) clusters with MMGC-maxima 16 and 18. The plot of the respective spectra (figure 62) shows a clear indication of the presence of the radionuclide ^{137}Cs which is repeated less distinctly for MMGC-maximum 16 at UTM coordinates (514210, 6253914). The spectrum of MMGC-maximum 18 does not display photon peaks which could be associated with artificial radionuclides.
Figure 63 shows the spectra of the MMGC-maxima cluster consisting of MMGC-maxima 7 (UTM coordinate (516514, 6254820)), 8 and 10, identifying the radionuclides ^{99m}Tc with main photon emission at 141 keV and ^{137}Cs. These two radionuclides are also found in the MMGC-maxima cluster around MMGC-maximum 5 at UTM coordinates(514434, 6253475) (figure 64).
The spectra of MMGC-maxima 9, 11, 12, 15, 17, 19 and 20 were also inspected and displayed no indication of the presence of artificial radionuclides.
The locations of potential radioactive sources are marked in figure 59.

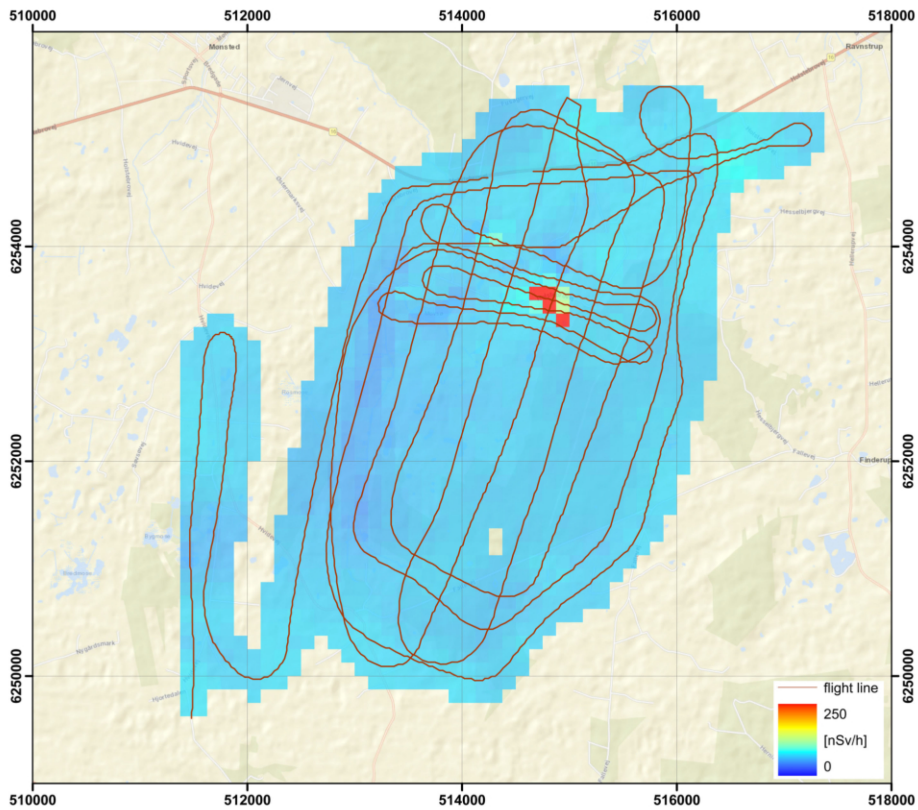

Figure 58: Dose rate over the Contex 2018 exercise area on June 20th. World street map ©2018 ESRI Inc.

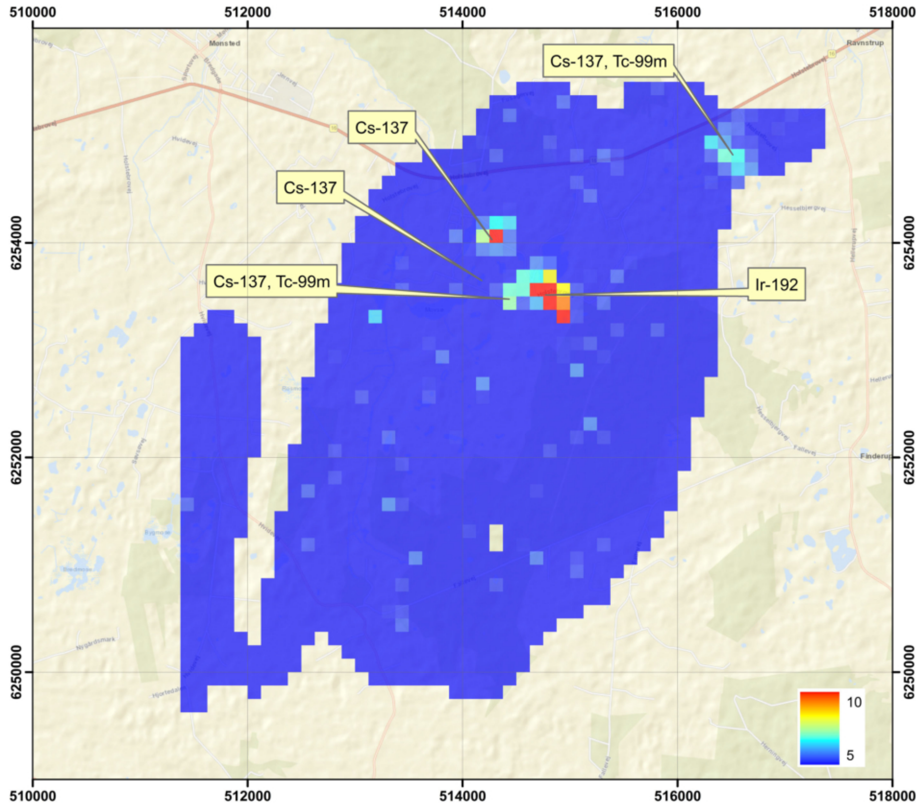

Figure 59: Man-made gross counts (MMGC) - ratio over the Contex 2018 exercise area on June 20th. World street map ©2018 ESRI Inc.

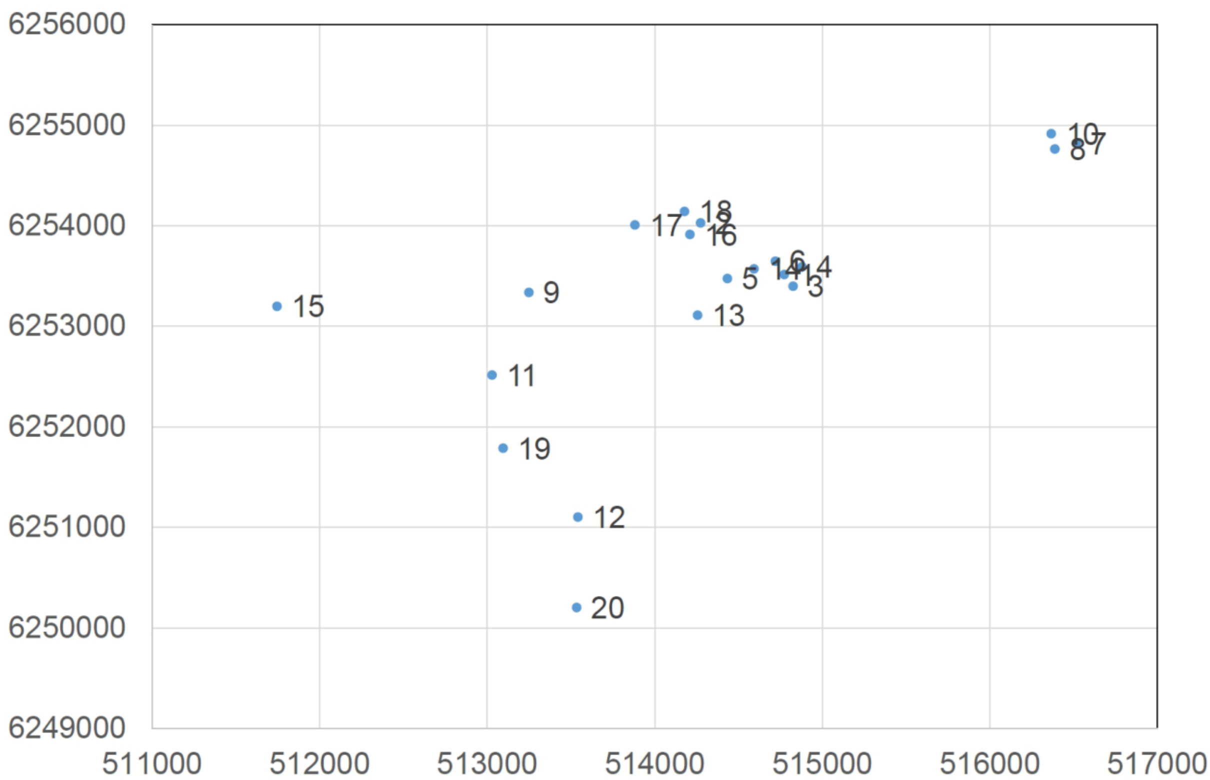

Figure 60: Location of the twenty largest MMGC values with distances larger than 125 m measured at June 20th (UTM32 coordinates).

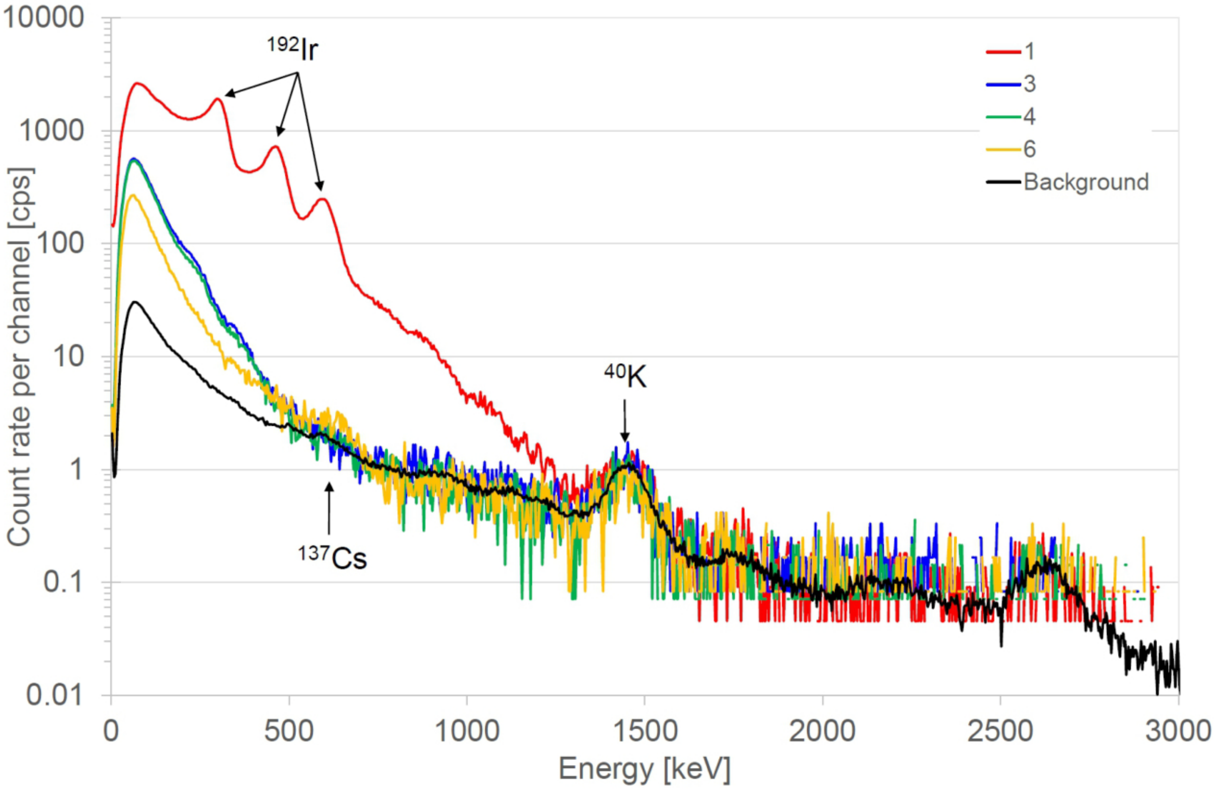

Figure 61: Average spectra over the MMGC-maxima No. 1, 3, 4 and 6 measured on June 20th compared to a background spectrum.

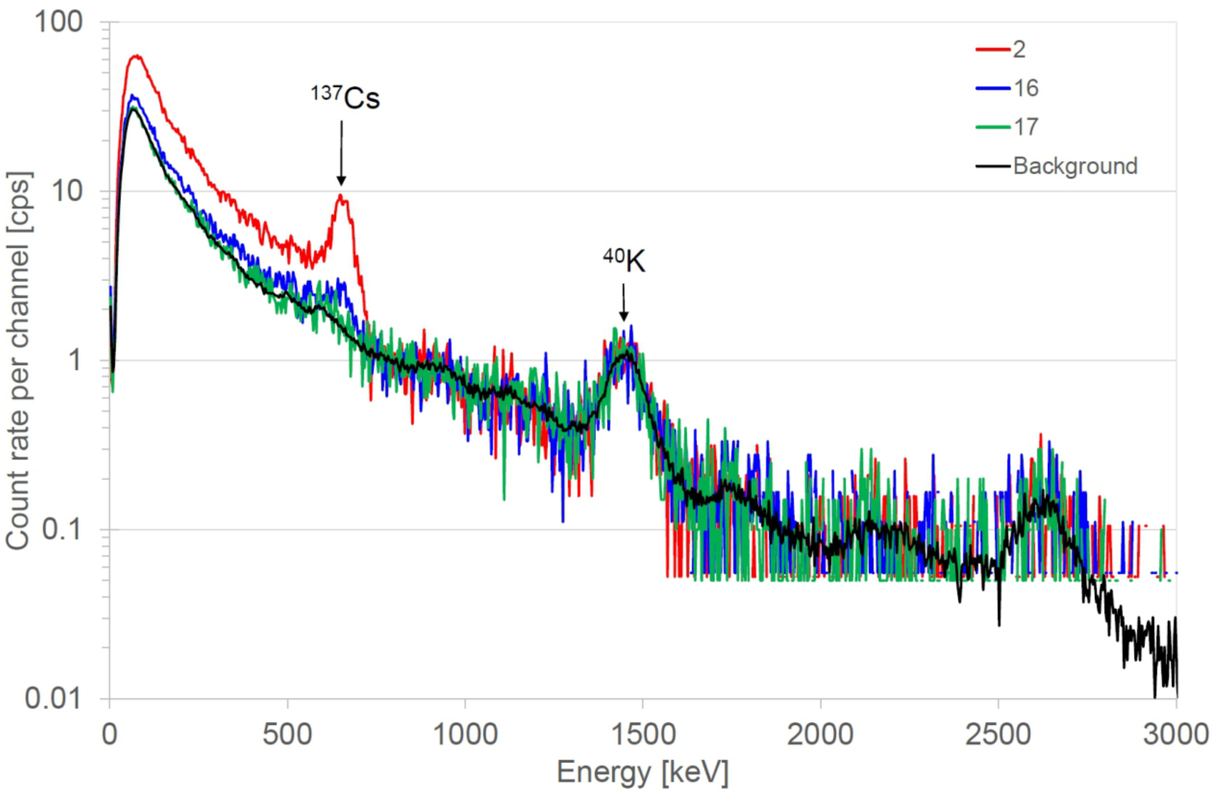

Figure 62: Average spectra over the MMGC-maxima No. 2, 16 and 18 measured on June 20th compared to a background spectrum.

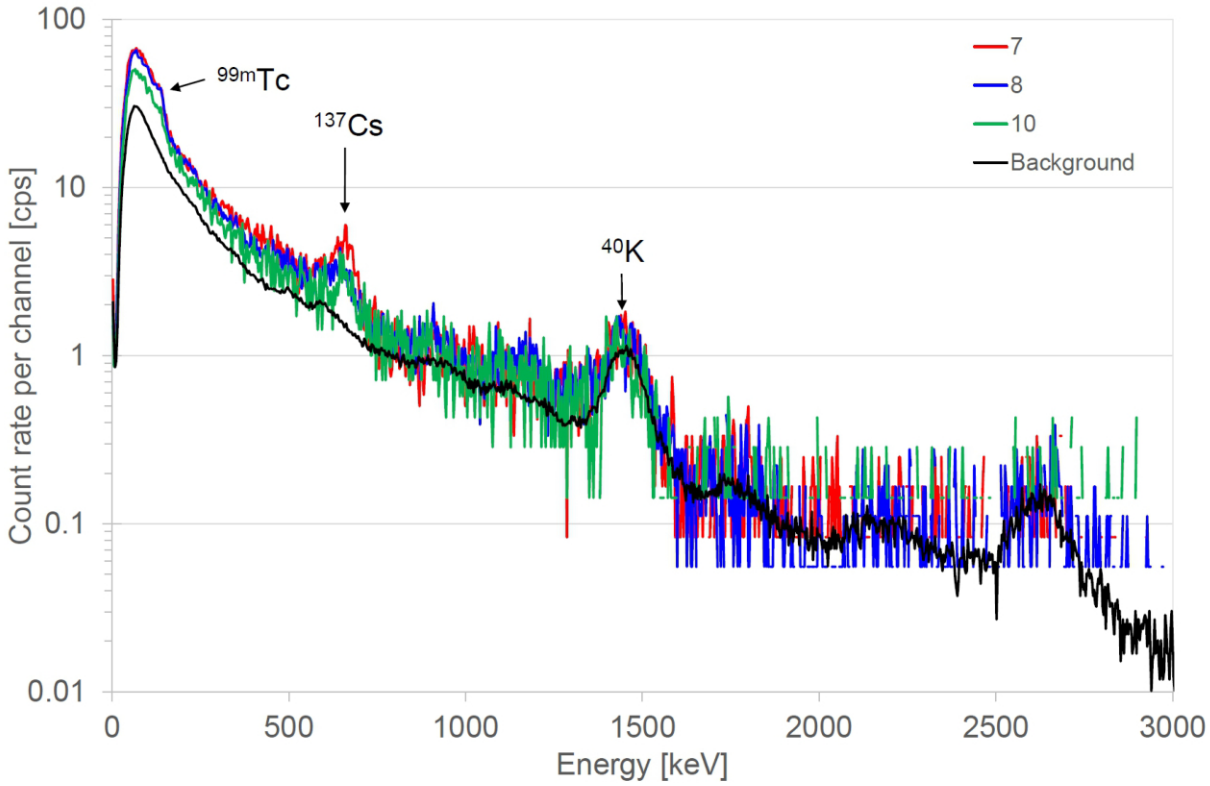

Figure 63: Average spectra over the MMGC-maxima No. 7, 8 and 10 measured on June 20th compared to a background spectrum.

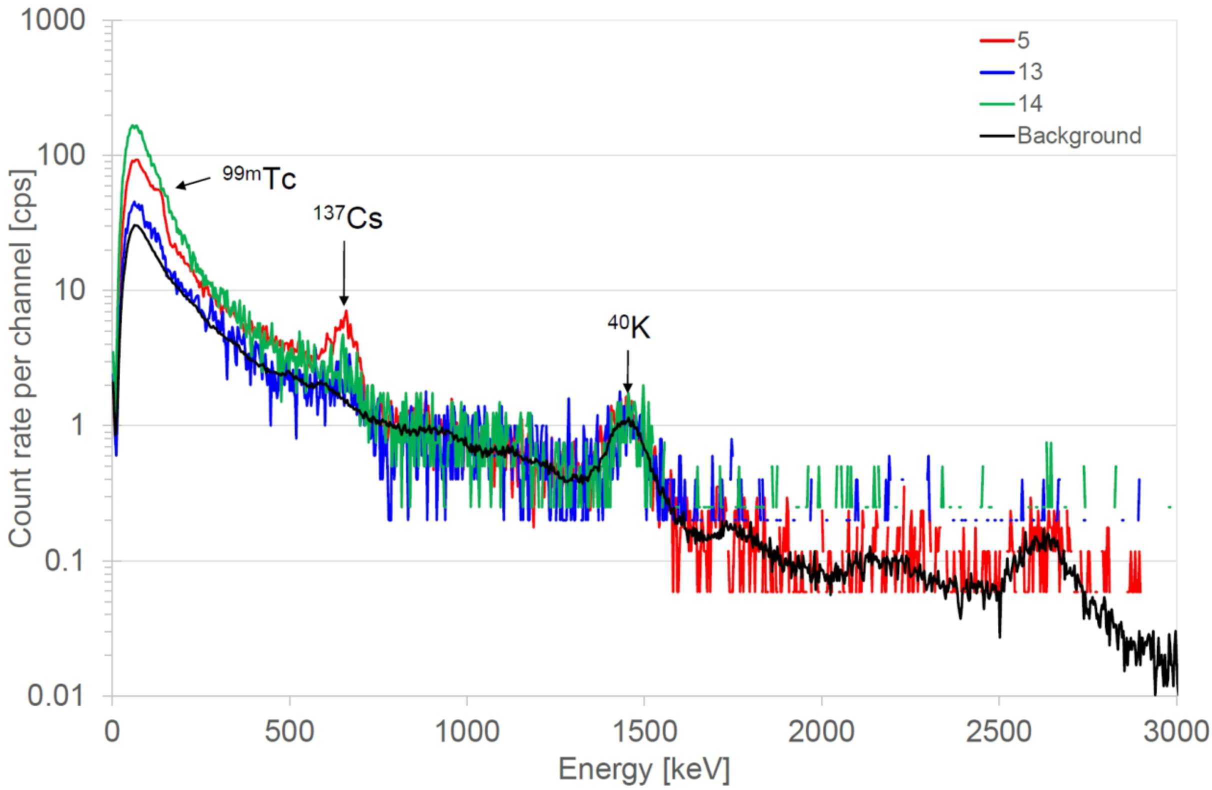

Figure 64: Average spectra over the MMGC-maxima No. 5, 13 and 14 measured on June 20th compared to a background spectrum.

For the third day of the exercise (June 21st), maps of dose rate (figure 65) and man-made gross count (MMGC) ratio (figure 66) show several areas with elevated readings. Figure 67 displays the twenty largest MMGC-maxima derived with the procedure described above for June 21st.

Figure 68 shows the spectra of the cluster of MMGC-maxima around the first MMGC-maximum. MMGC-maximum 1 located at UTM coordinates (514815, 6253515) with a MMGC-ratio of 2403 is identified as ^{192}Ir source, which was placed close to the location used on June 20th. MMGC-maxima 2, 3, 4, 7 and 20 can be associated with scattered radiation of the ^{192}Ir source, whereas MMGC-maximum 10 at UTM coordinates (514455, 6253494) indicates the presence of the radionuclides ^{137}Cs and ^{99m}Tm, also observed at this location on June 20th.

The spectra of a second cluster of MMGC-maxima 5, 6, 9, 11, 12 and 15 are displayed in figure 69. MMGC-maximum 6 located at UTM coordinates (516484, 6254610) shows photopeaks which were identified as the main photon emissions of ^{75}Se around 130 keV, 270 keV and 400 keV. The photo peaks in the spectrum over MMGC-maximum 9 at UTM coordinates (516631, 6254763) were interpreted as originating from the main photon emissions of the radionuclide ^{111}In at 171 keV and 245 keV. MMGC-maximum 5 at UTM coordinates (516769; 6254783) indicates ^{137}Cs which can also be identified in the other spectra of this MMGC-maxima cluster, sometimes associated with ^{99m}Tc. The spectrum measured over MMGC-maximum 8 at UTM coordinates (514464, 6254048) identifies also ^{75}Se. The distance to MMGC-maximum 6 of more than two kilometres indicates the presence of a second ^{75}Se source. The spectrum of MMGC-maximum 13 at UTM coordinates (517446, 6254766) (figure 71) identifies the radionuclide as ^{137}Cs. The spectra of MMGC-maxima 14, 16, 17, 18 and 19 were inspected without an indication of artificial radionuclides.

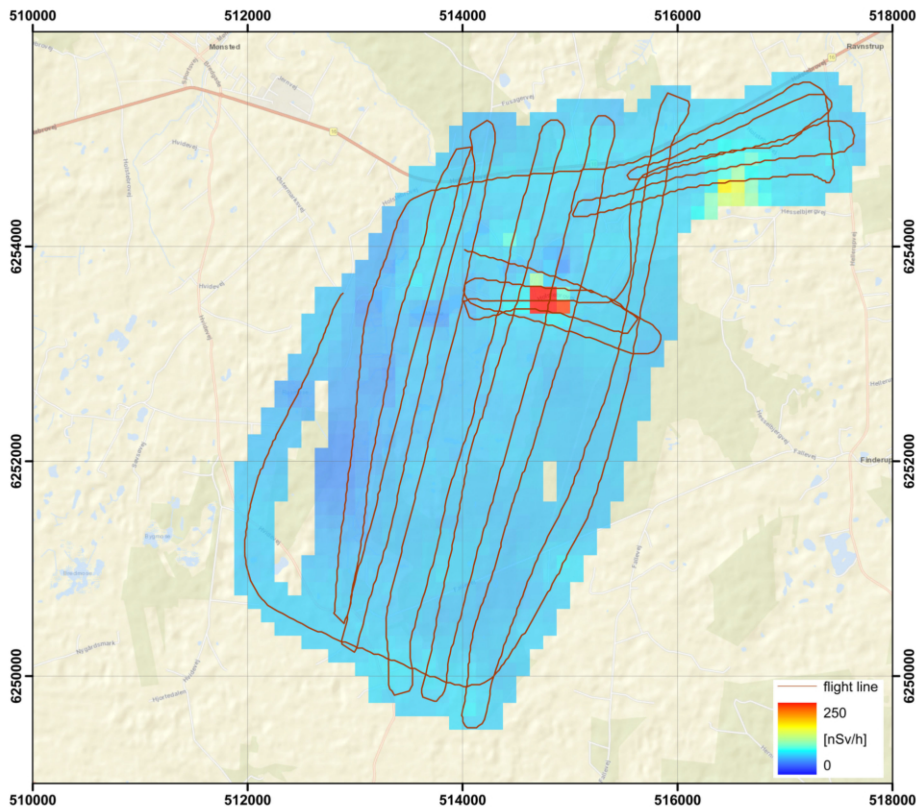

Figure 65: Dose rate over the Contex 2018 exercise area on June 21st. World street map ©2018 ESRI Inc.

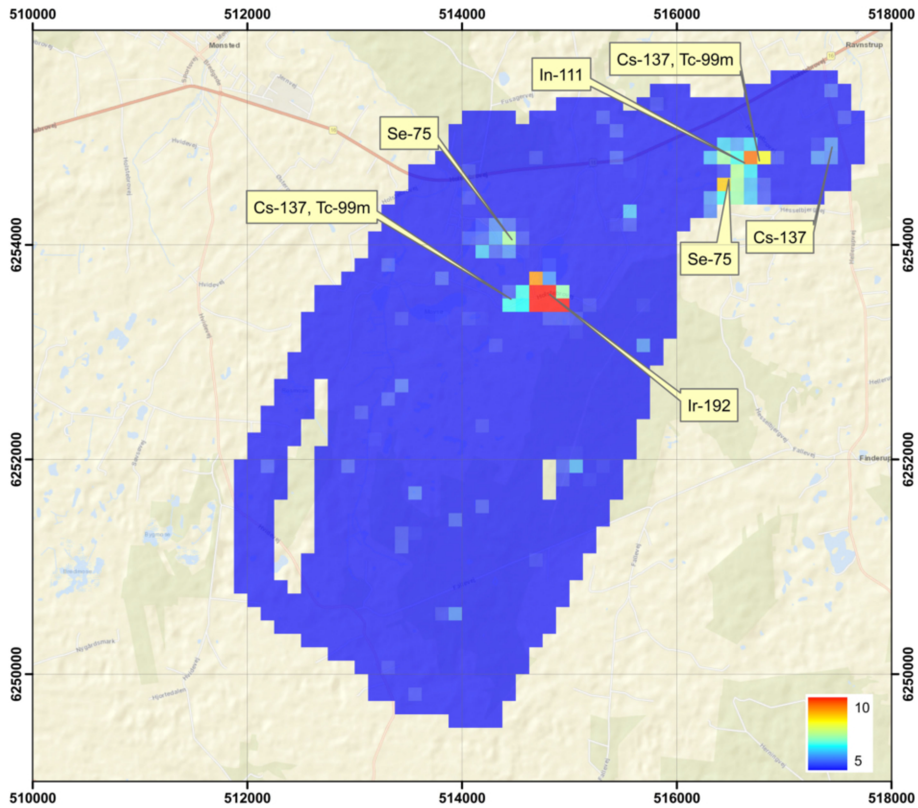

Figure 66: Man-made gross counts (MMGC) - ratio over the Contex 2018 exercise area on June 21st. World street map ©2018 ESRI Inc.

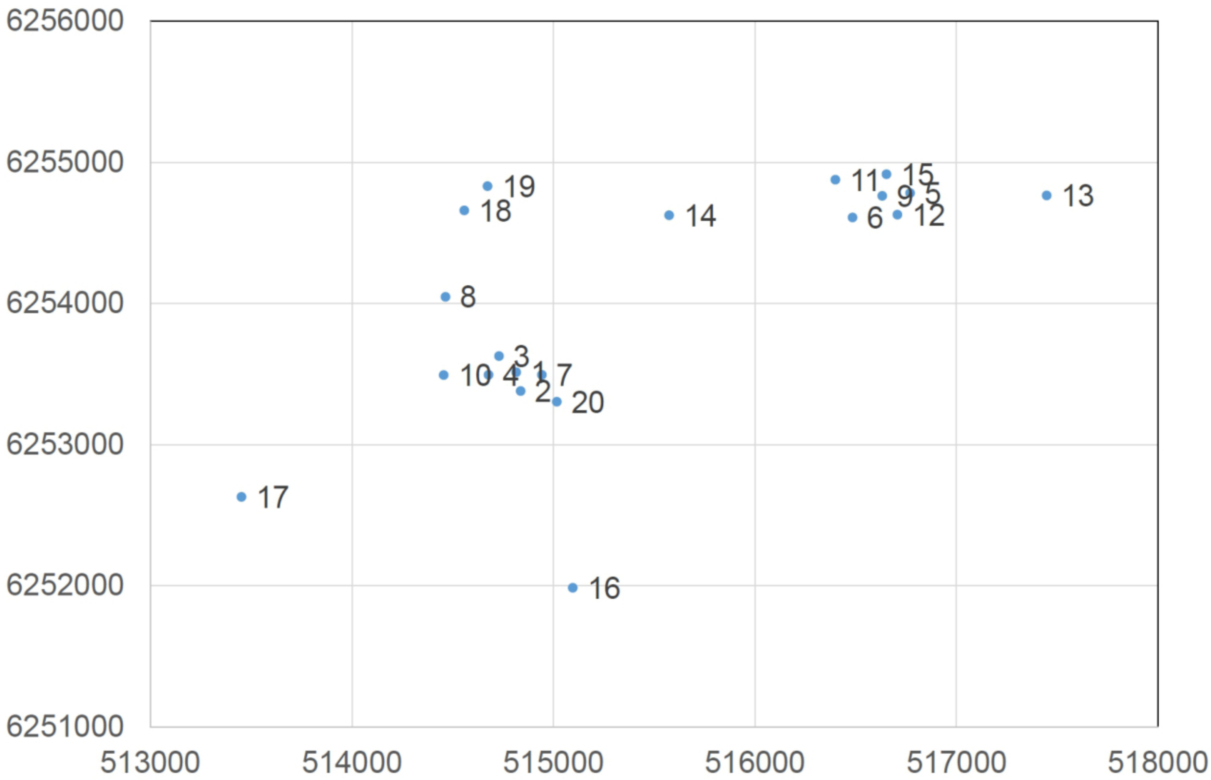

Figure 67: Location of the twenty largest MMGC values with distances larger than 125 m measured on June 21st (UTM32 coordinates).

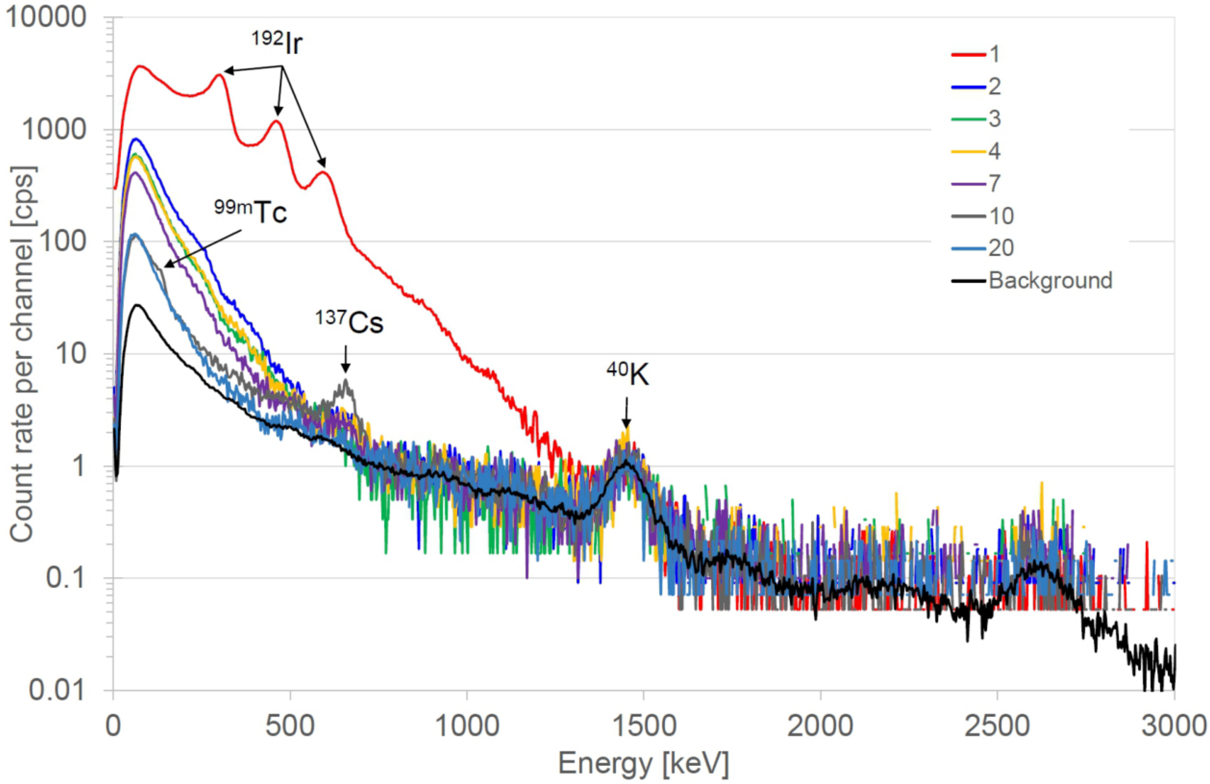

Figure 68: Average spectra over the MMGC-maxima No. 1, 2, 3, 4, 7, 10 and 20 measured on June 21st compared to a background spectrum.

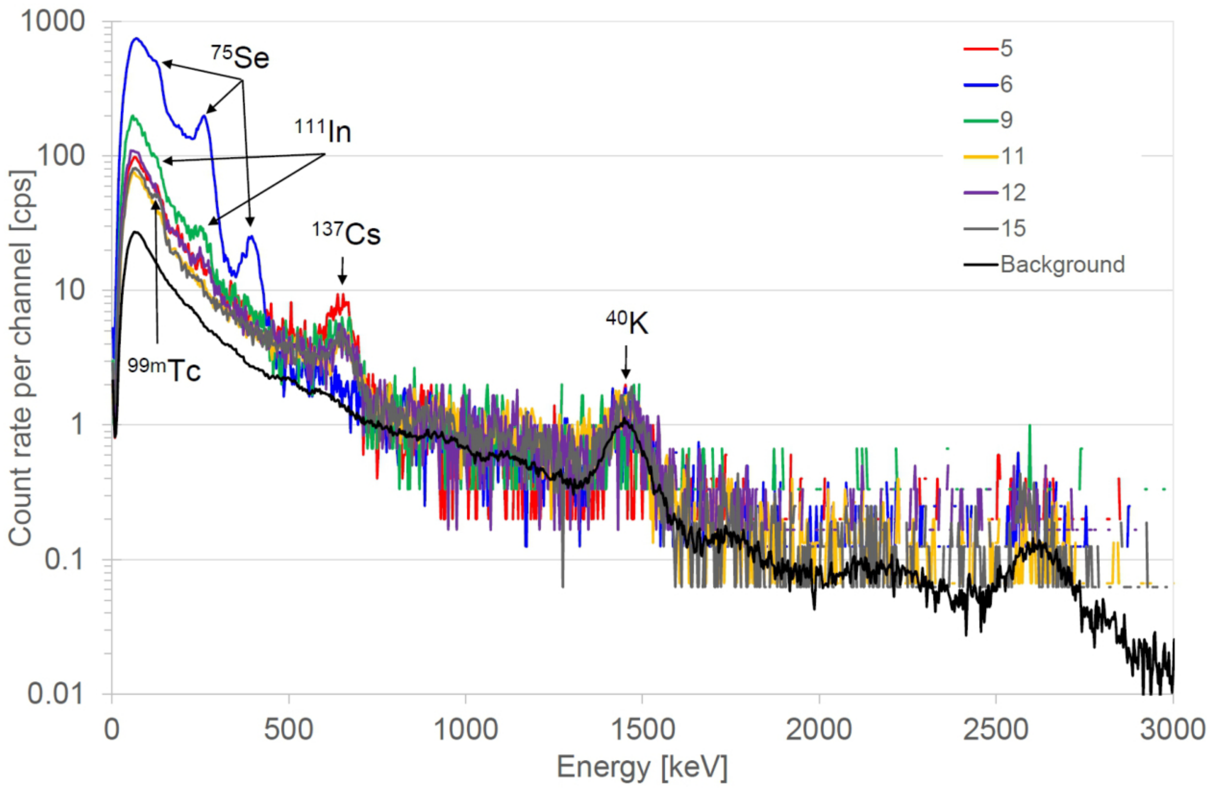

Figure 69: Average spectra over the MMGC-maxima No. 5, 6, 9, 11, 12 and 15 measured on June 21st compared to a background spectrum.

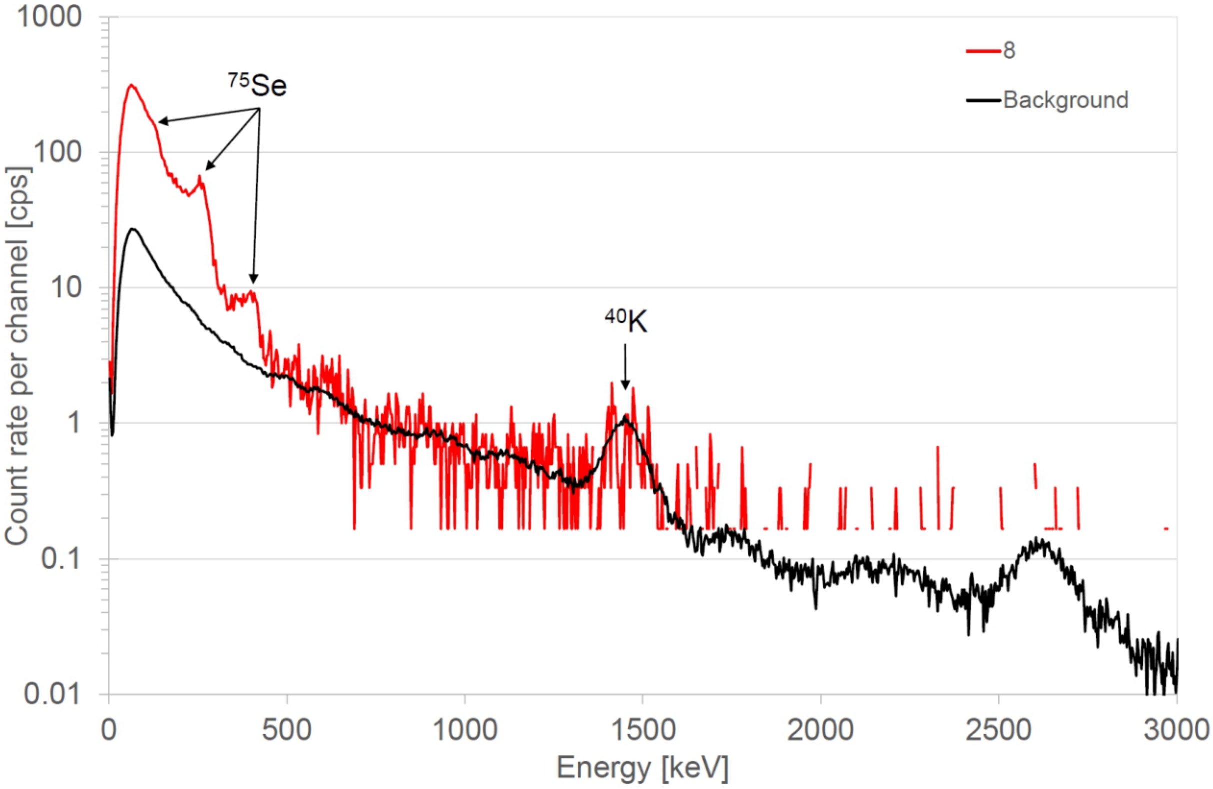

Figure 70: Average spectrum over the MMGC-maximum No. 8 measured on June 21st compared to a background spectrum.

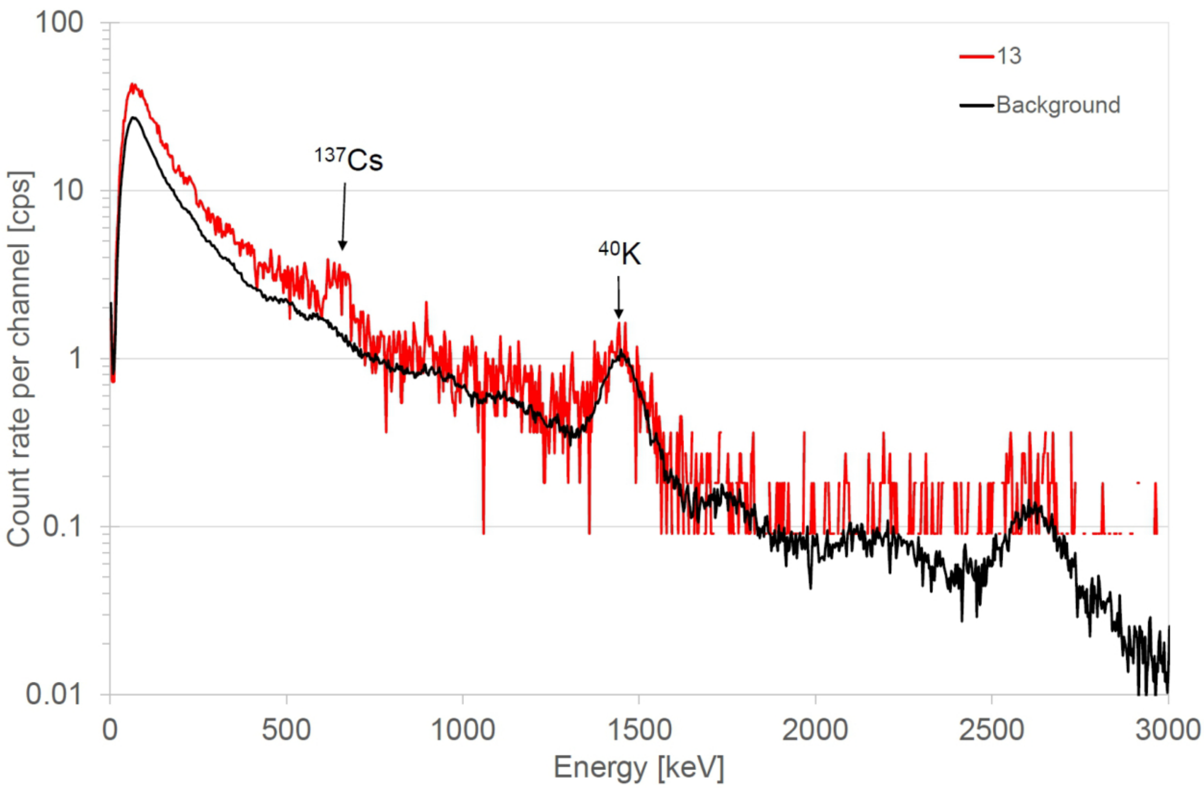

Figure 71: Average spectrum over the MMGC-maximum No. 13 measured on June 21st compared to a background spectrum.

3 Conclusions

The survey of the environs of the Swiss nuclear power plants Beznau (KKB) and Leibstadt (KKL), the intermediate storage facility ZWILAG and the Paul Scherrer Institute showed no artificial radionuclides outside of the plant premises. On request of German authorities, the measuring area was extended into German territory. In this area, a dose rate anomaly associated with ^{232}Th activity in a mineral processing plant could be identified.

The measurements over the cities of Fribourg, Solothurn and Yverdon-les-Bains expanded the database of radiation background over Swiss cities. No unusual values of the radiological quantities were observed. The measurement in the vicinity of Yverdon-les-Bains was used to directly compare the evaluation software of the old ARM system (MGS32) to the proprietary software of the manufacturer of the RLL system (Mirion). The differences observed in 2016 between the ARM and RLL measuring systems could be associated with different calibration factors used in the respective evaluation software, whereas detector efficiency of both systems could be considered identical.

Measurements around Mont Vully on behalf of the University of Basel could not clearly locate small scale anomalies of ^{238}U concentrations due to the field of view of the airborne measurements and depth of the peat layer containing elevated ^{238}U concentrations.

Measurements along a transversal from Berne to Kandersteg showed expected results due to flight altitude, content of natural radionuclides and attenuation of photons by water bodies.

An international exercise in northern Denmark provided the opportunity to measure an altitude profile over the North Sea with low airborne radon progeny concentrations. A clear difference to measurements over Swiss inland lakes was observed. This difference was used for investigating a potential method to compensate for the influence of airborne radon progeny on the measurement of ^{238}U activity concentrations. The organisers of the exercise placed several sources of different radionuclides and activities in the exercise area, challenging the performance of airborne detection. A method using maxima of the man-made-gross-count(MMGC)-ratio to define points which should be inspected more closely was developed. The spectra of these points of interest were inspected in detail and led to the identification of ^{137}Cs, ^{192}Ir, ^{99m}Tc, ^{75}Se and ^{111}In sources. The lower energy limit of the existing data evaluation set to 400 keV should be inspected to optimise performance for man-made radionuclides with photon emissions at lower energies.

4 Literature

Bucher, B.: Methodische Weiterentwicklungen in der Aeroradiometrie. Dissertation Nr. 13973, ETH Zürich, 2001.

Hurley, P.M., Fairbairn, H.W.: Abundance and Distribution of Uranium and Thorium in Zircon, Sphene, Apatite, Epidote, and Monazite in Granitic Rocks. Eos Trans. AGU 38(6), 939-944, 1957.

Minty, B.R.S., Luyendyk, A.P.J., Brodie, R.C.: Calibration and data processing for airborne gamma-ray spectrometry. AGSO Journal of Australian Geology & Geophysics 17(2), 51-62, 1997.

Schwarz, G. F.: Methodische Entwicklungen zur Aerogammaspektrometrie. Beiträge zur Geologie der Schweiz, Geophysik Nr. 23, Schweizerische Geophysikalische Kommission, 1991.

5 Previous reports

Schwarz, G. F., Klingelé, E. E., Rybach, L.: Aeroradiometrische Messungen in der Umgebung der schweizerischen Kernanlagen. Bericht für das Jahr 1989 zuhanden der Hauptabteilung für die Sicherheit der Kernanlagen (HSK). Interner Bericht, Institut für Geophysik, ETH Zürich, 1990.

Schwarz, G. F., Klingelé, E. E., Rybach, L.: Aeroradiometrische Messungen in der Umgebung der schweizerischen Kernanlagen. Bericht für das Jahr 1990 zuhanden der Hauptabteilung für die Sicherheit der Kernanlagen (HSK). Interner Bericht, Institut für Geophysik, ETH Zürich, 1991.

Schwarz, G. F., Klingelé, E. E., Rybach, L.: Aeroradiometrische Messungen in der Umgebung der schweizerischen Kernanlagen. Bericht für das Jahr 1991 zuhanden der Hauptabteilung für die Sicherheit der Kernanlagen (HSK). Interner Bericht, Institut für Geophysik, ETH Zürich, 1992.

Schwarz, G. F., Klingelé, E. E., Rybach, L.: Aeroradiometrische Messungen in der Umgebung der schweizerischen Kernanlagen. Bericht für das Jahr 1992 zuhanden der Hauptabteilung für die Sicherheit der Kernanlagen (HSK). Interner Bericht, Institut für Geophysik, ETH Zürich, 1993.

Schwarz, G. F., Klingelé, E. E., Rybach, L.: Aeroradiometrische Messungen in der Umgebung der schweizerischen Kernanlagen. Bericht für das Jahr 1993 zuhanden der Hauptabteilung für die Sicherheit der Kernanlagen (HSK). Interner Bericht, Institut für Geophysik, ETH Zürich, 1994.

Schwarz, G. F., Rybach, L.: Aeroradiometrische Messungen im Rahmen der Übung ARM94. Bericht für das Jahr 1994 zuhanden der Fachgruppe Aeroradiometrie (FAR). Interner Bericht, Institut für Geophysik, ETH Zürich, 1995.

Schwarz, G. F., Rybach, L.: Aeroradiometrische Messungen im Rahmen der Übung ARM95. Bericht für das Jahr 1995 zuhanden der Fachgruppe Aeroradiometrie (FAR). Interner Bericht, Institut für Geophysik, ETH Zürich, 1996.

Schwarz, G. F., Rybach, L., Bärlocher, C.: Aeroradiometrische Messungen im Rahmen der Übung ARM96. Bericht für das Jahr 1996 zuhanden der Fachgruppe Aeroradiometrie (FAR). Interner Bericht, Institut für Geophysik, ETH Zürich, 1997.

Bucher, B., Rybach, L., Schwarz, G., Bärlocher, C.: Aeroradiometrische Messungen im Rahmen der Übung ARM97. Bericht für das Jahr 1997 zuhanden der Fachgruppe Aeroradiometrie (FAR). Interner Bericht, Institut für Geophysik, ETH Zürich, 1998.

Bucher, B., Rybach, L., Schwarz, G., Bärlocher, C.: Aeroradiometrische Messungen im Rahmen der Übung ARM98. Bericht für das Jahr 1998 zuhanden der Fachgruppe Aeroradiometrie (FAR). Interner Bericht, Institut für Geophysik, ETH Zürich, 1999.

Bucher, B., Rybach, L., Schwarz, G., Bärlocher, C.: Aeroradiometrische Messungen im Rahmen der Übung ARM99. Bericht für das Jahr 1999 zuhanden der Fachgruppe Aeroradiometrie (FAR). Interner Bericht, Institut für Geophysik, ETH Zürich, 2000.

Bucher, B., Rybach, L., Schwarz, G., Bärlocher, C.: Aeroradiometrische Messungen im Rahmen der Übung ARM00. Bericht für das Jahr 2000 zuhanden der Fachgruppe Aeroradiometrie (FAR). Interner Bericht, Institut für Geophysik, ETH Zürich, 2001.

Bucher, B., Rybach, L., Schwarz, G., Bärlocher, C.: Aeroradiometrische Messungen im Rahmen der Übung ARM01. Bericht für das Jahr 2001 zuhanden der Fachgruppe Aeroradiometrie (FAR). Interner Bericht, Paul Scherrer Institut, Villigen, Schweiz, 2002.

Bucher, B., Rybach, L., Schwarz, G., Bärlocher, C.: Aeroradiometrische Messungen im Rahmen der Übung ARM02. Bericht für das Jahr 2002 zuhanden der Fachgruppe Aeroradiometrie (FAR). Interner Bericht, Paul Scherrer Institut, Villigen, Schweiz, 2003.

Bucher, B., Rybach, L., Schwarz, G.: Aeroradiometrische Messungen im Rahmen der Übung ARM03. PSI-Bericht 04-14, ISSN 1019-0643, Paul Scherrer Institut, Villigen, Schweiz, 2004.

Bucher, B., Butterweck, G., Rybach, L., Schwarz, G.: Aeroradiometrische Messungen im Rahmen der Übung ARM04. PSI-Bericht 05-10, ISSN 1019-0643, Paul Scherrer Institut, Villigen, Schweiz, 2005.

Bucher, B., Butterweck, G., Rybach, L., Schwarz, G.: Aeroradiometrische Messungen im Rahmen der Übung ARM05. PSI-Bericht 06-06, ISSN 1019-0643, Paul Scherrer Institut, Villigen, Schweiz, 2006.

Bucher, B., Butterweck, G., Rybach, L., Schwarz, G.: Aeroradiometrische Messungen im Rahmen der Übung ARM06. PSI-Bericht 07-02, ISSN 1019-0643, Paul Scherrer Institut, Villigen, Schweiz, 2007.

Bucher, B., Guillot, L., Strobl, C., Butterweck, G., Gutierrez, S., Thomas, M., Hohmann, C., Krol, I., Rybach, L., Schwarz, G.: International Intercomparison Exercise of Airborne Gammaspectrometric Systems of Germany, France and Switzerland in the Framework of the Swiss Exercise ARM07. PSI-Bericht Nr. 09-07, ISSN 1019-0643, Paul Scherrer Institut, Villigen, Schweiz, 2009.

Bucher, B., Butterweck, G., Rybach, L., Schwarz, G.: Aeroradiometrische Messungen im Rahmen der Übung ARM08. PSI-Bericht Nr. 09-02, ISSN 1019-0643, Paul Scherrer Institut, Villigen, Schweiz, 2009.

Bucher, B., Butterweck, G., Rybach, L., Schwarz, G., Strobl, C.: Aeroradiometrische Messungen im Rahmen der Übung ARM09. PSI-Bericht Nr. 10-01, ISSN 1019-0643, Paul Scherrer Institut, Villigen, Schweiz, 2010.

Bucher, B., Butterweck, G., Rybach, L., Schwarz, G., Mayer, S.: Aeroradiometrische Messungen im Rahmen der Übung ARM10. PSI-Bericht Nr. 11-02, ISSN 1019-0643, Paul Scherrer Institut, Villigen, Schweiz, 2011.

Bucher, B., Butterweck, G., Rybach, L., Schwarz, G., Mayer, S.: Aeroradiometric Measurements in the Framework of the Swiss Exercise ARM11. PSI-Report No. 12-04, ISSN 1019-0643, Paul Scherrer Institut, Villigen, Switzerland, 2012.

Butterweck, G., Bucher, B., Rybach, L., Schwarz, G., Hödlmoser, H., Mayer, S., Danzi, C. Scharding, G.: Aeroradiometric Measurements in the Framework of the Swiss Exercise ARM12. PSI-Report No. 13-01, ISSN 1019-0643, Paul Scherrer Institut, Villigen, Switzerland, 2013.

Butterweck, G., Bucher, B., Rybach, L., Schwarz, G., Hohmann, E., Mayer, S., Danzi, C. Scharding, G.: Aeroradiometric Measurements in the Framework of the Swiss Exercise ARM13. PSI-Report No. 15-01, ISSN 1019-0643, Paul Scherrer Institut, Villigen, Switzerland, 2015.

Butterweck, G., Bucher, B., Rybach, L., Schwarz, G., Hohmann, E., Mayer, S., Danzi, C. Scharding, G.: Aeroradiometric Measurements in the Framework of the Swiss Exercises ARM14 and FTX14. PSI-Report No. 15-02, ISSN 1019-0643, Paul Scherrer Institut, Villigen, Switzerland, 2015.

Butterweck, G., Bucher, B., Rybach, L., Schwarz, G., Hofstetter-Boillat, B., Hohmann, E., Mayer, S., Danzi, C. Scharding, G.: Aeroradiometric Measurements in the Framework of the Swiss Exercises ARM15, GNU15 and the International Exercise AGC15. PSI-Report No. 15-04, ISSN 1019-0643, Paul Scherrer Institut, Villigen, Switzerland, 2015.

Butterweck, G., Bucher, B., Rybach, L., Poretti, C., Maillard, S., Schwarz, G., Hofstetter-Boillat, B., Hohmann, E., Mayer, S., Scharding, G.: Aeroradiometric Measurements in the Framework of the Swiss Exercises ARM16 and LAURA. PSI-Report No. 17-01, ISSN 1019-0643, Paul Scherrer Institut, Villigen, Switzerland, 2017.

Butterweck, G., Bucher, B., Gryc, L., Debayle, C., Strobl, C., Maillard, S., Thomas, M., Helbig, A., Krol, I., Chuzel, S., Couvez, C., Ohera, M., Rybach, L., Poretti, C., Hofstetter-Boillat, B., Mayer, S., Scharding, G.: International Intercomparison Exercise of Airborne Gamma-Spectrometric Systems of the Czech Republic, France, Germany and Switzerland in the Framework of the Swiss Exercise ARM17. PSI-Report No. 18-04, ISSN 1019-0643, Paul Scherrer Institut, Villigen, Switzerland, 2018.

The reports since 1994 can be found and downloaded from the FAR website `http://www.far.ensi.ch`.

6 Evaluation parameter files

The parameter files used for the evaluation of raw data in this report are listed below to improve the traceability of the presented results. The detector definition files have been re-evaluated for all detectors in 2014. A software modification was performed to take into account different formats of terrain model files used for topographic correction, leading to a change in the detector definition file.

6.1 DefinitionFile_Processing_ch.txt

This file defines the standard parameters used for the calculation and gridding of measured data used throughout this report.

```
Definition file Swiss MGS32
"Windows"
10
Total    401.    2997.      0.   0
K-40    1369.    1558.   1460.   1
U-238   1664.    1853.   1765.   1
Th-232  2407.    2797.   2615.   1
Cs-137   600.     720.    660.   2
Co-60   1100.    1400.      0.   2
MMGC1    400.    1400.      0.   0
MMGC2   1400.    2997.      0.   0
LOW       40.     720.      0.   0
MID      720.    2997.      0.   0
"Ratios"
3
MMGCVerhältnis   MMGC1  MMGC2  Ratio_MMGC
LOWHigh          LOW    MMGC2  RatioLowHigh
LowMid           LOW    MID    RatioLowMid
"Conversion factors Activity to Dose Rate"
8
Total       0        NoCalibration   "     "   0
AD_K-40        0.044    DHSR            "nSv/h"   1
AD_U-238       0.55     DHSR            "nSv/h"   1
AD_Th-232      0.77     DHSR            "nSv/h"   1
AD_Cs-137      0.2      DHSR            "nSv/h"   2
Co-60       0        NoCalibration   "     "   0
MMGC1       0        NoCalibration   "     "   0
MMGC2       0        NoCalibration   "     "   0
"Typ des Darstellungsgrenzwertes"
1
Nachweistyp  0
"counts of spectra to stack"
1
Counts 1
"Auszugebende Werte"
```

```
30
"DHSR TOT            ","DHSR_TOT","nSv/h       ",0.00,250.00
"AP_Co-60            ","AP_Co-60","MBq       ",0.00,150.00
"AP_Cs-137           ","AP_Cs-137","MBq       ",0.00,40.00
"Terr. DL            ","DHSR_TOT","nSv/h     ",0.00,250.00
"CR_Caesium          ","CR_Cs-137","cps       ",20.00,120.00
"CR_Cobalt           ","CR_Co-60","cps       ",0.00,100.00
"NR_Caesium          ","NR_Cs-137","cps       ",0.00,120.00
"NR_Cobalt           ","NR_Co-60","cps       ",0.00,100.00
"Total_CR_corr       ","NR_Total","cps       ",200.00,1200.00
"K-40                ","AD_K-40","Bq/kg     ",0.00,1000.00
"U-238               ","AD_U-238","Bq/kg     ",0.00,120.00
"Th-232              ","AD_Th-232","Bq/kg     ",0.00,120.00
"Cs-137              ","AD_Cs-137","Bq/kg     ",0.00,240.00
"Cobalt_CR           ","NR_Co-60","cps       ",0.00,120.00
"Nat.Terr.DL         ","DHSR_NAT","nSv/h     ",0.00,250.00
"Künst.DL            ","DHSR_ANT","nSv/h     ",0.00,250.00
"MMGC_Ratio          ","&MMGC_Ratio","%         ",4.00,6.00
"Cosmic DL           ","DHSR_COS","nSv/h     ",20.00,60.00
"Cosmic              ","CR_COS","cps       ",000.00,400.00
"Radar               ","PH","m         ",0.00,300.00
"ODL                 ","DHSR","nSv/h     ",0.00,250
"AD_UT_K-40          ","AD_UT_K-40","Bq/kg     ",0.00,200
"AD_UT_U-238         ","AD_UT_U-238","Bq/kg     ",0.00,50
"AD_UT_Th-232        ","AD_UT_Th-232","Bq/kg     ",0.00,40
"AD_UT_Cs-137        ","AD_UT_Cs-137","Bq/kg     ",0.00,20
"Err_Co-60           ","NR_UT_Co-60","cps       ",0.00,40
"Nachweis_Cs-137     ","CR_LD_Cs-137,"cps       ",0.00,100.00
"Nachweis_Co-60      ","CR_LD_Co-60","cps       ",0.00,100.00
"Cs-137 beta=0       ","AA_Cs-137","Bq/m2     ",0.00,20000.00
"AA_UT_Cs-137        ","AA_UT_Cs-137","Bq/m2     ",0.00,20
```

6.2 DefinitionFile_Det002.txt

This file defines the parameter set used for RLL detector with serial number 002.

```
Definition file System
"Koordinaten"
WGS84
"Non-linearity"
4
a0  0.000000
a1  0.083333
a2  0.000000
a3  0.000000
"Recorder old RDT-Files"
8
```

```
Radar  0.00   -61.00
Baro   0.74   457.14
Cosm   0.00   1.00
Dead   5.00   0.00
Time   0.00   1.00
Temp   0.00   1.00
Pitch  0.00   76.20
Roll   0.00   90.91
"Background/Cosmic"
10
Total      62.266       5.534      0.463
K-40        6.515       0.270      0.033
U-238       2.434       0.227      0.032
Th-232     -0.013       0.294      0.029
Cs-137     10.974       0.520      0.089
Co-60       7.562       0.540      0.073
MMGC1      56.303       3.910      0.375
MMGC2       5.963       1.624      0.094
LOW          0.          0.         0.
MID          0.          0.         0.
"Stripping Coefficients"
10
1.000   0.000   0.000   0.000   0.000   0.000   0.000   0.000   0.000   0.000
0.000   1.000   0.986   0.468  -0.002   0.085   0.000   0.000   0.000   0.000
0.000  -0.003   1.000   0.374   0.000  -0.002   0.000   0.000   0.000   0.000
0.000  -0.004   0.061   1.000   0.000  -0.001   0.000   0.000   0.000   0.000
0.000   0.462   3.349   1.750   1.000   0.150   0.000   0.000   0.000   0.000
0.000   0.817   2.447   0.686   0.001   1.000   0.000   0.000   0.000   0.000
0.000   0.000   0.000   0.000   0.000   0.000   1.000   0.000   0.000   0.000
0.000   0.000   0.000   0.000   0.000   0.000   0.000   1.000   0.000   0.000
0.000   0.000   0.000   0.000   0.000   0.000   0.000   0.000   1.000   0.000
0.000   0.000   0.000   0.000   0.000   0.000   0.000   0.000   0.000   1.000
"Converted Stripping Coefficients Matrix"
10
1.000   0.000   0.000   0.000   0.000   0.000   0.000   0.000   0.000   0.000
0.000   1.072  -0.828  -0.131   0.002  -0.093   0.000   0.000   0.000   0.000
0.000   0.001   1.019  -0.383   0.000   0.001   0.000   0.000   0.000   0.000
0.000   0.003  -0.068   1.023   0.000   0.001   0.000   0.000   0.000   0.000
0.000  -0.371  -2.646  -0.499   0.999  -0.124   0.000   0.000   0.000   0.000
0.000  -0.879  -1.768   0.343  -0.003   1.073   0.000   0.000   0.000   0.000
0.000   0.000   0.000   0.000   0.000   0.000   1.000   0.000   0.000   0.000
0.000   0.000   0.000   0.000   0.000   0.000   0.000   1.000   0.000   0.000
0.000   0.000   0.000   0.000   0.000   0.000   0.000   0.000   1.000   0.000
0.000   0.000   0.000   0.000   0.000   0.000   0.000   0.000   0.000   1.000
"Sigma of Converted Stripping Coefficients Matrix"
10
0.000  0.000  0.000  0.000  0.000  0.000  0.000  0.000  0.000  0.000
0.000  0.000 -0.040 -0.017  0.000 -0.016  0.000  0.000  0.000  0.000
0.000  0.000  0.000 -0.028  0.000  0.000  0.000  0.000  0.000  0.000
```

```
0.000  0.000 -0.009  0.000  0.000  0.000  0.000  0.000  0.000  0.000
0.000 -0.080 -0.103 -0.037  0.000 -0.008  0.000  0.000  0.000  0.000
0.000 -0.140 -0.068  0.013  0.000  0.000  0.000  0.000  0.000  0.000
0.000  0.000  0.000  0.000  0.000  0.000  0.000  0.000  0.000  0.000
0.000  0.000  0.000  0.000  0.000  0.000  0.000  0.000  0.000  0.000
0.000  0.000  0.000  0.000  0.000  0.000  0.000  0.000  0.000  0.000
0.000  0.000  0.000  0.000  0.000  0.000  0.000  0.000  0.000  0.000
"Attenuation Coefficients"
10
Total        0.00600    1.00000   0.0003
K-40         0.00800    1.00000   0.0008
U-238        0.00550    1.00000   0.0114
Th-232       0.00600    1.00000   0.0044
Cs-137       0.01000    1.00000   0.0100
Co-60        0.00800    1.00000   0.0080
MMGC1        0.00600    1.00000   0.0060
MMGC2        0.00650    1.00000   0.0065
LOW          0.02000    1.00000   0.01
MID          0.01500    1.00000   0.005
"3D Attenuation Coefficients"
10
Total        0.00350    2.00000
K-40         0.00420    2.00000
U-238        0.00320    2.00000
Th-232       0.00350    2.00000
Cs-137       0.00800    2.00000
Co-60        0.00800    1.00000
MMGC1        0.00600    1.00000
MMGC2        0.00650    1.00000
LOW          0.02000    1.00000
MID          0.01500    1.00000
"Conversion factors Counts to Activity"
11
Total        0        NoCalibration   "      "
K-40         7.27     AD_K-40         "Bq/kg"
U-238        2.63     AD_U-238        "Bq/kg"
Th-232       1.50     AD_Th-232       "Bq/kg"
Cs-137       2.00     AD_Cs-137       "Bq/kg"
Cs-137       34.99    AA_Cs-137       "Bq/m2"
Cs-137       7.53     AP_Cs-137       "MBq  "
Co-60        2.61     AP_Co-60        "MBq  "
Co-60        0        NoCalibration   "      "
MMGC1        0        NoCalibration   "      "
MMGC2        0        NoCalibration   "      "
"Radon"
1
0            0
"Höhenkorrektur"
4
```

```
AltMethod    1
GroundAltDGM 1
DGMType      0
PfadDHM25   C:\DATEN\Benno\Aeroradiometrie\Daten\DHM25\
"SDI Constants"
7
Aten         0.0053
Convert      0.00096
CosmicKorr   95.5
Back         12640.0
Gain         12.0
referenz_alt 100.0
Threshold    240.0
```

6.3 DefinitionFile_Det003.txt

This file defines the parameter set used for RLL detector with serial number 003.

```
Definition file System
"Koordinaten"
WGS84
"Non-linearity"
4
a0  0.000000
a1  0.083333
a2  0.000000
a3  0.000000
"Recorder old RDT-Files"
8
Radar  0.00   -61.00
Baro   0.74   457.14
Cosm   0.00   1.00
Dead   5.00   0.00
Time   0.00   1.00
Temp   0.00   1.00
Pitch  0.00   76.20
Roll   0.00   90.91
"Background/Cosmic"
10
Total      62.266       5.534      0.463
K-40        6.515       0.270      0.033
U-238       2.434       0.227      0.032
Th-232     -0.013       0.294      0.029
Cs-137     10.974       0.520      0.089
Co-60       7.562       0.540      0.073
MMGC1      56.303       3.910      0.375
MMGC2       5.963       1.624      0.094
```

```
LOW          0.          0.         0.
MID          0.          0.         0.
"Stripping Coefficients"
10
1.000  0.000  0.000  0.000  0.000  0.000  0.000  0.000  0.000  0.000
0.000  1.000  0.933  0.364 -0.014  0.014  0.000  0.000  0.000  0.000
0.000 -0.018  1.000  0.333 -0.002 -0.010  0.000  0.000  0.000  0.000
0.000 -0.012  0.049  1.000 -0.002 -0.009  0.000  0.000  0.000  0.000
0.000  0.394  3.129  1.518  1.000  0.103  0.000  0.000  0.000  0.000
0.000  0.698  2.371  0.457 -0.012  1.000  0.000  0.000  0.000  0.000
0.000  0.000  0.000  0.000  0.000  0.000  1.000  0.000  0.000  0.000
0.000  0.000  0.000  0.000  0.000  0.000  0.000  1.000  0.000  0.000
0.000  0.000  0.000  0.000  0.000  0.000  0.000  0.000  1.000  0.000
0.000  0.000  0.000  0.000  0.000  0.000  0.000  0.000  0.000  1.000
"Converted Stripping Coefficients Matrix"
10
1.000  0.000  0.000  0.000  0.000  0.000  0.000  0.000  0.000  0.000
0.000  0.995 -0.906 -0.068  0.012 -0.024  0.000  0.000  0.000  0.000
0.000  0.009  0.989 -0.337  0.001  0.006  0.000  0.000  0.000  0.000
0.000  0.005 -0.079  1.018  0.002  0.008  0.000  0.000  0.000  0.000
0.000 -0.353 -2.442 -0.502  0.988 -0.125  0.000  0.000  0.000  0.000
0.000 -0.722 -1.708  0.376  0.000  0.997  0.000  0.000  0.000  0.000
0.000  0.000  0.000  0.000  0.000  0.000  1.000  0.000  0.000  0.000
0.000  0.000  0.000  0.000  0.000  0.000  0.000  1.000  0.000  0.000
0.000  0.000  0.000  0.000  0.000  0.000  0.000  0.000  1.000  0.000
0.000  0.000  0.000  0.000  0.000  0.000  0.000  0.000  0.000  1.000
"Sigma of Converted Stripping Coefficients Matrix"
10
0.000  0.000  0.000  0.000  0.000  0.000  0.000  0.000  0.000  0.000
0.000  0.000 -0.040 -0.017  0.000 -0.016  0.000  0.000  0.000  0.000
0.000  0.000  0.000 -0.028  0.000  0.000  0.000  0.000  0.000  0.000
0.000  0.000 -0.009  0.000  0.000  0.000  0.000  0.000  0.000  0.000
0.000 -0.080 -0.103 -0.037  0.000 -0.008  0.000  0.000  0.000  0.000
0.000 -0.140 -0.068  0.013  0.000  0.000  0.000  0.000  0.000  0.000
0.000  0.000  0.000  0.000  0.000  0.000  0.000  0.000  0.000  0.000
0.000  0.000  0.000  0.000  0.000  0.000  0.000  0.000  0.000  0.000
0.000  0.000  0.000  0.000  0.000  0.000  0.000  0.000  0.000  0.000
0.000  0.000  0.000  0.000  0.000  0.000  0.000  0.000  0.000  0.000
"Attenuation Coefficients"
10
Total        0.00600    1.00000   0.0003
K-40         0.00800    1.00000   0.0008
U-238        0.00550    1.00000   0.0114
Th-232       0.00600    1.00000   0.0044
Cs-137       0.01000    1.00000   0.0100
Co-60        0.00800    1.00000   0.0080
MMGC1        0.00600    1.00000   0.0060
MMGC2        0.00650    1.00000   0.0065
LOW          0.02000    1.00000   0.01
```

```
MID          0.01500    1.00000   0.005
"3D Attenuation Coefficients"
10
Total        0.00350    2.00000
K-40         0.00420    2.00000
U-238        0.00320    2.00000
Th-232       0.00350    2.00000
Cs-137       0.00800    2.00000
Co-60        0.00800    1.00000
MMGC1        0.00600    1.00000
MMGC2        0.00650    1.00000
LOW          0.02000    1.00000
MID          0.01500    1.00000
"Conversion factors Counts to Activity"
11
Total        0         NoCalibration   "     "
K-40         7.27      AD_K-40         "Bq/kg"
U-238        2.63      AD_U-238        "Bq/kg"
Th-232       1.50      AD_Th-232       "Bq/kg"
Cs-137       2.00      AD_Cs-137       "Bq/kg"
Cs-137       34.99     AA_Cs-137       "Bq/m2"
Cs-137       7.53      AP_Cs-137       "MBq  "
Co-60        2.61      AP_Co-60        "MBq  "
Co-60        0         NoCalibration   "     "
MMGC1        0         NoCalibration   "     "
MMGC2        0         NoCalibration   "     "
"Radon"
1
0            0
"Höhenkorrektur"
4
AltMethod     1
GroundAltDGM 1
DGMType       0
PfadDHM25    C:\DATEN\Benno\Aeroradiometrie\Daten\DHM25\
"SDI Constants"
7
Aten          0.0053
Convert       0.00096
CosmicKorr    95.5
Back          12640.0
Gain          12.0
referenz_alt 100.0
Threshold     240.0
```

Paul Scherrer Institut :: Forschungsstrasse 111 :: 5232 Villigen PSI :: Switzerland :: Tel. +41 56 310 21 11 :: www.psi.ch